The Dissertation Committee for Jeffrey Allan Nanzer Certifies that this is the approved version of the following dissertation:

Human Presence Detection Using Millimeter-Wave Radiometry

Committee:

Hao Ling, Supervisor

Robert Rogers, Co-Supervisor

Dean Neikirk

Elmira Popova

Ali Yilmaz

Human Presence Detection Using Millimeter-Wave Radiometry

by

Jeffrey Allan Nanzer, B.S., M.S.E.

Dissertation

Presented to the Faculty of the Graduate School of

The University of Texas at Austin

in Partial Fulfillment

of the Requirements

for the Degree of

Doctor of Philosophy

The University of Texas at Austin

May 2008

Dedication

To Dr. Ed Rothwell, without whose support and encouragement I would not have begun

my journey through graduate school.

Acknowledgements

I am indebted to my committee for their insight and guidance in my research on this dissertation. Bob Rogers has provided endless and invaluable guidance and support throughout the process of this research and has helped me learn how to become an effective independent researcher. My academic career has been guided by Hao Ling, who has always been willing to provide me with advice on my classes, my publications, and my future as a researcher. I thank Elmira Popova for giving me encouragement and direction in the development of the statistical aspects of this dissertation, which had initially been a struggle. I am grateful to have Dean Neikirk as the chair of my committee, his suggestions have helped me develop a clearer focus for my research. I also thank Ali Yilmaz for providing his assistance on my committee.

I am fortunate to have been able to conduct my research for this dissertation at he Applied Research Laboratories at the University of Texas. My co-workers have provided me with support and advice and the state-of-the-art facilities have been an invaluable part of my research experience.

Finally, I wish to thank my family and friends for their unending support, and most of all, my wife, who has been my true friend and source of encouragement throughout my time in graduate school.

Human Presence Detection Using Millimeter-Wave Radiometry

Publication No._____

Jeffrey Allan Nanzer, Ph.D.

The University of Texas at Austin, 2008

Supervisors: Hao Ling and Robert Rogers

A novel method of human presence detection using passive millimeter-wave sensors is presented. The method focuses on detecting a standing human from a moving platform in a cluttered outdoor environment using millimeter-wave radiometry, which has not been attempted before. K_a-band radiometers are used in total power mode as well as correlation mode, which ideally responds well to self-luminous objects such as humans. The intrinsic radiative power from a human is derived as well as the responses of the total power and correlation mode. The application of correlation radiometer theory to the detection of self-luminous objects at close range is presented in the context of human presence detection. Modifications and additions to techniques developed in radio astronomy and remote sensing for close range terrestrial situations are developed and discussed. The correlation radiometer fringe frequency is analyzed in the context of the scanning beam detection system and is estimated using MUSIC and ESPRIT. Detection and classification of humans is accomplished using a Naïve Bayesian classifier. The performance of the classifier is measured using the F_1-measure and the receiver operating characteristic.

Table of Contents

List of Tables

List of Figures

xiii

Chapter 1: Introduction

The ability of a sensor to detect human presence is desirable in cases where the use of a person is unpractical, expensive, or dangerous. Many current techniques employ radars or infrared detectors. The drawback of a radar system is that it is not passive: it transmits as well as receives energy and thus could be detected. In addition, while a radar system can effectively detect a moving object, it cannot easily distinguish a stationary human from other stationary objects. Infrared (IR) systems are passive and can detect a stationary person however these systems detect thermal radiation from the skin surface and can thus be overcome by wearing thick clothing. In addition, IR sensors can be overcome by bright daytime sunlight reflection, rendering human detection impossible.

Passive millimeter-wave (PMMW) systems are an effective way of determining the presence of a stationary human. Systems of this form typically use total power radiometers which function similarly to infrared detectors in that they detect the radiation of objects due to their heat signatures, except at much lower frequencies thus detecting thermal radiation from the body as a whole rather than the skin surface. However, these sensors can still have trouble resolving the presence of a human in outdoor environments as background objects of greatly varying temperatures can confuse the sensor. This dissertation will show that a new technique in PMMW systems using radiometers in both total power and correlation mode can effectively detect the presence of a human from a moving platform.

No studies have been shown to successfully detect a stationary person in an outdoor environment from a moving platform. I will discuss the current state of

1

autonomous presence detection and show the lack of focus on this problem of human presence detection. The use of a radiometer in both total power and correlation mode presents a solution to this problem, and the use of a correlation receiver is a novel concept which has not been utilized in presence detection; such a receiver ideally responds well only to self-luminous objects such as humans. The requirements of the sensor will be put into context by reviewing the current state of technology in two areas which the detection method draws from: millimeter-wave radiometry and correlation radiometry in remote sensing. Following this, because the radiation detected by the method presented in this dissertation is thermal in origin, I will describe the uses and drawbacks of a more widely used thermal detector, infrared detection systems.

1.1 PROLEGOMENON

All objects with a physical temperature emit radiation at certain frequencies. In addition, the temperature of the object is proportional to the power of the emitted radiation. Humans tend to have greater temperature than inanimate objects and therefore the radiation emitted by humans in the microwave region of the electromagnetic spectrum is typically greater and is also essentially flat over frequency [1]; thus sensors can be used to detect the presence of a human in certain environments. One such sensor is a total power radiometer which detects the radiation power emitted by whatever it sees in its antenna beam and produces an output voltage proportional to the power detected. However, this system cannot easily distinguish between humans and objects of similar temperature.

The radiation emitted by a human differs from many outdoor objects in that it is more coherent because the human is a self-luminous object. Typical outdoor objects do not generate their own heat and thus their radiation is a combination of scattering,

reflection and thermal emission from solar heating. By using two total power radiometers and correlating the outputs the responses to these uncorrelated background objects can be reduced significantly, while the coherent, correlated radiation from a human will be preserved. This dissertation will present the development and analysis of such a radiometer and show that this sensor can effectively detect the presence of a human from a moving platform.

1.2 REVIEW OF PUBLISHED LITERATURE

1.2.1 Autonomous Robotic Sensing

Detection of human presence for autonomous sensors typically falls into the categories of motion detection and emission detection, and has been attempted by active and passive means using primarily infrared, ultrasonic, and microwave sensors [2]. Motion detection focuses on changes in a stable environment and has been accomplished successfully using microwave Doppler radars by examining the Doppler shift of the signal reflected off a moving person. Ultrasonic transducers have been used in an analogous way [3]. Motion detection is also achieved by using passive means such as video imagers or infrared imagers. These imagers work by detecting a change in a stationary scene as a person scans across the field of view. Imagers such as these are well suited to stationary applications since the background is stationary, though typically cannot be implemented as mobile sensors because the shifting background leaves no reference with which to compare changes. An example of a change-detection system for a moving platform was developed by H. R. Everett at the Naval Postgraduate School in a robot called ROBART II; the ultrasonic detection system creates a reference template of the most frequently occurring ranges detected in a specified area and compares subsequent detected ranges on following passes [3].

3

While a moving person is differentiated from his environment by his velocity, a standing human must be detected by other means of differentiating him from his environment. Emission detection focuses on intrinsic signals produced by a person, such as thermal radiation or acoustic signals. A number of methods have been developed, for instance ROBART II utilized an array of acoustical transducers to triangulate the position of a person creating noise. This method works well indoors or in very quiet outdoor environments but in typical outdoor environments ambient noise typically drowns out the acoustic signal from a moving person. Other techniques use optical arrays to detect any light emission, such as a person using a flashlight, or infrared thermal sensors [3, 4]. The drawbacks to optical detection are in cases such as broad daylight where a person uses no light source. For a thermal sensor, a person must appear warmer to the sensor than the background. For indoor environments this is a safe assumption, however in an outdoor daytime environment infrared detection becomes difficult, as I will discuss in Section 1.3.

An area of human presence detection which has not been explored is the passive detection of intrinsic millimeter-wave radiation from a human. Radiation in this frequency range has benefits over infrared in outdoor environments, as I will present in later sections. The method I present in this dissertation focuses on the detection of intrinsic human radiation using passive receivers and can detect a standing person in an outdoor environment, where other techniques have failed.

The human presence detection method utilizes passive millimeter-wave radiometry and a radiometric correlation technique which was developed in the fields of radio astronomy and remote sensing. I will put the objective in context by briefly reviewing current trends in millimeter-wave security applications as well as radio astronomy and remote sensing.

4

1.2.2 Millimeter-Wave Radiometry

The focus of passive millimeter-wave imaging has recently been in the area of contraband detection because millimeter-wave radiation passes through most garment and baggage materials with negligible attenuation [5]. The millimeter-wave emissivity of most metals is in the range of 0.10-0.30 while the millimeter-wave emissivity of a human is 0.60-0.65 [1]. Thus a metal weapon or other contraband hidden under clothing would appear cold on the warmer background of the human body. A contraband detection imager developed by Millivision Technologies [6] uses a focal plane array of 64 radiometric channels at 94 GHz to provide images of 28×28 pixels. The device is shown to work reasonably well indoors or outdoors with an all-sky background. However, the millimeter-wave radiometric temperature of the sky is approximately 20 K due to the cosmic microwave background [7], and in contrast, nearly any material will have a larger brightness temperature. Other millimeter-wave imagers use active technology for contraband detection, transmitting a signal and detecting the reflected millimeter-wave radiation from the person and any objects under the person's clothing [8, 9]. However, in a security environment it is beneficial to have a passive sensor so that no information is being transmitted that could possibly be intercepted, indicating to an intruder where the sensor might be. For this reason passive sensors are more desirable. In addition, millimeter-wave radars make no use of the thermal information detected by radiometers and thus amount to a simple mapping device.

Passive millimeter-wave radiometers have been developed as flight sensors mounted on helicopters. One design uses a phased-array frequency-scanned imager with a square planar dielectric antenna at 84.5 GHz to provide a 128×192 pixel detection map [10]. This study demonstrated that the emissivity of objects plays an important role; in

cases where no thermal contrast is present the differing emissivities will cause contrasting brightness temperatures. Other designs have used imagers for collision avoidance [11].

The detection method described in this dissertation shares much of the same technology as the systems just described, however for many of these systems, such as contraband detection, human presence is implied and even required. In other cases, such as collision-avoidance flight sensors, there have been no tests on detecting a human and no studies focused solely on presence detection. By concentrating on human presence detection my millimeter-wave detection method has the added benefit of a lower data rate than the systems discussed above. That is, the majority of millimeter-wave systems are imagers and thus require a large amount of data processing in order to run real-time. The technique described here uses one-dimensional sensors and correlates the outputs to determine a detection, thus by analyzing data arrays rather than matrices the processing time is easier to implement in real-time.

1.2.3 Radio Astronomy and Remote Sensing

A novel approach of the detection method is the use of a correlation mode to attempt to detect self-luminous objects. The correlation radiometer has been widely used in radio astronomy [12-15] and earth remote sensing [16-18]. In radio astronomy large radio telescopes are needed as the angular resolution of the system is dependent on the size of the antenna system. By using multiple antennas and correlating the outputs the effective aperture of the receiver is equal in size to the largest baseline between the antennas. An example is the Very Large Array in Socorro, NM, which comprises of 27 antennas with a maximum baseline of 36 km resulting in an angular resolution of 0.05 arcseconds.

The interferometer technique is also used in earth remote sensing where it is unfeasible to deploy a large single-aperture antenna in space. An example demonstrating the effectiveness of the technique is ESTAR which was an *L*-band airborne radiometer used to detect soil moisture content [18].

To achieve large effective apertures radio astronomy arrays correlate the outputs of the individual receivers. The voltage output of the receivers is comprised of two components: the signal from the radiating source V_s and noise from antenna reception of radiation away from the main beam as well as system noise generated in the microwave components V_i and is written by $V_{out,i} = V_i + V_s$, where $i = 1, 2$ indicates the receiver channel. The radiation from the source is coherent and thus the same in both receivers while the noise component is incoherent. Thus by multiplying the two voltages and averaging over a sufficient length of time, the incoherent noise components will tend to zero, while the signal component will be squared, resulting in a voltage output proportional to power. Following multiplication the output voltage is given by

$$V_{out,1}V_{out,2} = \left(V_1 + V_s\right)\left(V_2 + V_s\right)$$
$$= V_1V_2 + V_1V_s + V_2V_s + V_s^2. \tag{1.1}$$

The noise components in the receiver circuitries are statistically independent, and thus with sufficient time averaging the first three terms of (1.1) tend to zero, yielding

$$\overline{V_{out,1}V_{out,2}} = \overline{V_s^2}. \tag{1.2}$$

The correlation technique is useful in radio astronomy and earth remote sensing to achieve greater aperture sizes, but also inherent in the correlation process is the response only to self-luminous objects, which are sources of coherent radiation. Though

7

astronomical objects as well as humans are spatially incoherent, that is, the radiation from one point on the object is statistically independent of the radiation from another point, each point produces coherent radiation. This aspect can be useful in human presence detection. A person is a self-luminous source and much of the other radiation present in a cluttered outdoor environment is incoherent radiation from reflections and scatterings. Thus an ideal correlation radiometer (a radiometer with sufficient averaging time) should respond only to self-luminous objects, such as humans, while other radiation will be averaged to zero.

1.3 INFRARED SENSORS

Upon the advent of IR thermocouples and IR imagers, devices were created to detect human presence based on intrinsic human IR radiation. The ratio of energy emitted by an object compared to a perfect radiator (called a *blackbody*) of the same temperature is called the *emissivity*, and human skin emissivity in the infrared spectrum was found to be 0.997-0.999 [19]. Thus human skin is a near-perfect radiator in the IR region of the electromagnetic spectrum. Since the source of energy in the human body is of thermal origin the radiation is directly related to the temperature of the body. An object is measured radiometrically by its *brightness temperature* T_B, which is a quantity related to an object's physical temperature T and its emissivity e at a given frequency by $T_B = eT$. A contrast in brightness temperature can result from two cases: an object and its background have similar emissivities and the object has a higher temperature than the background, or the object and its background have similar temperatures but the background has a lower emissivity than the object.

Figure 1.1. IR image of a person in a cluttered outdoor environment. The person is in the center of the image.

IR devices work well in certain situations such as nighttime or indoor environments due strong thermal contrast as well as lack of sunlight. In an indoor environment a person's thermal signature in the IR band is dominant over most other sources of radiation and thus a person can be detected through his warm thermal signal contrasting with a cooler background. However, outdoors the IR radiation of the environment looks different. The IR emissivity of typical vegetation is 0.90-0.98 [20] and thus in environments where physical temperatures are on the order of human body temperature, vegetation will have a brightness temperature similar to that of a human. The peak wavelength of the sun's radiation is 500 *nm* which is just under the defined limit of IR wavelengths of 1 *mm* to 750 *nm* and since most metals reflect IR radiation very well, reflections from the sun can be extremely bright in cluttered outdoor environments, drowning out the signature from a human. In addition, treated wood has an IR emissivity of 0.89-0.94 [20], thus any wooden objects warming in the sun will also have a large brightness temperature which can further cause confusion. Figure 1.1 shows

an image from an IR camera of a person with a building in the background; of note are the objects that have brightness much larger than the human, as well as the fact that the level of emission from the person is nearly equivalent to that of other parts of the building.

My research has shown that millimeter-wave radiometers perform better then IR sensors in outdoor environments. Figure 1.2 shows comparisons of a 27.4 GHz total power radiometer and an IR sensor scanning across a human in an outdoor environment. The background of the test included the metal wall of a building to the right of the peak and a parking lot to the left. The total power detector has a noticeable peak when scanning the person between -20° and 0°, but the IR shows no indication of detection.
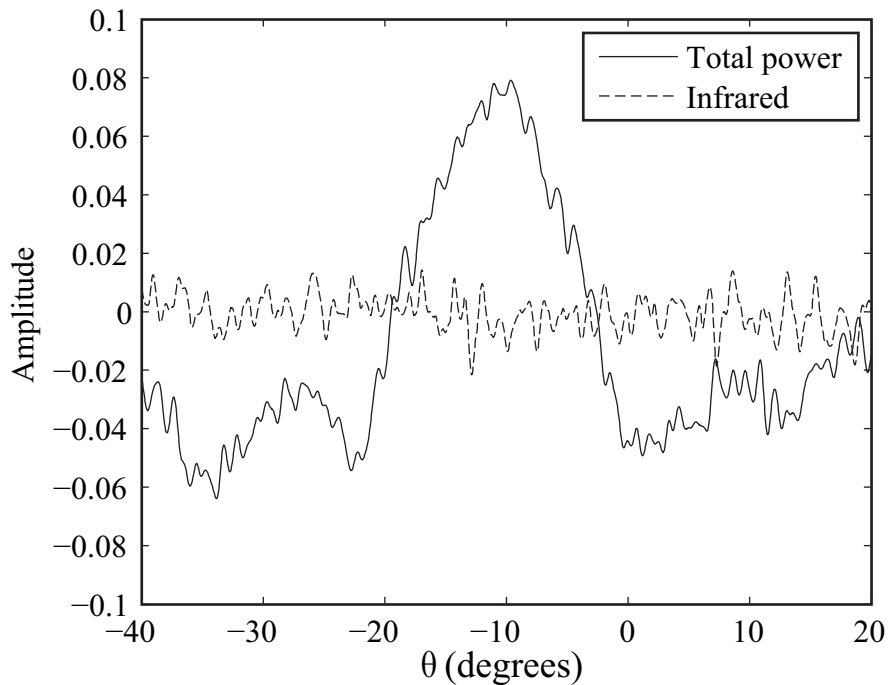
Figure 1.2. Comparison of IR and PMMW sensors scanning a human.

The use of millimeter-wave technology has another benefit over IR in that clothing of thickness on the order of 1 mm is effectively opaque at IR frequencies, suffering transmission attenuation of 22 dB through typical garment materials [5]. Power is related to temperature through Boltzmann's Law:

$$P = kT_B\Delta f, \qquad\qquad (1.3)$$

where $k = 1.38 \times 10^{-23}$ joule·K^{-1} is Boltzmann's constant and Δf is the detection bandwidth. Thus the power is proportional to the brightness temperature of the source and with 22 dB of power attenuation this translates to an observed brightness temperature 158 times lower. Thus IR sensors will have difficulty differentiating a clothed human from a typical outdoor background temperature. Even with clothing that has warmed to high temperatures the brightness temperature may still be low depending on the emissivity of the clothing material. Thus it is relatively simple to cover up a person's IR radiation signature by attenuating the radiation through layers of clothing. However, millimeter-wave frequencies have been shown to have less than 3 dB of attenuation up to 300 GHz and less than 1 dB attenuation at K_a-band through most garment materials [5].

1.4 SYSTEM CONCEPT – HUMAN PRESENCE DETECTING RADIOMETER

In this dissertation I present a method of human presence detection using passive millimeter-wave radiometry. To demonstrate this novel mode of human presence detection I present a system concept which uses a K_a-band radiometer in total power and correlation mode, a W-band total power radiometer and a Bayesian statistical detection classifier; for simplicity the system is referred to as the correlation radiometer or radiometer system. The radiometer utilizes three superheterodyne receivers, two at 27.4

GHz, the third at 95 GHz. The sensor suite is mounted to a rotating platform atop a semi-autonomous robot, the rotation giving the scanning beam system 360° coverage. The sensor signals are collected in an analog-to-digital converter and processed with a Naïve Bayesian statistical classifier, which analyzes the signals based on voltage level, width of detection peaks, and temporal correlation of each signal.

1.5 RESEARCH OBJECTIVES

The research presented in this dissertation serves to introduce the idea of using millimeter-wave radiometry to detect the presence of a human from a moving platform. Detection of human presence from a moving platform in outdoor environments is an unsolved problem and this dissertation presents one possible solution.

An additional goal of this dissertation is to investigate new methods of detection and classification in the data fusion of total power and correlation signals. The Bayesian formulation of detection and classification shows promising results with a simplistic implementation which allows for easy combination of additional sensors or additional signal statistics.

1.6 DISSERTATION ORGANIZATION

The detection method presented in this dissertation can be conceptually decoupled into the different regimes in which the relevant signals are generated, detected, or processed. The first regime is the generation of the thermal radiation by the human and is discussed in Chapter 2. After the radiation escapes the surface of the human, passing through clothing layers with minimal attenuation as discussed in Chapter 1, it traverses through the effectively free-space outdoor medium to the receiver. In the millimeter-wave

region radiation interacts minimally with air in most conditions; only during rain where the water droplets become significantly large compared to the wavelength does the radiation suffer attenuation. The radiation is detected by the correlation and total power receivers after transmitting through the air. The theoretical responses of the receivers are discussed in Chapter 3 and the system design, where the radiation is converted to digital signals, is discussed in Chapter 4. The general interferometer theory must be altered in the case of close-range human presence detection and these modifications to the theory are also discussed in Chapter 4.

Chapter 5 discusses the processing and conditioning of the digitized signals as well as the detection and classification algorithms. Two classification methods were investigated; first a heuristic classifier which showed promising results but which was too computationally expensive, and second a Bayesian formulation to signal classification which showed reliable detection capabilities and which was far less computationally expensive.

The detection method is evaluated by experimental validation in Chapter 6. Experimental setups are discussed and results are shown. The data sets resulting from the system experiments are shown to be imbalanced, with a small percentage of positive detections of humans. Performance metrics are discussed which pertain to imbalanced data sets and give a theoretical measure of the classifier performance. The practical performance of the classifier is demonstrated by analyzing the receiver operating curve of the correlation radiometer. Finally, the conclusion chapter discusses the contributions my research has made to the field and covers future directions of the research.

Chapter 2: Applying MMW Radiometry to Human Presence Detection

2.2 SOURCE OF HUMAN RADIATION

The radiation emitted by human is thermal in nature. In the infrared spectrum the thermal radiation detected originates from the outer layer of the skin, with a depth of a few wavelengths [19]. In the millimeter-wave region the radiation originates from the outer layer of the underlying tissue as well as the bulk of the skin. Using a simple model of the human body, this section shows that the majority of the radiation emitted by a human in the millimeter-wave region originates in the skin and the surface of the tissue beneath the skin.

The *optical depth* of a material or object at a frequency f is defined by [21]

$$\tau_f(s) = \int_{s_0}^{s} \alpha_f(s')ds',$$

(2.1)

where α_f is the spectral absorption coefficient of the material and the integral is taken along the depth of the material. In the microwave region at $f = 23.6$ GHz, the absorption coefficients of human skin and human blood are [22]

$$\alpha_{skin} \sim 6.35 \, cm^{-1},$$

(2.2)

$$\alpha_{blood} \sim 10 \, cm^{-1}.$$

(2.3)

It is difficult to model the human body while including organs, tissue, and blood, and as such I will approximate the human body as a layer of skin surrounding tissue

approximated as blood. Such a model is an oversimplification, although it will provide an approximation of how the radiation is generated. Also, the model is not wholly unreasonable because of the high blood content of most tissue and organs in the human body. The average thickness of human skin has been measured as $s_1 \sim 1$ mm [23], and the thickness of the torso from front to back is $s_2 \sim 18$ cm [24].

The optical depth of human skin is then

$$\tau_{skin} = \int_0^{s_1} \alpha_{skin} ds' = s_1 \alpha_{skin} = 0.635, \quad (2.4)$$

and the optical depth of the tissue is

$$\tau_{tissue} = \int_0^{s_2} \alpha_{blood} ds' = s_2 \alpha_{blood} = 180. \quad (2.5)$$

Since $\tau_{skin} < 1$, the skin is *optically thin,* while the tissue is *optically thick* since $\tau_{tissue} > 1$. This means that the majority of the photons originating in the tissue are absorbed before reaching the surface of the tissue; the radiation emitted comes from photons originating from the surface to a depth of a few *mean-free paths*. A mean-free path is the distance an average photon can travel through an absorbing material without being absorbed. The majority of the photons originating from the bulk of the skin are not absorbed, and thus are radiated outwards, along with those photons which are not absorbed in the tissue an eventually escape. Thus the human thermal radiation detected in the millimeter-wave region is generated from the surface of the tissue underneath the skin and from the skin itself.

2.3 RECEIVED HUMAN MMW RADIATION

The *spectral brightness* of a blackbody is given by Planck's radiation law:

$$I_f = \frac{2hf^3}{c^2} \frac{1}{e^{hf/kT} - 1},$$ (2.6)

where I_f = spectral brightness or spectral intensity ($W \cdot m^{-2} \cdot Hz^{-1} \cdot sr^{-1}$),

h = Planck's constant (6.63×10^{-34} joule·s),

f = frequency (Hz),

c = speed of light (3×10^8 m·s^{-1}),

k = Boltzmann's constant (1.38×10^{-23} joule·K^{-1}),

T = temperature (K).

Human body temperature is $T = 310.015$ K and at a frequency $f = 27.4$ GHz the argument of the exponential is $hf / kT = 4.24 \times 10^{-3}$. Since this is much less than unity the denominator can be approximated by $e^{hf/kT} - 1 \approx 1 + hf/kT - 1 = hf/kT$, and thus

$$I_f = \frac{2hf^3}{c^2} \frac{kT}{hf} = \frac{2f^2}{c^2} kT,$$ (2.7)

which is known as the *Rayleigh-Jeans approximation*. Figure 2.1 shows (2.6) over frequency at human body temperature. The Rayleigh-Jeans region to the left of the dotted line indicates the frequencies where (2.7) is valid. Over a narrow bandwidth $\Delta f \ll f$ the spectral brightness is approximately constant over the bandwidth and thus the *brightness*, given by I W·m^{-2}·sr^{-1}, is

$$I = \int_f^{f+\Delta f} I_f \, df \approx I_f \int_f^{f+\Delta f} df = \frac{2f^2}{c^2} kT \Delta f.$$ (2.8)

16
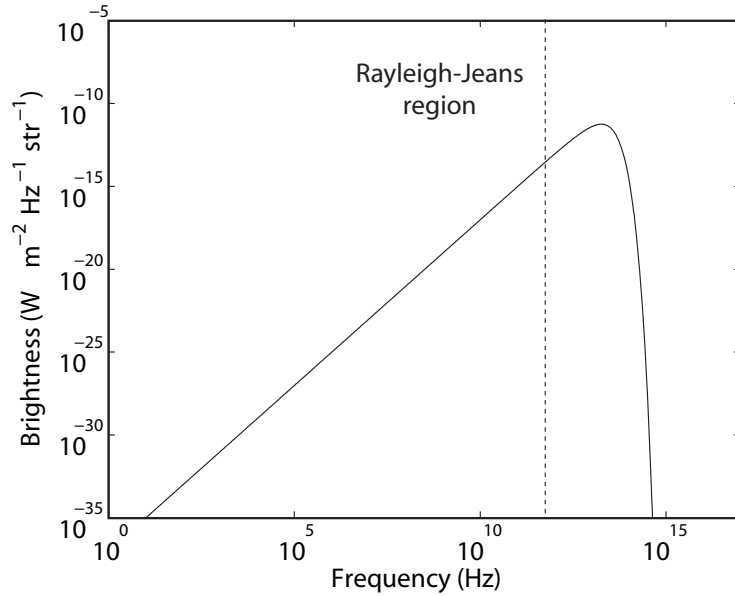
Figure 2.1. Radiation from a blackbody at the temperature of a human.

If the effective aperture of the transmitter is A_t the power received by an antenna of effective aperture A_r is given by

$$P_{bb} = \frac{1}{2} I A_r \frac{A_t}{R^2} = \frac{A_r A_t}{R^2} \frac{f^2}{c^2} kT\Delta f.$$
(2.9)

where R is the distance between the radiating source and the receiving antenna. The power given by (2.9) is that due to a blackbody radiating at a physical temperature T, indicated by the subscript bb. To relate this to a greybody the emissivity is used, defined by

$$e = \frac{T_B}{T},$$
(2.10)

17

where T_B is the *brightness temperature*, which is the blackbody equivalent radiometric temperature, or the temperature that a blackbody must be to radiate at the observed brightness. The previous equations assumed that $e = 1$, thus that $T = T_B$. Inserting (2.10) into (2.9) yields the received power from a radiating greybody:

$$P = e\frac{A_r A_t}{R^2}\frac{f^2}{c^2}kT\Delta f. \qquad (2.11)$$

If the person is close enough to the antenna that the antenna beamwidth β is not greater than the angular extent of the person, the person is *resolved* within the beam, and the preceding equations are accurate. However, as the person becomes more distant β becomes too wide to resolve the person and the self-luminous radiation becomes only a certain fraction of the brightness seen by the sensor. In such cases the brightness temperature seen by the antenna is no longer given simply by (2.10) and must be modified to include the effects of the antenna beamwidth.

The brightness given by (2.10) can be considered the *resolved brightness*, while the *unresolved brightness* is given by [12]

$$T_{B,u} = \frac{\Omega_s}{\Omega_r}eT, \qquad (2.12)$$

where Ω_s is the source solid angle and Ω_r is the antenna beam area which is given by [12]

$$\Omega_r = \frac{4}{3}\beta^2. \qquad (2.13)$$

18

Let the width of a person be given by w meters. The angular width χ of the person at a given range is then

$$\chi = 2 \tan^{-1}\left(\frac{w}{R}\right) \tag{2.14}$$

and the source solid angle can then be found by

$$\Omega_s = \pi\chi^2 = 4\pi\left[\tan^{-1}\left(\frac{w}{R}\right)\right]^2. \tag{2.15}$$

The point at which a person becomes unresolved can be found by setting (2.13) and (2.15) equal and solving for R. For a person of width $w = 0.3048$ m with $\beta = 0.066$ radian the resolution limit is $R_l = 7.0533$ m.
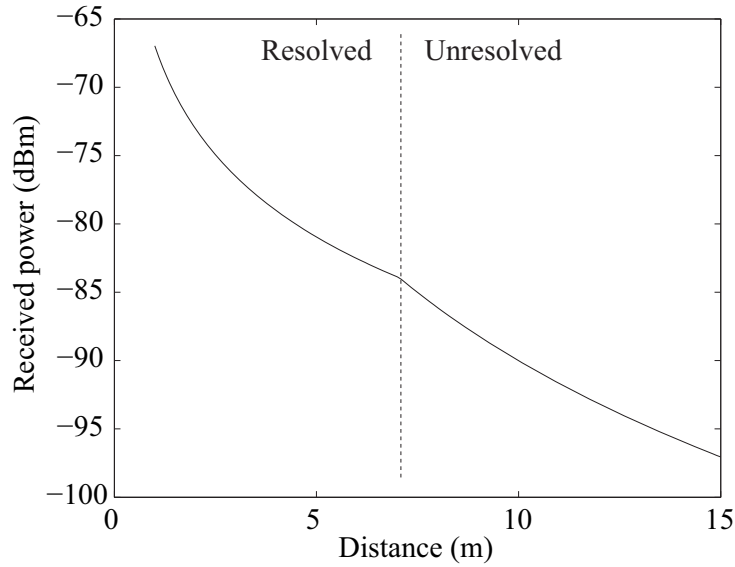
Figure 2.2. Received power from a radiating human

19

A range profile of the approximate received radiation from a human can now be found. The emissivity of a human in the K_a-band is approximately 0.65 [1]. Assuming the human body is an omni-directional radiator, the surface area of the skin can be used which is about 1.8 m^2 [25]. Given a bandwidth of $\Delta f = 500$ MHz, which satisfies that $\Delta f \ll f$, the received power in terms of distance R for a receiving antenna with a circular aperture of diameter 6 is shown in Figure 2.2.

Chapter 3: Theory of the Total Power and Correlation Responses

The response of the millimeter-wave sensors to the received radiation is discussed in this chapter. I begin by deriving the response if the total power receiver and follow by deriving the more complicated response of the correlation receiver and showing examples of each mode.

3.1 RESPONSE OF THE TOTAL POWER RECEIVER

The input power to the receiver system is a combination of the antenna noise power and the system noise power [16]:

$$P_{sys} = P_A + P_{rec} = kT_{sys}\Delta f, \qquad (3.1)$$

where

$$T_{sys} = T_A + T_{rec} \qquad (3.2)$$

is the system noise temperature, comprised of the antenna noise temperature T_A and receiver noise temperature T_{rec}; Δf is the system bandwidth. The noise power at the output of the IF amplifier is given by

$$P_{IF} = GkT_{sys}\Delta f \qquad (3.3)$$

where G is the system gain. Assuming that the output power of the IF amplifier is across a 1 Ω resistor yields

$$P_{IF} = \overline{V_{IF}^2}. \tag{3.4}$$

Following the IF amplifier is a detector diode with a power-sensitivity constant C_d. The output of the diode is given by $V_d = C_d V_{IF}^2$, and the average value is given by

$$\overline{V_d} = C_d \overline{V_{IF}^2} = C_d GkT_{sys}\Delta f. \tag{3.5}$$

The signal is then typically passed through a low-pass filter (LPF), which is the equivalent of averaging V_d over an interval $\tau = (2\Delta f_{LPF})^{-1}$, where Δf_{LPF} is the filter bandwidth. The voltage output of the LPF is then given by

$$\overline{V}_{out} = L_{LPF}C_d GkT_{sys}\Delta f, \tag{3.6}$$

where L_{LPF} is the loss of the LPF. Thus the output voltage of the total power radiometer is directly proportional to the input power P_{sys}, given in terms of the antenna temperature by (3.1) and (3.2). T_{rec} is measured in the lab [12, 16], while T_A is related to the brightness temperature of the observed scene through

$$T_A = \frac{P_A}{k\Delta f}, \tag{3.7}$$

where P_A is given by (2.11). Thus the output voltage of the total power receiver is directly related to the temperature of the observed scene.

In practice the output voltage of the filter is often in the range of microvolts and must be further amplified. The radiometer system uses op-amp based baseband amplifiers to provide an additional 50 dB of gain just prior to the LPFs. Because the signals being boosted are so low in voltage there is often a small dc bias that must be subtracted out to

keep the amplified signal within the limits of the op-amp and filter power rails. This is accomplished with an op-amp based differencing amplifier which subtracts a variable voltage from the amplified signal. Thus the total power output is given by

$$\bar{V}_{out} = GkT_{sys}\Delta f + V_{offset},\qquad(3.8)$$

where L_{LPF}, C_d, and the baseband amplifier gain has been included in G. An example of the total power response as a person crosses the antenna beam at varying distances is show in Figure 3.1. The person starts approximately 10ft from the radiometer, walks out to nearly 50ft and walks back. The background is the metal wall of a building.
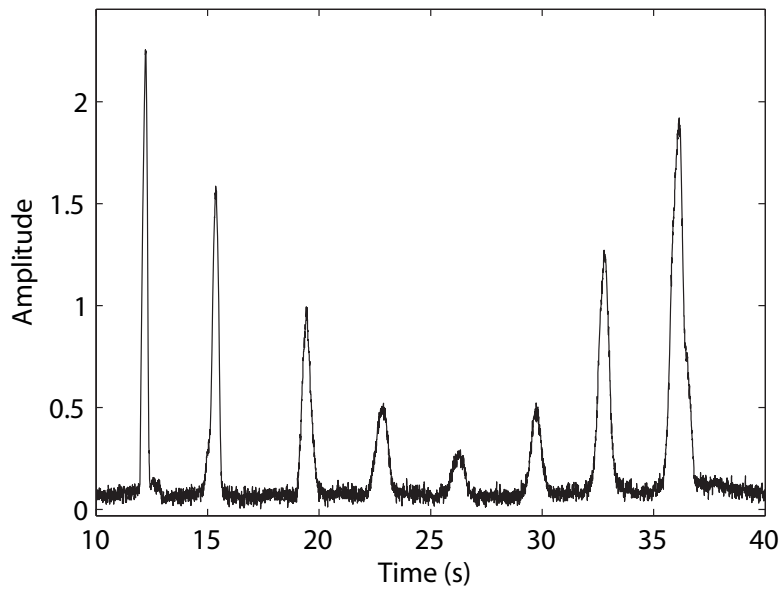
Figure 3.1. Total power response to a human crossing in front of the radiometer at varying distances.

3.2 RESPONSE OF THE CORRELATION RECEIVER

A simple correlation receiver consists of two identical total power receivers whose outputs are multiplied and integrated prior to any square-law detection. The frequency response of the multiplier due to a point source is proportional to

23
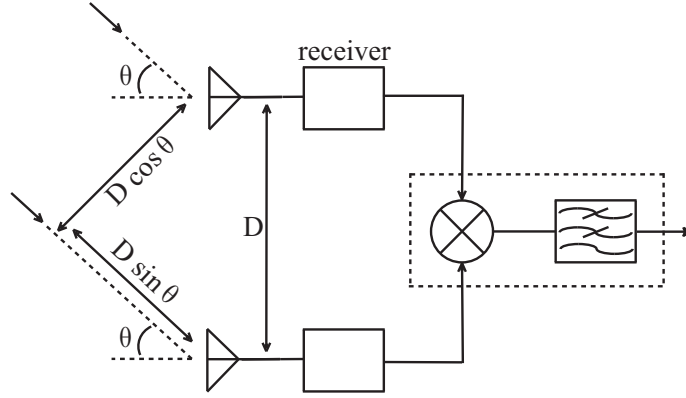
Figure 3.2. Geometry of a simple correlation radiometer.

$$F = 2\sin\left(2\pi ft\right)\sin\left[2\pi f\left(t - \tau_g\right)\right]$$
$$= 2\cos\left(2\pi f\tau_g\right) - 2\cos\left(2\pi ft\right)\cos\left[2\pi f\left(t - \tau_g\right)\right],$$

(3.9)

where

$$\tau_g = \frac{D}{c}\sin\theta$$

(3.10)

is the geometrical time delay between the reception of the signal on the two antennas and D is the antenna baseline, as seen in Figure 3.2. Following some trigonometric manipulation (3.9) becomes

$$F = \cos\left(2\pi f\tau_g\right) - \cos\left(4\pi ft\right)\cos\left(2\pi f\tau_g\right) - \sin\left(4\pi ft\right)\sin\left(2\pi f\tau_g\right).$$

(3.11)

Low-pass filtering (3.11) results in the *fringe pattern*, given by

$$F = \cos\left(2\pi f\tau_g\right) = \cos\left(\frac{2\pi D}{\lambda}\sin\theta\right).$$

(3.12)

24

Integrating over the pre-detection bandwidth Δf of the receiver centered at f_c gives an envelope to the fringe pattern, called the *fringe washing function.* Ideally the passband is rectangular which results in a sinc function envelope. The fringe washing function is further limited in angle by the antenna pattern A_θ, resulting in a receiver response given by

$$F\left(f_c\right) = A_\theta \cos\left(2\pi f_c D \sin\theta/c\right) \mathrm{sinc}\left(\pi\Delta f D \sin\theta/c\right). \qquad (3.13)$$

The fringe washing function is wide enough at the bandwidth Δf = 500 MHz that the angular limiting factor of the fringe washing function is the antenna pattern of the 6" lens antennas. In fact, for a given center frequency and bandwidth the fringe washing function is dependent only on the antenna baseline. It was calculated that the antenna pattern is the angular limiting factor of the fringe washing function if the baseline D < 130.75 cm, or 4.29 ft.

It is seen from (3.13) that the period of the fringes varies inversely with the quantity $fD/c = D/\lambda$ and that the fringe width is given by λ/D and both are independent of the bandwidth Δf. However, the fringe washing function is dependent on Δf as well as D through τ_g. The placement of the baseline and bandwidth variables in (3.13) means that long baselines or wide bandwidths will result in narrow fringe washing functions.

Figure 3.3 shows the fringe pattern over angle, and Figure 3.4 shows how the fringe washing function angularly limits the fringe pattern. In radio astronomy the fringe washing function is created to be narrower than the antenna pattern, however in this case the antenna pattern is the angularly limiting factor, as seen in Figure 3.5. The full response is then show in Figure 3.6.
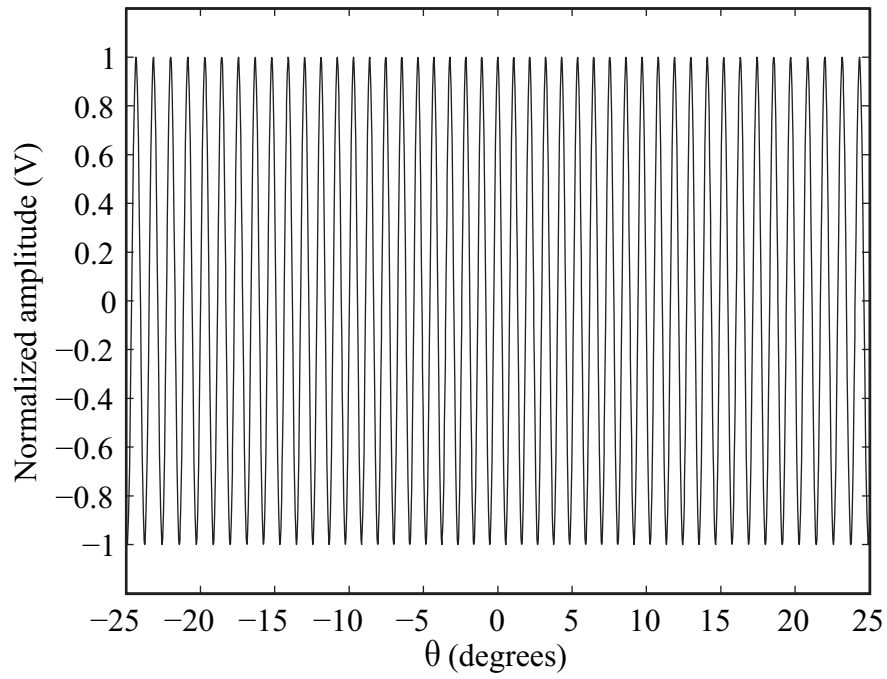
Figure 3.3. Fringe pattern.
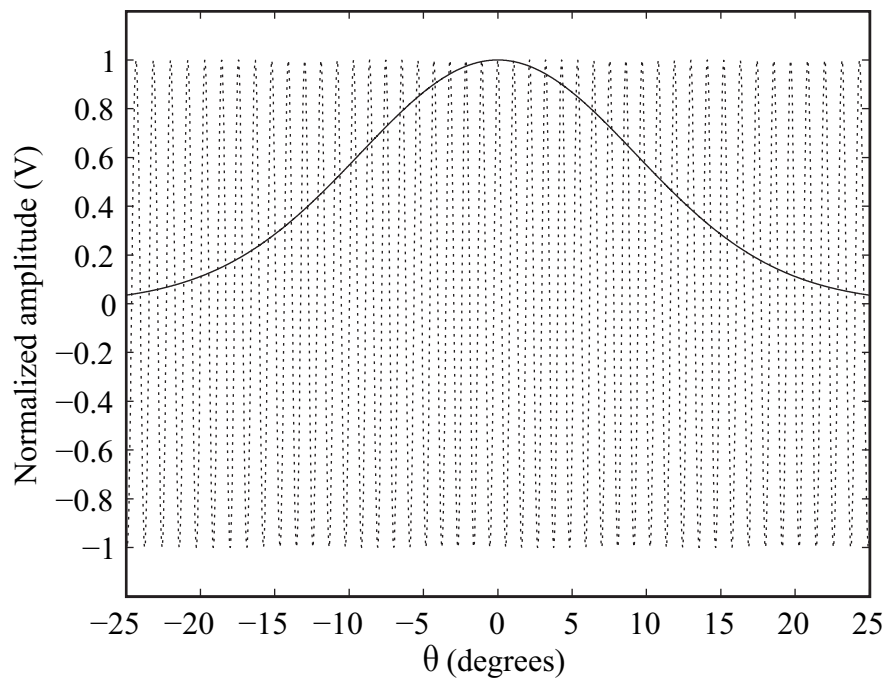
Figure 3.4. Fringe washing function.
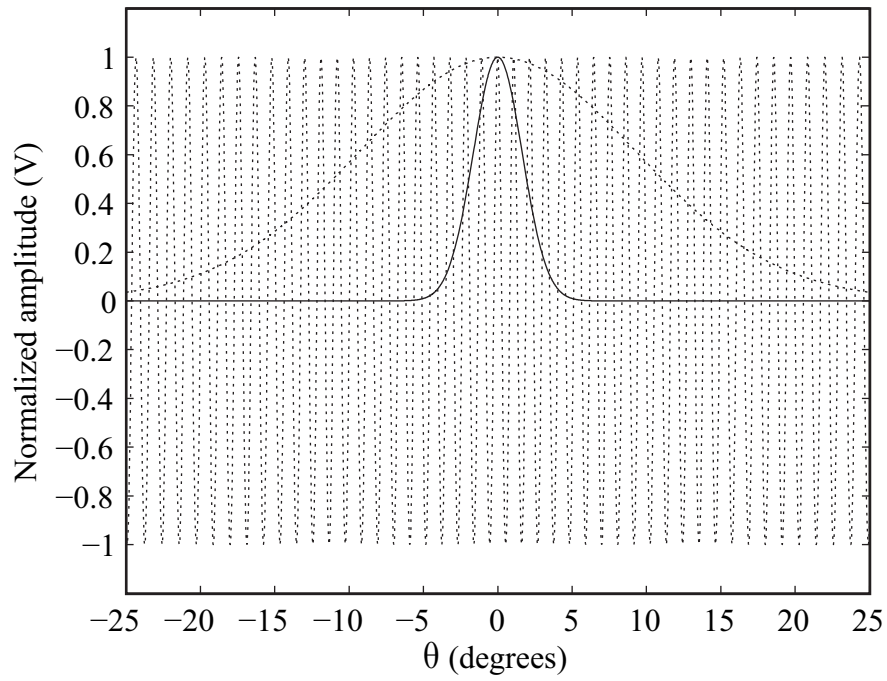
Figure 3.5. Antenna pattern.
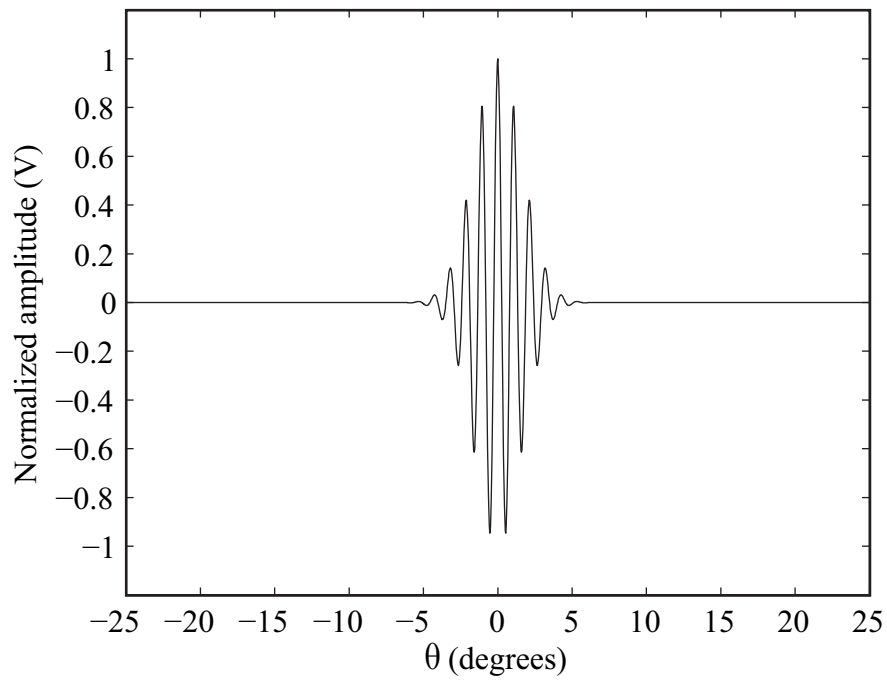
Figure 3.6. Resulting correlation response.

27
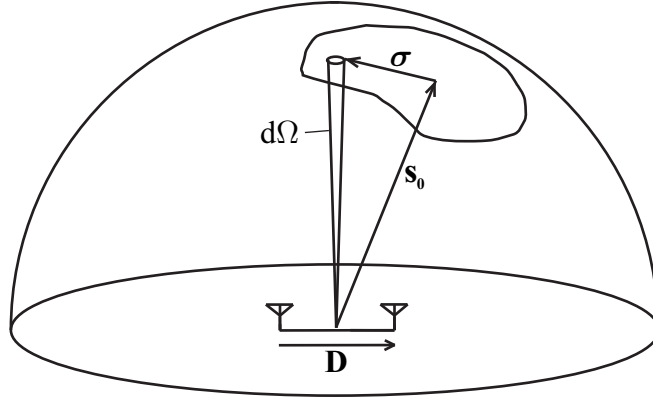
Figure 3.7. Geometry describing the correlation response to a distributed source (after [14]).

The power received by the antenna from a point source is given by

$$P_A = \frac{1}{2} A_r I_f \Delta f.$$
(3.14)

For an extended source whose center is located at $\mathbf{s}_0$, as seen in Figure 3.7, an element of solid angle $d\Omega$ at position $\mathbf{s} = \mathbf{s}_0 + \boldsymbol{\sigma}$ contributes a component of power given by

$$P_A = \frac{1}{2} A(\boldsymbol{\sigma}) I(\boldsymbol{\sigma}) \Delta f \, d\Omega.$$
(3.15)

With equal responses on each antenna the correlator response is proportional to the received power and the fringe term:

$$r \propto A(\boldsymbol{\sigma}) I(\boldsymbol{\sigma}) \Delta f \cos\left(2\pi f_c \tau_g\right) d\Omega.$$
(3.16)

Let the vector $\mathbf{D}_\lambda$ represent the antenna baseline in wavelengths. Then $f_c \tau_g = \mathbf{D}_\lambda \cdot \mathbf{s} = \mathbf{D}_\lambda \cdot (\mathbf{s}_0 + \boldsymbol{\sigma})$ and thus

28

$$r = \Delta f \int_{4\pi} A(\boldsymbol{\sigma}) I(\boldsymbol{\sigma}) \cos\left[2\pi \mathbf{D}_\lambda \cdot (\mathbf{s}_0 + \boldsymbol{\sigma})\right] d\Omega$$

$$= \Delta f \cos\left(2\pi \mathbf{D}_\lambda \cdot \mathbf{s}_0\right) \int_{4\pi} A(\boldsymbol{\sigma}) I(\boldsymbol{\sigma}) \cos\left[2\pi \mathbf{D}_\lambda \cdot \boldsymbol{\sigma}\right] d\Omega \qquad (3.17)$$

$$- \Delta f \sin\left(2\pi \mathbf{D}_\lambda \cdot \mathbf{s}_0\right) \int_{4\pi} A(\boldsymbol{\sigma}) I(\boldsymbol{\sigma}) \sin\left[2\pi \mathbf{D}_\lambda \cdot \boldsymbol{\sigma}\right] d\Omega.$$

The complex visibility function is defined as [14]

$$\mathcal{V} = |\mathcal{V}| e^{j\phi_v} = \int_{4\pi} A_N(\boldsymbol{\sigma}) I(\boldsymbol{\sigma}) \exp\left(-j2\pi \mathbf{D}_\lambda \cdot \boldsymbol{\sigma}\right) d\Omega, \qquad (3.18)$$

where A_N is the normalized antenna pattern given by $A_N(\boldsymbol{\sigma}) = A(\boldsymbol{\sigma})/A_0$ where A_0 is the antenna collecting area in the direction $\mathbf{s}_0$. Separating (3.18) into real and imaginary components and inserting into (3.17) yields

$$r = \Delta f \cos\left(2\pi \mathbf{D}_\lambda \cdot \mathbf{s}_0\right) |\mathcal{V}| \cos\phi_v A_0 + \Delta f \sin\left(2\pi \mathbf{D}_\lambda \cdot \mathbf{s}_0\right) |\mathcal{V}| \sin\phi_v A_0$$

$$= A_0 \Delta f |\mathcal{V}| \cos\left(2\pi \mathbf{D}_\lambda \cdot \mathbf{s}_0 - \phi_v\right), \qquad (3.19)$$

which is the general response of the correlation receiver to a distributed source. Equation (3.19) is expressed as the fringe pattern of a hypothetical point source multiplied by the complex visibility function. As defined in (3.18) the visibility has a Fourier transform relationship with the brightness. Thus an inverse Fourier transform of the visibility results in a quantity proportional to the observed brightness.

A more general expression for the correlation response must include effects of phase from the receivers as well as the geometrical time delay. Let the frequency responses of two receivers be given by $H_1(f)$ and $H_2(f)$. The frequency f is that at the input of the correlator while the input to the antennas is $f_{LO} - f$ since the system has two lower-sideband superheterodyne receivers. The phase delays through the receivers are

29

designated ϕ_1 and ϕ_2 where negative values indicate phase delays. Assuming that the visibility does not vary significantly over the receiver bandwidth, the response is given by

$$r = \mathrm{Re}\left\{ A_0 |\mathcal{V}| \int_0^\infty H_1(f) H_2^*(f) \exp\left(j(\phi_1 - \phi_2 - \phi_v)\right) df \right\}. \tag{3.20}$$

If receiver 1 is designated the delay reference the signal reaching the antenna on receiver 2 undergoes a geometrical time delay of τ_g and thus a phase delay of

$$\phi_1 = 2\pi f_c \tau_g + \theta_1, \tag{3.21}$$

where θ_1 is the local oscillator phase. The signal reaching receiver 1, being the reference, does not undergo a geometrical time delay, thus the phase delay is given by the LO phase:

$$\phi_2 = \theta_2. \tag{3.22}$$

The correlator output is then given by

$$\begin{aligned} r = \mathrm{Re}\Big\{ A_0 |\mathcal{V}| &\exp\left(-j\left[2\pi f_c \tau_g + (\theta_1 - \theta_2) - \phi_v\right]\right) \\ &\times \int_0^\infty H_1(f) H_2^*(f) \exp\left(j2\pi f \tau_g\right) df \Big\}. \end{aligned} \tag{3.23}$$

In general, the instrumental gain factor $G = |G|\exp(j\phi_G)$ is defined such that

$$\begin{aligned} A_0 \int_0^\infty H_1(f) H_2^*(f) \exp\left(j2\pi f \tau_g\right) df &= G(\tau_g) \exp\left(j2\pi f_c \tau_g\right) \\ &= |G(\tau_g)| \exp\left[j\left(2\pi f_c \tau_g + \phi_G\right)\right]. \end{aligned} \tag{3.24}$$

30

Thus, the general response of the lower-sideband correlation receiver including phase effects is given by

$$r = |\mathcal{V}| \left| G\left(\tau_g\right) \right| \cos\left[2\pi f_c \tau_g + \left(\theta_1 - \theta_2\right) - \phi_\upsilon - \phi_G\right]. \tag{3.25}$$

The variation of G over the geometrical time delay results in the fringe washing function, while the fringe pattern results from the cosine term. The phase ϕ_G of the instrumental gain factor is due to the difference in phase of the two receivers, from the phase delays of the receiver amplifiers, filters, and other components. This is kept separate from the LO phases only because they enter into an upper-sideband receiver with opposite sign. System two is an upper-sideband system, and the response is given by

$$r = |\mathcal{V}| \left| G\left(\tau_g\right) \right| \cos\left[2\pi f_c \tau_g + \left(\theta_1 - \theta_2\right) - \phi_\upsilon + \phi_G\right]. \tag{3.26}$$

Measurement of the system phase delay results in a quantity which is a combination of the LO and component phase delays, and in this case it is useful to use the correlation response with a total system phase delay

$$\phi_{sys} = \left(\theta_1 - \theta_2\right) \pm \phi_G \tag{3.27}$$

resulting in an expression for the correlation response given by

$$r = |\mathcal{V}| \left| G\left(\tau_g\right) \right| \cos\left[2\pi \left(f_{LO} \pm f_{IF}\right)\tau_g - \phi_\upsilon + \phi_{sys}\right]. \tag{3.28}$$

where f_{IF} is the intermediate frequency after down-conversion and the positive signs in (3.27) and (3.28) are used for the upper-sideband receiver.

31

Chapter 4: System Concept and Adaptation to Human Presence Detection

4.1 DESIGN OBJECTIVES

The use of a millimeter-wave correlation receiver is novel for the application of human presence detection. Therefore, while the hardware system is in general based on established research, the presence detection system must be designed with the new application of human presence detection as the focal point. Modifications are necessary to adapt the theory to the short ranges and different types of detection in human presence detection.

The sensitivity of the correlation radiometer must be analyzed in the context of human presence detection to ensure validity of the system radiometric sensitivity. The novel use of the sensor as a rotating, scanning beam system makes the determination of the correlation fringe frequency important for signal processing, and the projected baseline must be determined to ensure validity of the Fourier inversion of the measured visibility.

The ranges of the detection system are small compared to radio astronomy or Earth remote sensing, and to detect humans at shorter ranges the antennas are angled inwards. Thus the phase must be analyzed to ensure that far-field conditions are not violated. In addition, the spatial resolution of the correlation mode must be determined in order to calculate the dwell time of the sensor, which affects the radiometric resolution.

Figure 4.1. Correlation radiometer atop the mobile platform. The black antennas feed the K_a-band radiometer.

4.2 HARDWARE DEVELOPMENT

4.2.1 Overview

Figure 4.1 shows the entire radiometer system atop the mobile platform. The system design is based on a two-element correlation interferometer. The voltage output of the pre-detection hardware is divided by a power-splitter to facilitate both the total power and correlation detection modes. Two receivers are used and the outputs of each are

multiplied and integrated to provide the correlation detection mode. Figure 4.2 shows the component schematic of the receiver. Because both receivers are identical in structure with minor variations in component parameters, one receiver will be described in the following sections.
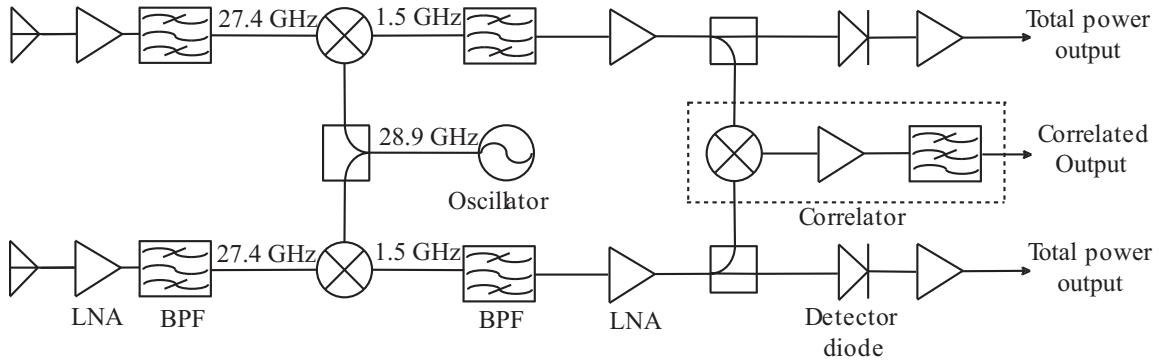
Figure 4.2. Correlation radiometer component schematic.

4.2.2 Antenna

The antenna used on each receiver is a Gaussian optical lens antenna with a 6" diameter lens and gain of 32.7 dBi. The radiation patterns of the antennas are circularly symmetric with half-power beamwidths of 3.876° in azimuth and 3.759° in elevation. In order to use the antenna pattern in theoretical simulations it was approximated by a $\cos^x \theta$ directivity function [26]. This simulates only the main beam of the antenna and therefore the figures used to match the simulated pattern to the actual pattern were the 3-dB beamwidths. While only the main beam is simulated, this approximation is valid since the sidelobes of the measured pattern are greater than 30 dB lower than the main beam. The approximating functions that most closely matched the measured values from the data sheet were $\cos^{1210} \theta$ for the azimuth pattern and $\cos^{1285} \theta$ for the elevation pattern. The resulting simulated azimuth HPBW is 3.8772° with an error of 0.0003% from the

34

measured value; the simulated elevation HPBW is 3.762° with an error of 0.0008%. The simulated antenna patterns are shown in Figure 4.3.
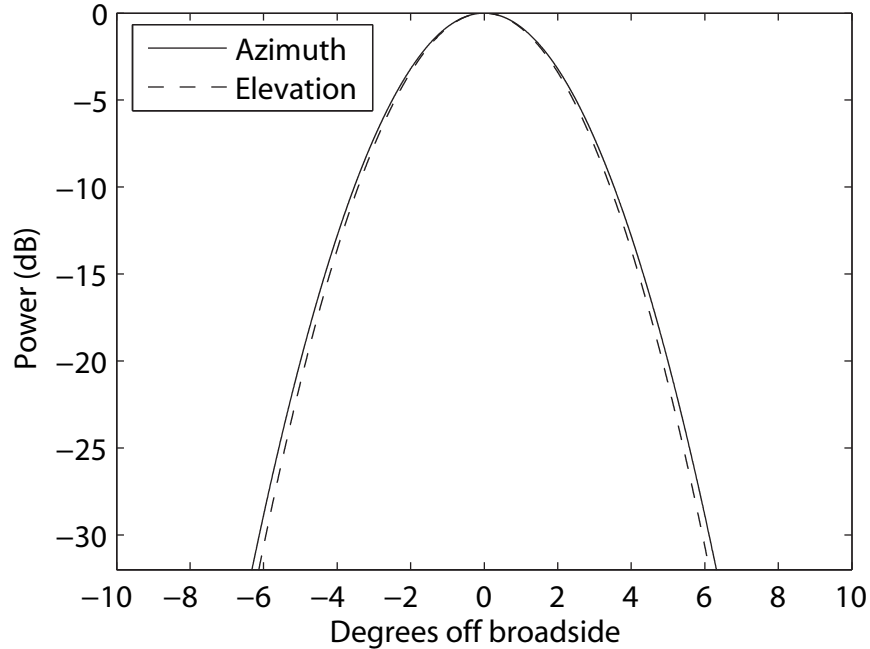
Figure 4.3. Simulated antenna patterns.

4.2.3 Pre-Detection Hardware

The hardware front-end of the detection system consists of two independent superheterodyne receivers of identical structure. The pre-detection hardware consists of components prior to detection through either a detector diode for the total power response, or the analog correlator for the correlation response.

The receiver is a lower-sideband receiver and has an RF center frequency given by $f_{c,RF}$ = 27.4 GHz, an LO frequency f_{LO} = 28.9 GHz, and an IF center frequency $f_{c,IF}$ = 1.5 GHz. The antenna used is a Gaussian optical lens antennas with a diameter of 6 inches, HPBW = 3.8° and a gain of 32.7 dBi. Following the antenna is a flexible coaxial cable with a loss of 0.15 dB which is connected directly to the RF LNA which has a gain

of 32 dB and a noise figure of 3.2 dB. The pre-detection bandwidth is Δf_{pre} = 500 MHz and is set by the RF band-pass filter (BPF) which follows the LNA. The output of the BPF is mixed down to the IF where another BPF is located with a bandwidth of 500 MHz centered on $f_{c,IF}$. Following the IF BPF are two cascaded LNAs giving a total of 63 dB gain. The LNA output is split; one output is sent to a detector diode which produces the total power response, the other combined with the output of the second receiver through a mixer which provides the multiplication part of the correlation. There are then three voltage signals: total power one, total power two, and correlation, and each are sent to a baseband circuit which provides additional amplification of 50 dB as well as low-pass filtering of the signals.

4.2.4 Post-Detection Hardware

The amplification is achieved using four cascaded op-amps, as seen in Figure 4.4, and is divided into two sections of two op-amps each. The purpose of the first section is to zero out the input signals. Despite an RF gain of nearly 80 dB up to this point, the input signal fluctuations are still in the microvolt range and must be amplified to the range of volts in order to clearly differentiate them from amplifier noise. A voltage of approximately −100 mV was measured on the output of the detector diodes under ambient conditions and amplifying this would put the value off the range capable of the op-amps. Therefore the input to the baseband amps must be offset to zero before the amplification [27]. The first op-amp has a gain of 1.5 and following this is a differential amplifier subtracting up to −120 mV from the total power channels. The detector diodes are inverting in nature and hence the negative signs on the preceding values. A voltage of approximately 10mV was measured on the output of the correlation channel and its differencing amplifier subtracts up to +120 mV. These differencing values are connected

36

to 10 kΩ potentiometers and were thus adjusted until the outputs of the first baseband stages were as close to DC as possible. This was done before the full system assembly and the potentiometers are not accessible during operation however the second amplifier stage also contains 10kΩ pots which are adjustable during operation. Thus the first offset adjustment is used to manipulate the output voltages to the general range desired and the second offsets are used to fine-tune the voltage levels.
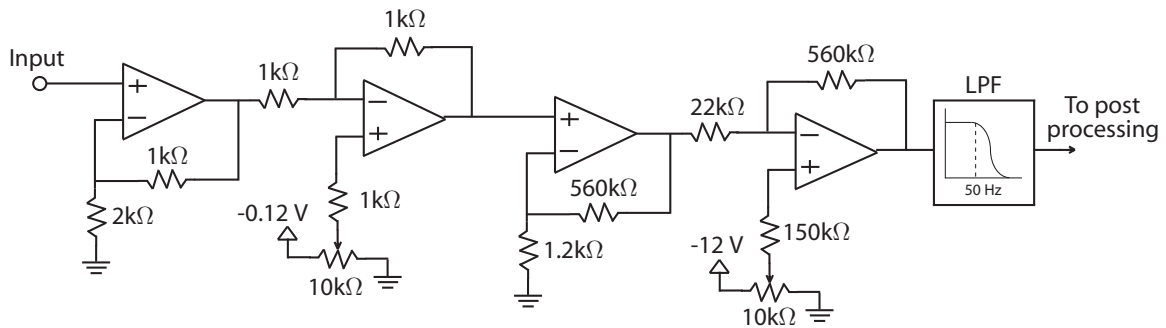
Figure 4.4. Baseband amplifier hardware

The second stage is identical in layout to the first stage except the total stage gain is 40.7 dB for the total power channels and 53.4 dB for the correlation (the 22 kΩ resistor is replaced with a 1.2 kΩ for the correlation channel). The extra gain on the correlation channel is needed to compensate for the 12 dB conversion loss of the mixer. The differencing value for the secondary offset is $-12\,\mathrm{V}$ for the total power channels and $+12\,\mathrm{V}$ for the correlation.

The LPFs used are 4-pole Butterworth filters and provide the post-detection bandwidth of $\Delta f_{post,tp}$ = 500 Hz for the total power channels and $\Delta f_{post,cr}$ = 2 kHz for the correlation signal. The LPF provides the integration of the correlation process.

37

4.2.5 A/D Converter and Processing

The analog outputs of the radiometer are passed to a Texas Instruments MSP430 microprocessor which has a 12 bit-precision analog-to-digital converter. The correlation and three total power signals are all sampled a rate of 2048 S·s^{-1}. The digitized signals are passed to a USART on the MSP430 and then to an FTDI USB-to-Serial microchip. The FTDI chip allows the MSP430 to be physically linked to the processing computer through a simple USB cable while the making use of the straightforward serial communication protocol.

The digitized signals are recorded on an OQO Model 2 computer. The OQO is a small-form-factor PC chosen for its small size of 5.6 in x 3.3 in x 1.0 in. Following an experiment the data are analyzed and the detection algorithms are run using MATLAB.

Figure 4.5 shows the K_a-band correlation radiometer system with the phase shifter for each channel mounted to the top. The phase shifters are used to calibrate ϕ_{sys} to eliminate the phase error between the channels. The baseband hardware is shown in Figure 4.6 with the baseband circuit board containing the op-amp amplifiers and low-pass filters. The mixer to the right performs the analog multiplication for the correlation channel. Underneath the baseband hardware is the IF hardware, shown in Figure 4.7, with the band-pass filters on the left and the LNAs (two per channel) on the right. Finally, the RF hardware is shown in Figure 4.8, with the antenna inputs on the right connected to a LNA, then a BPF and then the mixer which performs the down-conversion.
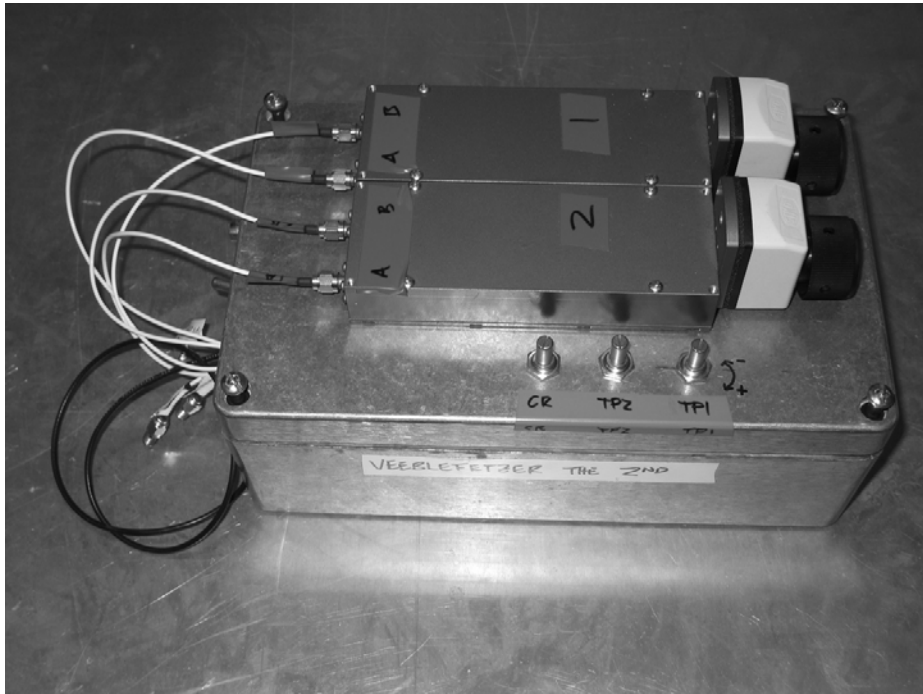
Figure 4.5. Correlation radiometer hardware case.
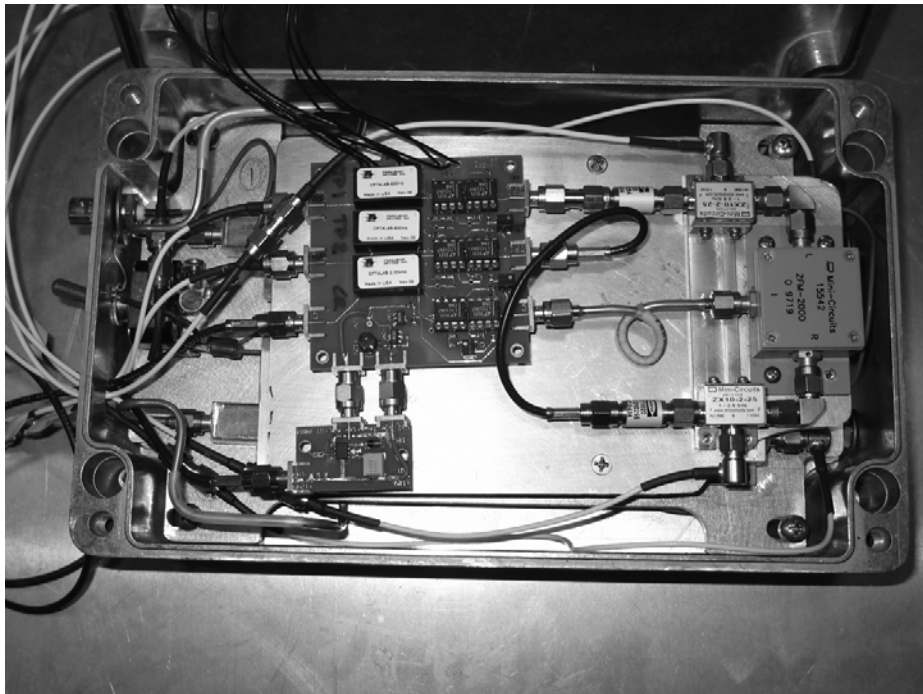
Figure 4.6. Baseband hardware.
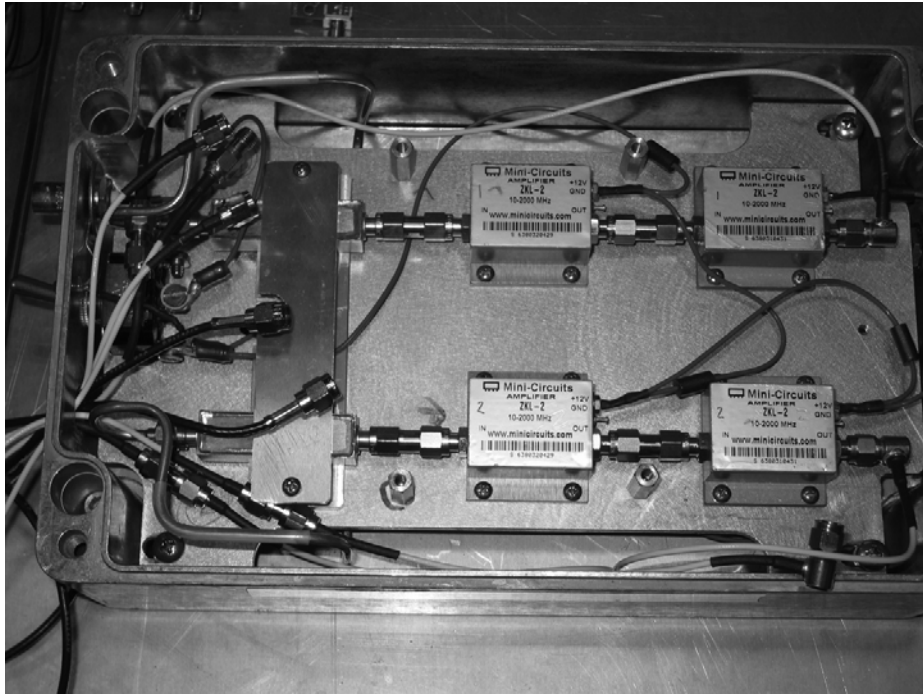
Figure 4.7. Correlation radiometer IF components.
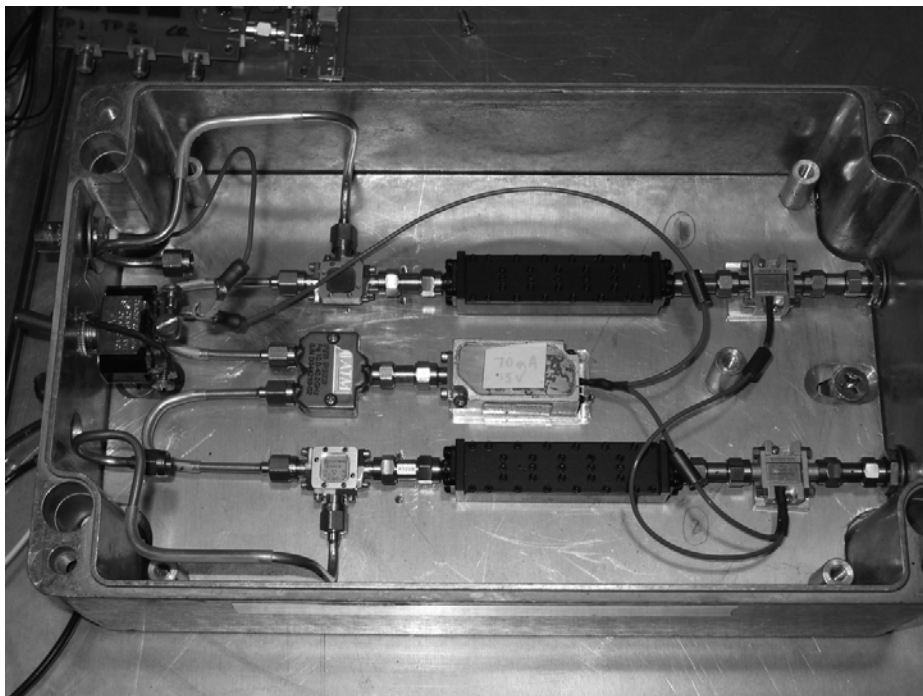
Figure 4.8. RF components.

4.3 NOISE FIGURE AND SYSTEM EQUIVALENT TEMPERATURE

The system noise figures were calculated using the Y-factor method [28]. The antennas were replaced with a noise source with an excess noise ratio (ENR) of 12.4 dB at 27.4 GHz. The ENR is defined by

$$ENR_{dB} = 10\log_{10}\frac{T_{ne} - T_0}{T_0},$$ (4.1)

where $T_0 = 290$ K and T_{ne} is the effective noise temperature of the noise source, related to its noise temperature T_a by $T_{ne} = T_a(1-|\Gamma|^2)$ where Γ is the reflection coefficient of the noise source [29].

Because temperature fluctuations in the RF amplifiers can cause small gain variations, the system was run for a period of time to allow the temperatures to equalize. Following this the voltages of all three channels were recorded. The Y-factor is a ratio of two noise power levels, one power level measured with a noise source on and the other with the noise source off. Because the total power channels are detected with square-law detectors the voltage output is linearly related to the input power. Likewise the correlation output is the multiplication of two noise voltage levels by the mixer and thus gives a voltage signal which is also linearly related to the power. The Y-factor for each channel is the ratio of the output voltage with noise source on (V_H) to the output voltage with the noise source off (V_L) and is given by

$$Y = \frac{V_H}{V_L}.$$ (4.2)

The voltage outputs represent the noise power of the system N_{sys} plus the noise power of the noise source, whether it is on or off: $V_{H,L} = N_{H,L} + N_{sys}$. The thermal noise power of a device is given by $N = kTB$ where k is Boltzmann's constant, T is the noise temperature and B is the bandwidth [29]. Since N is proportional to T the Y-factor can then be given as

$$Y = \frac{N_H + N_{sys}}{N_L + N_{sys}} = \frac{T_H + T_{sys}}{T_L + T_{sys}}. \qquad (4.3)$$

Rearranging, the system temperature can be given in terms of Y by

$$T_{sys} = \frac{T_H - YT_L}{Y - 1}. \qquad (4.4)$$

The noise figure is then given by

$$F = 10\log_{10}\left(1 + \frac{T_{sys}}{T_0}\right). \qquad (4.5)$$

The noise figures for each sensor are given in Table 4.1.

Table 4.1. Radiometer sensor noise figures.

	Sensor			
	Correlation	Total Power $K_{a,1}$	Total Power $K_{a,2}$	Total Power W
Noise Figure (dB)	3.09	6.71	7.20	6.90

4.4 SYSTEM ADAPTATION TO HUMAN PRESENCE DETECTION

The application of the theory of the correlation radiometer to human presence detection requires the modification of certain properties. The synthesized beam, sensitivity, fringe frequency, projected baselines, far-field phase approximation, spatial resolution and dwell time are analyzed in the following sections.

4.4.1 Point Source Response and Synthesized Beam

If the radiometer views a point source, the spectral radiance $I(\sigma)$ reduces to a delta function $\delta(\sigma)$ and the integral in (3.18) reduces to the normalized antenna pattern. If $H(f)$ is an ideal square passband of bandwidth Δf, (3.24) reduces to the antenna pattern A_0 multiplied by a sinc function with argument $D\sin\theta\Delta f/c$ where D is the baseline distance. If ϕ_{sys} is also negligible, either by design or calibration, the response of the two-element interferometer to a radiating point source is given by

$$r_p = A(\theta)\text{sinc}(D\sin\theta\,\Delta f/c)\cos(2\pi f_c D\sin\theta/c). \qquad (4.6)$$
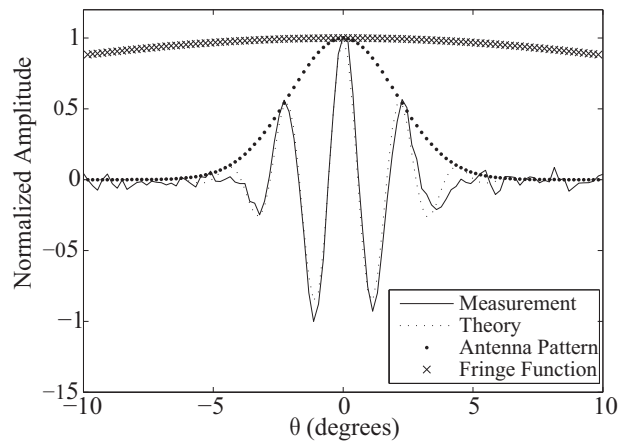
Figure 4.9. Theoretical and measured point source responses for the correlation radiometer.

43

The expression in (4.6) is compared to a point source measurement of the correlation radiometer in Figure 4.9. The correlation radiometer has and $D = 27.94$ cm for the point source measurement. Note that the response is angularly limited by the antenna pattern which has half-power beamwidth $\beta = 3.8°$. In most radio astronomy and Earth remote sensing applications it is desirable to have the fringe function narrower than the antenna pattern. This creates a synthesized beam which can achieve greater angular resolution than the individual antennas. In the case of human presence detection the goal is to exploit the coherence of the electromagnetic field produced by self-luminous objects. Because of this and the availability of antennas with beams narrow relative to the application of human and object detection, narrow synthesized beams are less important.

4.4.2 Sensitivity

The sensitivity of a two-element correlation radiometer is the minimum detectable change in flux density and in general is given by [30]

$$\Delta S = \sqrt{\frac{S_T^2 + S_C^2 + S_T\left(SEFD_1 + SEFD_2\right) + SEFD_1 SEFD_2}{2\Delta f \tau}},\qquad (4.7)$$

where τ is the integration time, S_T is the total flux density at the two antennas (assumed to be equal), and S_C is the correlated flux density between the antennas[†]. If the received radiation is perfectly correlated, $S_C = S_T$, otherwise $S_C < S_T$. The system equivalent flux density, denoted $SEFD_i$ for receiver i = 1, 2, is related to the receiver system temperature and is typically many times greater than the flux density in radio astronomy applications. In such a case only the $SEFD_1 SEFD_2$ term of (4.7) is important.

[†] Expression (4.7) is derived in Appendix A.

The *SEFD* is defined as [30]

$$SEFD = \frac{2kT_{sys}}{A_{ant}},$$ (4.8)

where k = 1.38 $\times 10^{-23}$ joule·K^{-1} is Boltzmann's constant and A_{ant} is the antenna collecting area. The observed flux density is given by [12]

$$S_T = \frac{2kT_A}{A_{ant}},$$ (4.9)

where the antenna temperature is given in terms of the source temperature T_S and antenna pattern by

$$T_A = \frac{A_{ant}}{\lambda^2} \iint T_S(\theta,\phi) A(\theta,\phi) d\Omega.$$ (4.10)

For an indoor environment the source temperature can be assumed to be constant with angle, and is typically 290 K. Outdoors a constant temperature is an idealized case, but an ambient temperature of 290 K is within an order of magnitude of typical conditions and is used here as an approximation. In this case (4.10) reduces to

$$T_A = 290 \frac{A_{ant}}{\lambda^2} \iint A(\theta,\phi) d\Omega.$$ (4.11)

In typical remote sensing applications such as radio astronomy the antenna beams are narrow enough that $T_A \ll T_{sys}$ and thus, through (4.8) and (4.9), $S_T \ll SEFD$. The sensitivity given by (4.7) then reduces to

$$\Delta S = \sqrt{\frac{SEFD_1 SEFD_2}{2\Delta f \tau}}. \tag{4.12}$$

If the two receivers are identical,

$$\Delta S = \frac{SEFD}{\sqrt{2\Delta f \tau}}. \tag{4.13}$$

In terms of temperature, the sensitivity can be written

$$\Delta S = \frac{2k}{A_{ant}} \frac{T_{sys}}{\sqrt{2\Delta f \tau}} = \frac{2k}{A_{ant}} \Delta T, \tag{4.14}$$

and the temperature sensitivity is

$$\Delta T = \frac{T_{sys}}{\sqrt{2\Delta f \tau}}. \tag{4.15}$$

The measured system temperature of the correlation radiometer is 301 K and the antenna collecting area is 6.1×10^{-3} m^2 giving $SEFD = 1.36 \times 10^{-18}$ W·m^{-2}·Hz^{-1} from (4.8). The antennas have $\beta = 3.8°$ at a wavelength of 1.1 cm giving $S_T = 3.45 \times 10^{-20}$ W·m^{-2}·Hz^{-1} from (4.9) and (4.11), and thus $S_T \ll SEFD$ and (4.12) - (4.15) are valid.

With the baseband LPF bandwidth of 2 kHz the resulting sensitivity is 426 mK. The relatively high cutoff frequency of the baseband filter allows for fringe frequencies resulting from fast rotation rates. The signal is filtered around the fringe frequency with a bandwidth proportional to the 3dB width of a simulated spectral point source response generated with equal rotation rate and results in a lower sensitivity. After estimation of

the fringe frequency, the signal is filtered around it resulting in sensitivities in the range of 150-400 mK. The sensitivities of the K_a-band total power radiometer modes were 477 mK and 550 mK.

4.4.3 Fringe Frequency

The fringe frequency is the centroid of the correlation frequency response and is dependent on the phase of the fringe pattern in (4.6):

$$FP = \cos\left(2\pi \frac{f_0}{c} D \sin\theta\right). \tag{4.16}$$

For a scanning radiometer the angle variable θ can be given by the rotation rate ω rad·s^{-1} multiplied by the time t. The phase of the fringe pattern is then

$$\phi_F = 2\pi \frac{f_0}{c} D \sin(2\pi\omega t), \tag{4.17}$$

and the instantaneous frequency of (4.17) gives the fringe frequency

$$f_F = 2\pi\omega \frac{f_0}{c} D. \tag{4.18}$$

The fringe frequency is dependent on the rotation rate of the radiometer as well as the antenna baseline, and the correlation radiometer has a variable rate of rotation as the system scans. Once f_F is determined the signal can be filtered to reject noise outside of the frequency band of interest.

Since the rotation rate is variable f_F can vary from a few hundred Hz to a few kHz and the baseband hardware must accommodate the range of frequencies. Thus determination of f_F is important to filter noise outside of the band of interest. To determine f_F in real-time, spectral estimation techniques are used. Pisarenko harmonic decomposition (PHD) [31, 32], Root MUSIC [31, 33], and a least-squares ESPRIT [31, 34] were compared to (4.18) using four sets of data[†]. The algorithms are run prior to any filtering, thus there are a total of three complex sinusoids present in the correlation signal; two resulting from the cosine in (4.16) centered at $\pm f_F$ and one at DC. The signal of interest is the $+f_F$ sinusoid. The time-window length for the PHD algorithm is M = 4 (one greater than the number of signals), while for the Root MUSIC and ESPRIT algorithms a time-window length of M = 10 was chosen. Using M > 10 for MUSIC and ESPRIT did not result in a significant improvement in estimating f_F and increased the processing time. The results of the experimental comparison are shown in Table 4.2 and demonstrate that the Root MUSIC and ESPRIT algorithms performed comparably while the PHD algorithm showed the greatest error. Due to its computational simplicity the ESPRIT algorithm was chosen over MUSIC.

Table 4.2. Spectral estimation of the fringe frequency

Fringe Frequency	97 Hz	126 Hz	171 Hz
Number of tests	32	41	57
Average Estimation error (Hz)			
PHD	110.2	16.1	6.1
Root MUSIC	3.8	3.2	0.3
ESPRIT LS	5.7	5.0	0.5

[†] The derivations of the PHD, MUSIC, and ESPRIT algorithms are covered in Appendix B.

4.4.4 Projected Baseline

The response of the correlation radiometer is a measure of the coherence of the electric field at the two antennas. In general the coherence at two points can be measured by the mutual coherence function, defined by [15]

$$\Gamma(\mathbf{x}_1, \mathbf{x}_2) = \lim_{T \to \infty} \frac{1}{2T} \int_{-T}^{T} E(\mathbf{x}_1, t) E^*(\mathbf{x}_2, t) dt$$
$$= \left\langle E(\mathbf{x}_1, t) E^*(\mathbf{x}_2, t) \right\rangle. \tag{4.19}$$

The electric field is given by

$$E = E_0 \exp\left[-j2\pi f \left(\mathbf{x}_{1,2} \cdot \mathbf{s}_{1,2} / c - t\right)\right], \tag{D.20}$$

where $\mathbf{x}_i$ is the location of the antenna and $\mathbf{s}_i$ is the vector from the antenna to the point of interest on the source. The baseline is then given by $\mathbf{D} = \mathbf{x}_1 - \mathbf{x}_2$ and $\boldsymbol{\sigma} = \mathbf{s}_1 - \mathbf{s}_2$. The total coherence function is integrated over the source giving [15]

$$\Gamma(\mathbf{D}) = \iint_{4\pi} I(\boldsymbol{\sigma}) \exp\left(-j2\pi f \mathbf{D} \cdot \boldsymbol{\sigma}\right) d\Omega. \tag{4.21}$$

The mutual coherence function given by (4.21) is similar to the visibility given by (3.18) except that the visibility is modified by the antenna pattern. In radio astronomy and remote sensing applications, the inverted visibility is divided by the antenna pattern to recover the radiance.

For a total power receiver the baseline $|\mathbf{D}| = 0$ and (4.21) reduces to $\Gamma(\mathbf{D}) = I(\boldsymbol{\sigma})$. For the correlation receiver $\Gamma(\mathbf{D}) \leq I(\boldsymbol{\sigma})$ depending on the level of coherence of the

49

incoming waves. In human presence detection in cluttered environments the coherence depends on the type of object being viewed and whether it is self-luminous or reflecting. A self-luminous object, such as a human, will produce radiation that tends to be highly correlated between the antennas. Radiation from an object which reflects and scatters radiation from other environmental sources will contain a number of random signals and will tend to have low correlation between the antennas.

Because of the narrow beamwidth of the antennas, and because the antennas on the correlation radiometer are stationary and do not track a source as in radio astronomy, the projected baseline D_p, which is the baseline as seen from the source, remains approximately stationary as a source passes through the beams. This is in contrast to radio astronomy applications which use the rotation of the Earth to alter the projected baseline as the source is tracked [14]. The beamwidth on each antenna is 0.0663 radians, thus for a point source the recorded response results from the projection of the baseline changing over 0.0332 radians on either side of the source. The projected baseline at the edges of this region is then

$$\mathbf{D}_{p,edge} = \sin\left(\frac{\pi}{2} \pm 0.0332\right)\mathbf{D} = 0.9995\,\mathbf{D}. \tag{4.22}$$

The maximum baseline used on the correlation radiometer is approximately 70λ, resulting in a negligible change in the projected baseline over the beamwidth. With only a single baseline the spatial transfer function of the interferometer, which indicates which spatial points are sampled in the source plane, is a point source or delta function in terms of the baseline [35]. If multiple antennas were used, the transfer function would be a sum of delta-functions at each of the available baselines. The visibility given by (3.18), sometimes referred to as the measured visibility, is the multiplication of the spatial

transfer function and the actual visibility. Thus (3.18) is approximately constant at each sampled point of the response.

4.4.5 Phase Analysis and the Far-Field Approximation[†]

When the radiating source is not significantly far from the correlation radiometer the vectors from the source to each antenna are no longer parallel. With a uniformly radiating source the difference between this setup and that with parallel radiating vectors is the geometrical time delay. The general geometrical diagram with non-parallel radiation vectors is shown in Figure 4.10.
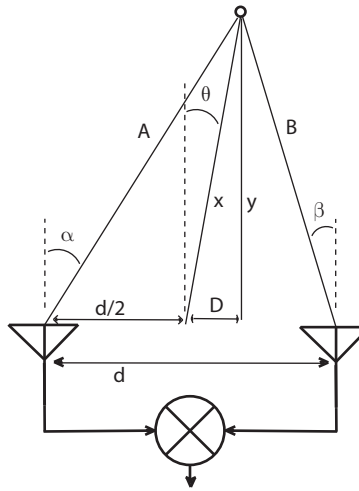
Figure 4.10. Geometry of non-parallel radiation setup.

The geometrical time delay for parallel radiation is defined as

$$\tau_{g,p} = (d/c)\sin\theta. \tag{4.23}$$

[†] For completeness of this dissertation, this section is reproduced from [36]   J. A. Nanzer, "A K_a-Band Correlation Radiometer for Human Presence Detection from a Moving Platform," M.S. Thesis, The University of Texas at Austin, 2005.

The geometrical time delay for the non-parallel case is the difference in length between the two distances A and B, the distances between the source and each antenna, divided by the speed of light:

$$\tau_{g,n} = \frac{1}{c}(A-B). \tag{4.24}$$

The length d is known and the angle θ is the variable. This information alone is not enough to define the response and thus the distance to the radiating source x is also assumed to be known and will be defined in test cases to show how changing the distance to the source affects the time delay compared to the parallel case. Thus the distances A and B must be found in terms of d, θ and x From the diagram, these distances can be defined as

$$\begin{aligned} A &= \frac{y}{\cos\alpha}, \\ B &= \frac{y}{\cos\beta}. \end{aligned} \tag{4.25}$$

The time delay is then given by

$$\tau_{g,n} = \frac{1}{c}(A-B) = \frac{y}{c}\left(\frac{1}{\cos\alpha} - \frac{1}{\cos\beta}\right) = \frac{y}{c}\left(\frac{\cos\beta - \cos\alpha}{\cos\alpha\cos\beta}\right). \tag{4.26}$$

The length y can be used to find the angles α and β by

$$y = A\cos\alpha = B\cos\beta, \tag{4.27}$$

52

$$\alpha = \cos^{-1}\left(\frac{y}{A}\right), \tag{4.28}$$

$$\beta = \cos^{-1}\left(\frac{y}{B}\right). \tag{4.29}$$

The lengths D and y can be given by

$$D = y \tan\theta, \tag{4.30}$$
$$y = x \cos\theta. \tag{4.31}$$

Distance A can be found in terms of these lengths by

$$A = \sqrt{y^2 + \left(d/2 + D\right)^2} = \sqrt{x^2 \cos^2\theta + \left(d/2 + x\cos\theta\tan\theta\right)^2}. \tag{4.32}$$

Distance B is found similarly except that the length $d/2+D$ becomes $d/2-D$:

$$B = \sqrt{x^2 \cos^2\theta + \left(d/2 - x\cos\theta\tan\theta\right)^2}. \tag{4.33}$$

Equations (4.32) and (4.33) can then be substituted into equations (4.28) and (4.29) to find the angles α and β; these along with (4.31) can then be substituted into (4.26) yielding

$$\tau_{g,n} = \frac{x\cos\theta}{c}\left(\frac{\cos\beta - \cos\alpha}{\cos\alpha\cos\beta}\right), \tag{4.34}$$

with the angles and distances defined by (4.28), (4.29), (4.31), (4.32) and (4.33).

When $\theta = \pm\pi/2$ the angles α and β become equal and (4.34) becomes zero; this corresponds to radiation incident 90° to boresight on the antennas. For a real antenna this would be of no concern since it would not pick up radiation that was incident directly sideways. Theoretically however equation (4.34) should be amended as follows:

$$\tau_{g,n} = \begin{cases} \dfrac{x\cos\theta}{c}\left(\dfrac{\cos\beta - \cos\alpha}{\cos\alpha\cos\beta}\right), & \theta \neq \dfrac{\pi}{2} \\[2em] \dfrac{x}{c}, & \theta = \dfrac{\pi}{2} \end{cases}$$

(4.35)

recalling that $\theta = \pi/2 \rightarrow \alpha = \beta$.

The difference between (4.23) and (4.35) depends on y the distance to the radiating source. Figure 4.11 shows the delays graphed over one half-cycle for four different distances. The difference between $\tau_{g,n}$ and τ_p becomes negligible beyond even a few feet from the antennas: With $x = 15.7$ ft and a range of 4 ft to the radiation source, the average time difference $|\tau_p - \tau_{g,n}| = 7.5$ ps over the hemisphere. However the antenna half power beamwidth is 3.876° in azimuth and in this range the time difference is 0.589 ps which at 27.4 GHz translates to a phase delay of merely 0.92° compared to the assumption of parallel radiation vectors. The inner range of the radiometer is about 4 ft and a phase delay of less than 1° is acceptable, thus $\tau_{g,n} \approx \tau_p$.

Figure 4.12 shows the fringe patterns resulting from a radiating source at 15.7 ft and parallel radiation (15.7 ft is the distance where the center of the angled antenna beams cross in this configuration). The average difference in amplitude between the two fringe patterns is 0.0019 V where the patterns have been normalized to 1 V; this difference is negligible. Thus if the radiating source is greater than 5 ft from the radiometer the difference between the theoretical result assuming non-parallel radiation incidence and that assuming parallel incidence is negligible.

54
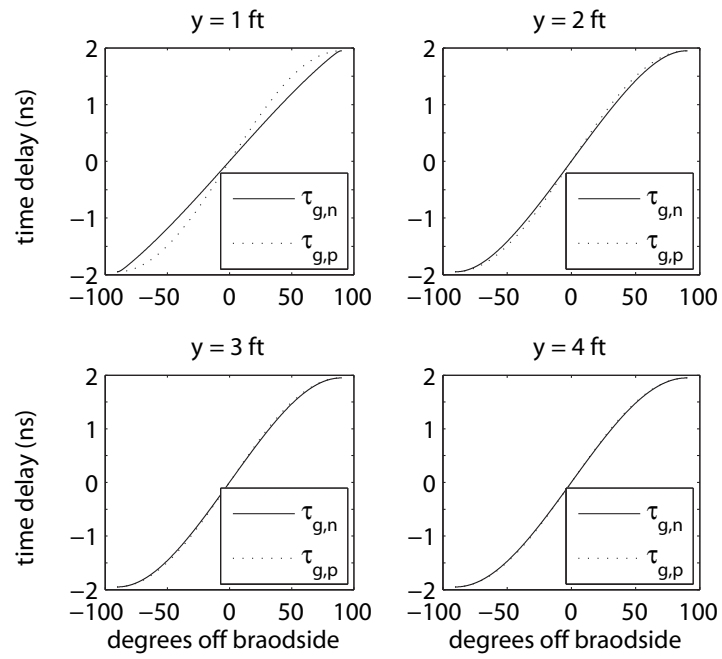
Figure 4.11. Time delays over one half-cycle for distance of 1 to 4 ft for non-parallel radiation $\tau_{g,n}$ and parallel radiation τ_p.
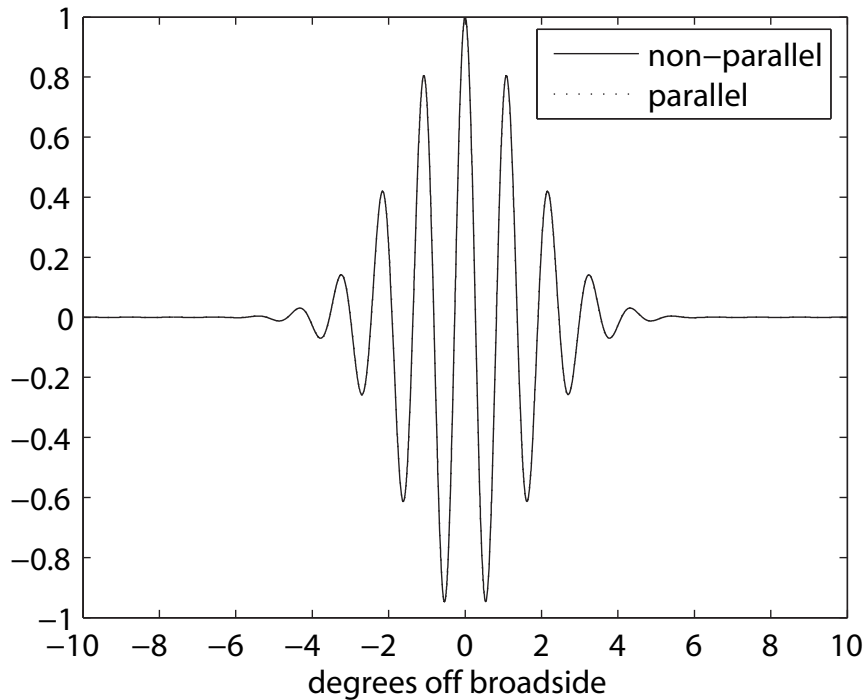
Figure 4.12. Calculated fringe patterns resulting from non-parallel radiation from a source at 15.7 ft and parallel radiation incidence.

4.4.6 Spatial Resolution and Dwell Time

The antenna beams of the correlation radiometer are not always parallel [37]. Angling the antennas changes the spatial resolution depending on the range and antenna angle. It is important to accurately know the spatial resolution because the dwell time of the radiometer directly depends on it, and to ensure good radiometric resolution the dwell time must be longer than the integration time of the correlator [16].

The dwell time for a single antenna beam is given by

$$\tau_d = \beta/\omega. \tag{4.36}$$

In terms of the spatial resolution Δx and the range R the dwell time can be written

$$\tau_d = \Delta x/R\omega. \tag{4.37}$$

For close range detection with a two-element correlation radiometer there are generally three different cases specifying the spatial resolution depending on the antenna angle α, the beamwidth β, and the range r_1 where the centers of the antenna beams converge: no convergence (Figure 4.13(a)), where the beams cross at infinity; partial convergence (Figure 4.13(b)), where the beam centers converge but the beams do not diverge within β; and total convergence (Figure 4.13(c)), where the beam centers converge and the beams diverge at a finite distance. The expressions for the ranges where the 3dB beamwidths converge (r_c) and diverge (r_d) are given by

$$r_{c,d} = \frac{D}{2}\tan\left(\frac{\pi}{2} - \alpha \mp \frac{\beta}{2}\right). \tag{4.38}$$

The spatial resolution is given by the following equations for each case:

1. $\alpha = 0$ (no convergence)

$$\Delta x_{cr} = \begin{cases} (R - r_c)\beta, & R \geq r_c \\ 0, & R < r_c \end{cases}$$

(4.39)

2. $0 < \alpha \leq \beta/2$ (partial convergence)

$$\Delta x_{cr} = \begin{cases} (R - r_c)(2\alpha + \beta), & r_c \leq R < r_1 \\ 2b\sin(\alpha + \beta/2), & R = r_1 \\ D - 2R(\alpha - \beta/2), & R > r_1 \\ 0, & R < r_c \end{cases}$$

(4.40)

where $r_1 = r_c + b(\alpha + \beta/2)$ and

$$b = \frac{\sin \beta}{\sin 2\alpha} \sqrt{r_c^2 + D^2/4}.$$

(4.41)

3. $\alpha > \beta/2$ (total convergence)

$$\Delta x_{cr} = \begin{cases} (R - r_c)(2\alpha + \beta), & r_c \leq R < r_1 \\ r_1(2\alpha - \beta), & R = r_1 \\ (r_d - R)(2\alpha - \beta), & r_1 < R \leq r_d \\ 0, & r_d < R \text{ or } R < r_c \end{cases}$$

(4.42)

where $r_1 = D/2\alpha$.
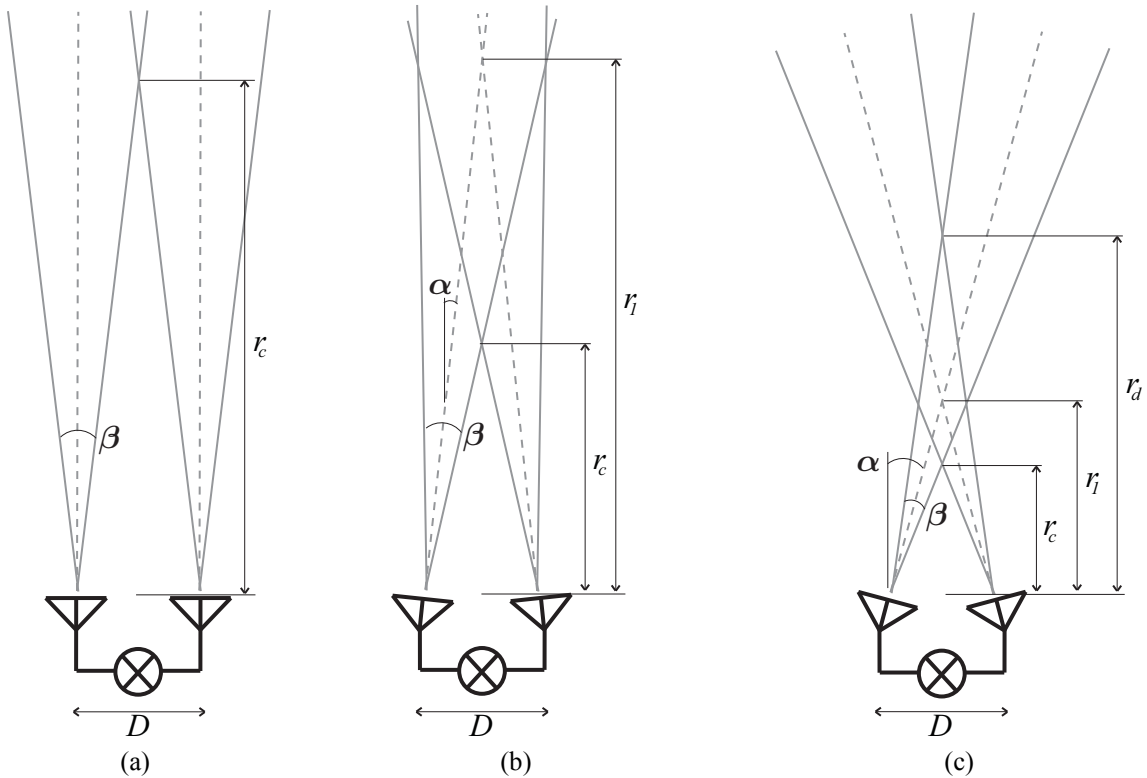
Figure 4.13. Diagrams of three cases of antenna coverage for the calculation of spatial resolution. (a) No convergence, (b) partial convergence, and (c) total convergence.

The dwell time for the correlation radiometer is then

$$\tau_d = \Delta x_{cr}/R\omega. \tag{4.43}$$

The spatial resolution of the correlation radiometer is shown in Figure 4.14(a) for a baseline $D = 16$ cm and $\beta = 3.8°$. When $\alpha = \beta/2 = 1.9°$ the spatial resolution remains constant in R beyond r_c; this is the boundary between partial convergence and total convergence. The dwell time, being proportional to R^{-1}, does not remain constant over range (Figure 4.14(b)).
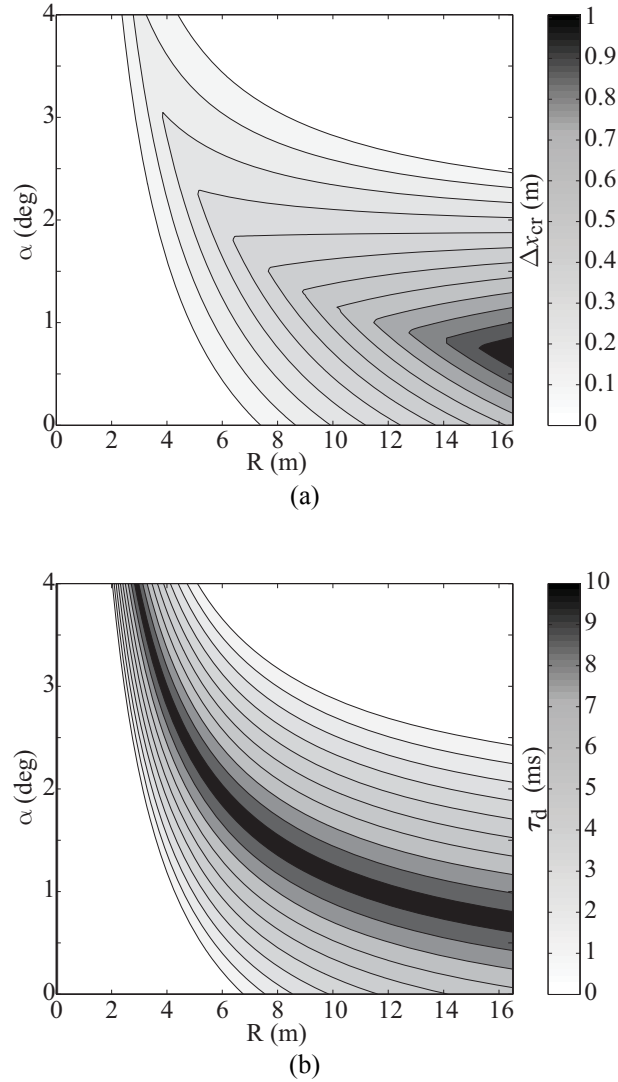
Figure 4.14. (a). Spatial resolution. (b). Dwell time.

If the integration time τ of the radiometer is much greater than τ_d it will take the radiometer longer than τ_d to register a change in the observed scene. This effectively makes the radiometric spatial resolution larger than the antenna spatial resolution Δx_{cr}. Thus, given the dwell time in (4.43) the integration time of the system can be set to keep the spatial resolution reasonably close to Δx_{cr}. On the correlation radiometer τ is set by the 2 kHz LPF at 0.5 ms, which is lower than τ_d in all relevant cases. Only when $\alpha > 2°$

does the integration time become an issue at large values of R; however, the maximum α used for the correlation radiometer is 1.5°.

Chapter 5: Target Detection and Classification

5.1 OBJECTIVE

The voltage signals from the correlation mode given by (3.28) and the three total power detection modes (two K_a-band and one W-band) given by (3.8) must be analyzed in conjunction with the shaft encoder signal to determine target classification on a rotation-to-rotation basis. The signals must be filtered and conditioned properly in order to pass to the classification algorithms. This section describes the processes used to condition the signals prior to classification and describes the methods of signal classification that were used. Some experimental results are discussed, although the experimental evaluation of the classifiers is presented in the following chapter.

5.2 PRE-CLASSIFICATION SIGNAL PROCESSING

The sensor suite contains the K_a-band radiometer sensor, the W-band total power radiometer, a shaft encoder for angle data, and a laser range finder for the determination of range. The range estimated using only the K_a-band total power radiometers in order to focus solely on the PMMW system; however the passive range estimation is relatively inaccurate as will be shown, and the active ranging laser range finder is used to corroborate the passive estimate. Using the shaft encoder data the signals are divided into arrays for each rotation to facilitate real-time processing. Thus, upon completion of a full 360˚ rotation the signal arrays are conditioned and analyzed.

(a)

(caption on following page)

(b)

(caption on following page)

62

(c)
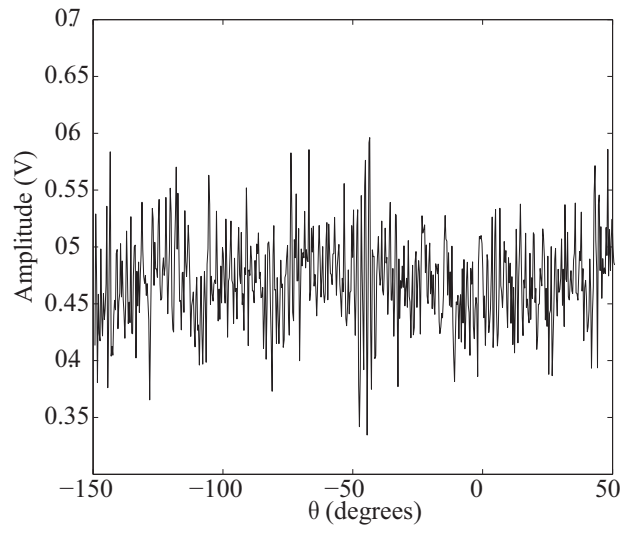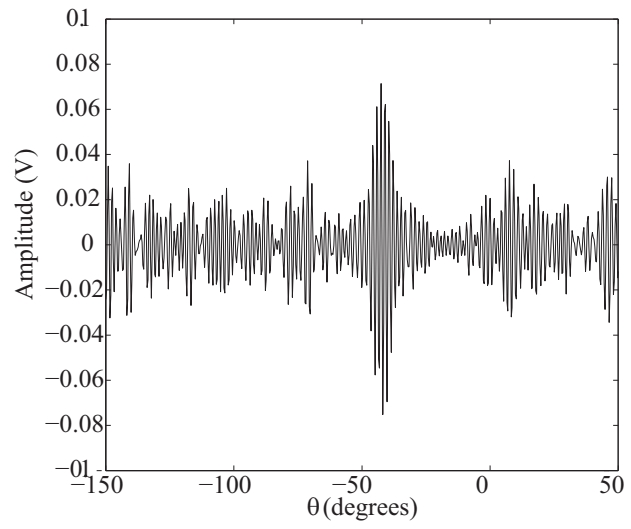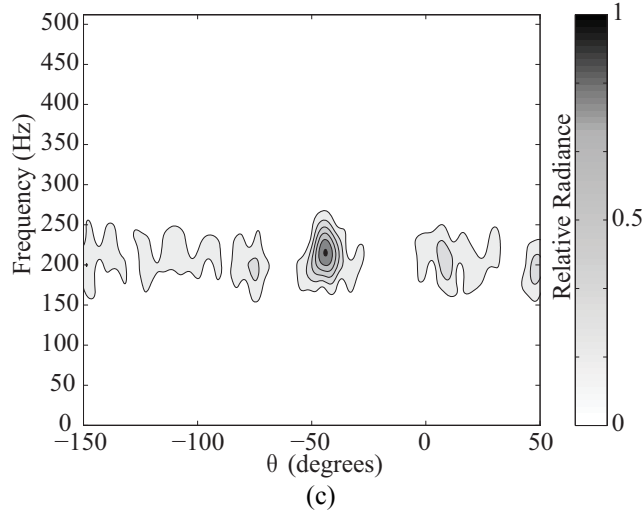
Figure 5.1. Steps in the processing of the correlation signal. The response to a human is present at -45°. (a) Raw time-domain signal. (b) Time-domain signal filtered around f_F. (c) Spectral correlation signal in the time-frequency domain.

The fringe frequency f_F is estimated each rotation using ESPRIT. The correlation signal is then band-pass filtered around f_F with a bandwidth equal to the spectral 3dB width of a simulated point source response. Following this the signal is processed by short-time Fourier transform (STFT) resulting in the *spectral correlation* signal, which is proportional to the radiance. If calibrated to absolute temperature, the spectral radiance is equal to the observed brightness. The profile of the spectral radiance is taken along f_F, resulting in a time-dependent voltage signal consisting of peaks and nulls which is similar in appearance to the total power signals. Figure 5.1 shows the raw correlation signal, the signal filtered around f_F, and the spectral correlation signal resulting from the STFT.

5.2.1 Median Filtering

The width of a peak in the total power or spectral correlation signals that is due to a human is dependent mostly on the distance of the person. For this dissertation I am only

63

concerned with detecting a standing human; detection of a person in other positions would be carried out by creating training data sets and setting the classification thresholds accordingly. The peak width is dependent somewhat on the position of the standing person; whether the sensor views the side or front of a person. However, the dependence on position of the person is dwarfed by the dependence on distance thus it is not included in the analysis.

The median filter is a nonlinear smoothing filter which consists of a running median of a given length. The median filter is nonlinear because it does not obey the superposition property [38]:

$$\text{median}\left[ax_1(n)+bx_2(n)\right] \neq a\,\text{median}\left[x_1(n)\right]+b\,\text{median}\left[x_2(n)\right].$$ (5.1)

Consider the total power or spectral correlation signal as a combination of a slowly varying signal due to the background and a rapidly varying signal due to human detections;

$$x(n) = s(n)+r(n),$$ (5.2)

where $s(n)$ is the slowly varying background signal and $r(n)$ is the rapidly varying signal due to the human. A median filter of median length m has the effect of eliminating sharp discontinuities of length $l \leq m$ [38]. Thus, given the width of a peak resulting from a human at a distance r, all such peaks will be eliminated from the signal, leaving the smoothed signal

$$y(n) \approx s(n).$$ (5.3)

The desired signal is composed only of the rapidly varying signals to be classified. This signal can be obtained by subtracting (5.3) from (5.2), giving

$$z(n) = x(n) - y(n) \approx r(n). \tag{5.4}$$

Figure 5.2 shows a block diagram of the median filtering process and examples of the median filtering process are shown in Figure 5.3. The first plot shows $x(n)$ from a total power scan over one rotation. The following plots show the median filtered signal and the difference of the two. The final signal is contained of peaks whose width is equal to or less than that of a human at a given distance and this signals allows the filtering of the raw data into range bins. The data is then analyzed based on the peak widths for its appropriate range bin.
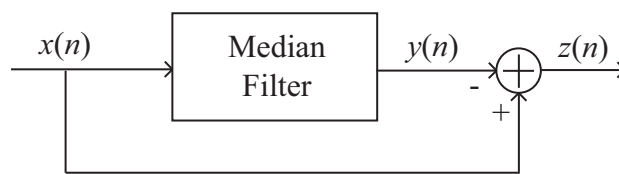
Figure 5.2. Block diagram of the median filtering process.
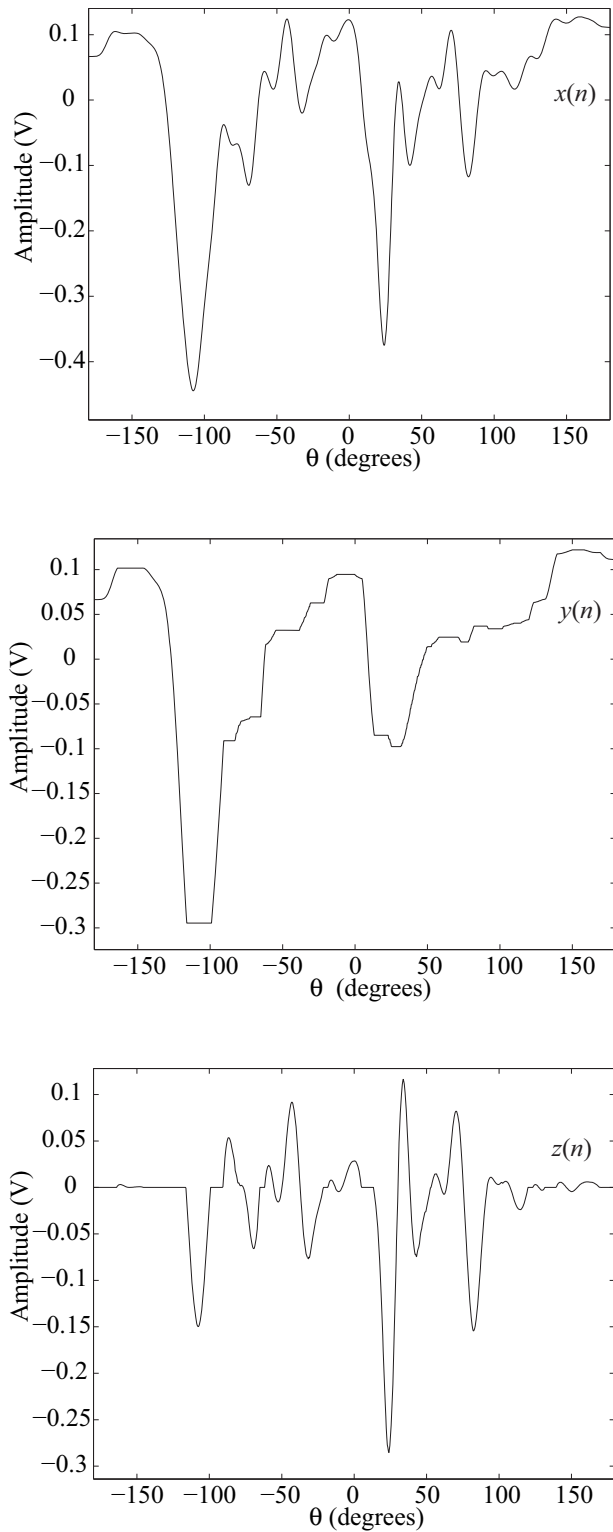
Figure 5.3. Example of the median filtering process.

66

Table 5.1. Detection range divisions

	Region 1	Region 2	Region 3	Region 4
Range (ft)	0-10	10-25	25-35	35-45

Region 4

Region 3

Region 2

Region 1

Robot and
Radiometer
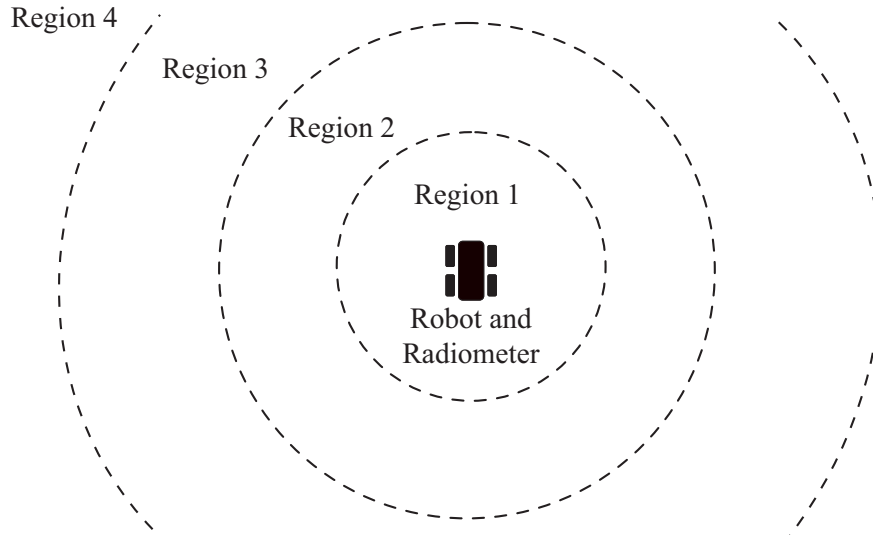
Figure 5.4. Diagram showing the range divisions for the median filtering process.

The peak width used to detect humans is calculated based on four divisions in the effective range of the sensors which are given in Table 5.1. Four filtered signals are calculated from each input signal (total power or correlation), each filtered signal specific to one region. Figure 5.4 shows a diagram (not to scale) of the range regions.

5.2.2 Range Estimation

Range is determined in two different methods, one using a simple triangulation laser range finder, the second using the intrinsic properties of the angled beams of the K_a-band total power modes to estimate the range passively. Once the range is determined an

x-y map of the area scanned can be produced. Without the range determination the detection method would not work as a mobile system.

Passive Range Estimation

The range is estimated by measuring the time difference between peaks in the total power signals. Knowing the angles of the antenna beams, once a peak is detected in the first beam the time until the same peak appears in the second beam can determine the range. The method also works beyond the convergence point of the beams by measuring the time between the peak appearing on the second beam before the first.
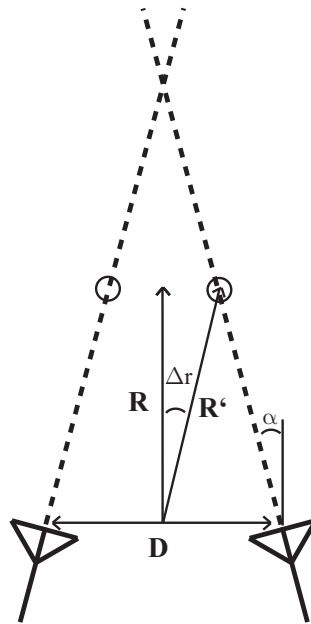
Figure 5.5. Geometry describing the passive range estimation. The circles indicate where the person crosses the antenna beams, R is the range vector to the person.

The geometry in Figure 5.5 shows how the passive range estimation is calculated. The range to the person R is found based on the antenna angle α and the separation between the peak $2\Delta r$, which is measure in radians. From the law of sines,

$$\frac{R'}{\sin(\pi/2-\alpha)} = \frac{D/2}{\sin(\Delta r+\alpha)},$$ (5.5)

or

$$R' = \frac{D}{2} \cdot \frac{\sin(\pi/2-\alpha)}{\sin(\Delta r+\alpha)}.$$ (5.6)

Since $R = R'\cos(\Delta r)$,

$$R = \frac{D}{2}\cos(\Delta r)\frac{\sin(\pi/2-\alpha)}{\sin(\Delta r+\alpha)}.$$ (5.7)

The distance Δr can be found by the equation

$$\Delta r = 2\pi \cdot \frac{1}{2}\frac{N}{F},$$ (5.8)

where N is the number of data points between the two peaks and F is the number of points in the full rotation.

The preponderance of peaks present in the total power channels caused an over-prediction of objects estimated by the passive ranging, as seen in Figures 5.6 and 5.7. In Figure 5.6 (a)-(c) a person is present at (10ft, 25ft), (14ft, 25ft), and (18ft, 25ft) respectively, and there is clutter present on the left of the graph. The colors indicate the number of times an object is detected at each pixel: grey pixels indicate one range detection and black pixels indicate two detections. In the actual setting there are fewer objects than detected by the passive range estimation. However, the passive range tends

to cluster range detections at the correct locations. In Figures 5.6 (a)-(c) the clutter present on the black pixels on the left of the graph were present in the actual setting, as were objects where the grey pixels tend to cluster. Lines can be seen on the bottom left of the graph which are comprised of grey pixels and correctly, although somewhat inaccurately, represent actual objects. The center line of range detections in the figures indicate the location of the platform as it traverses the track and does not indicate an object. Figures 5.7 (a)-(c) shows three passive range maps with a person located at (10ft, 25ft), (14ft, 25ft), and (18ft, 25ft) respectively in a less cluttered environment. The range still tends to clutter in the area where the person is located.
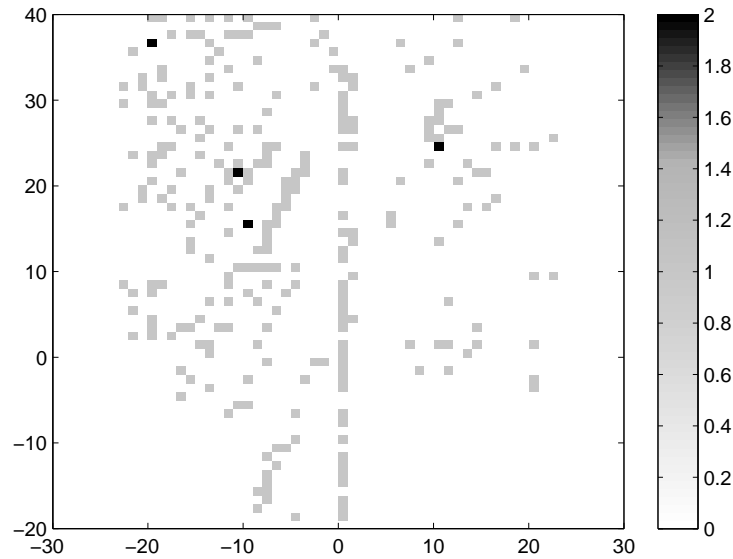
(a)
(caption on following page)
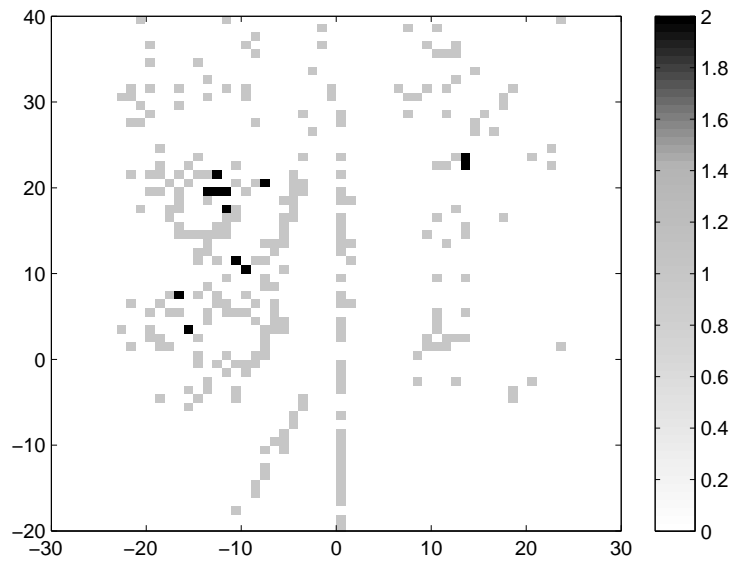
(b)
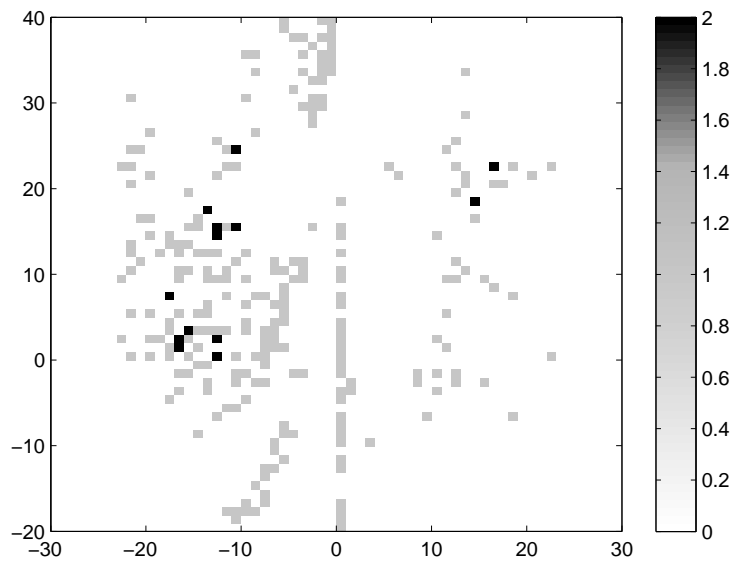
(c)

Figure 5.6. Passive range maps from one setting with a person present at (a) (10ft, 25ft), (b) (14ft, 25ft), and (c) (18ft, 25ft). There are objects present on the left side of the graph where the pixels tend to cluster. The center line indicates the location of the moving platform as it moves forward.

(a)
(caption on following page)
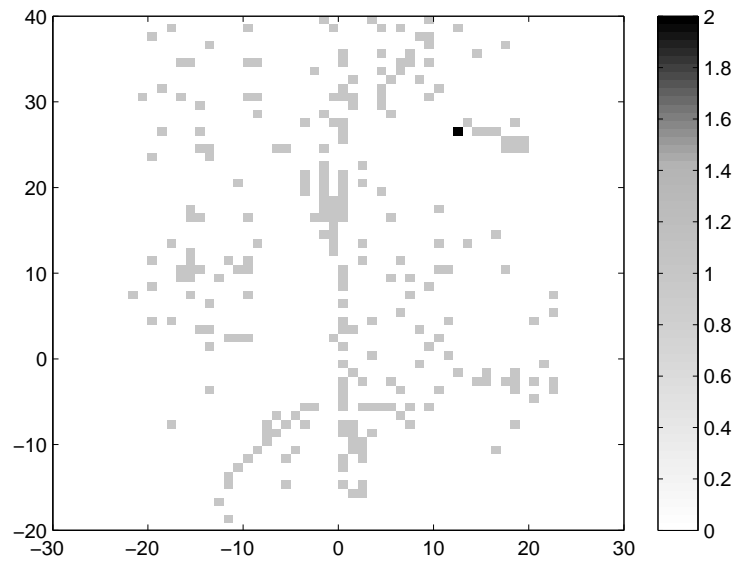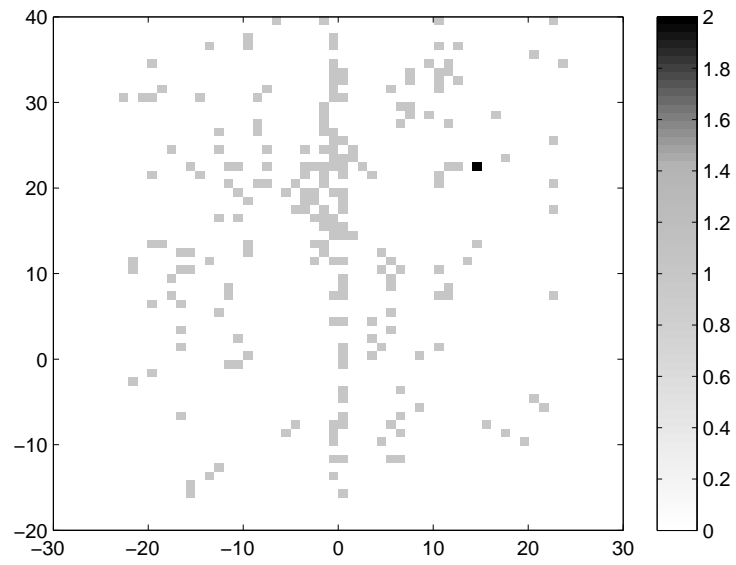
(b)
(caption on following page)
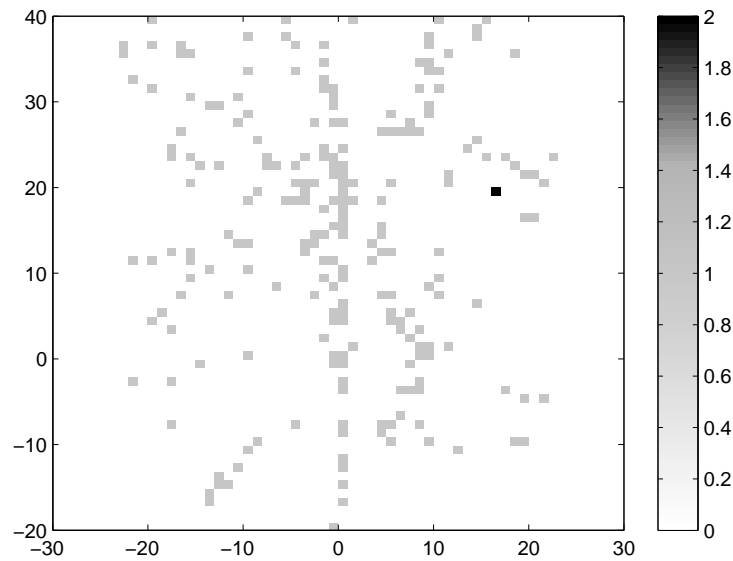
(c)

Figure 5.7. Passive range maps from a second, less cluttered setting with a person present at (a) (10ft, 25ft), (b) (14ft, 25ft), and (c) (18ft, 25ft).

The over-estimation of objects indicates the inaccuracy of the passive range method, however the tendency of the estimation to cluster range detections in the area of actual detections indicates that the estimation of range to objects is approximately correct in these areas. In the following sections I will discuss that the probability of detection in the areas where there are fewer passive range detections tends to be lower since there are no peaks present in these areas. Thus when implementing the final x-y map with the range, only the areas of greater probability tend to be present. To improve the accuracy of the passive range estimation a linear regression estimator could be implemented using the active range as the data to approximate.

Active Range

In its current implementation the passive range estimate is not accurate enough on its own. As a backup measure a triangulation laser range finder is attached to the platform to provide a more accurate range measurement.

Range determination does not enter into the classification algorithms. The range is only used to create the *x-y* detection map in the final steps. Thus the detection and classification algorithms are only dependent on the millimeter-wave sensors, thus making the detection method presented here independent of any active sensors.

5.3 TARGET CLASSIFICATION

5.3.1 Heuristic classification

Target classification was initially accomplished using a heuristic formulation. In this classification method the total power signals are filtered to remove slowly-varying background variations, resulting in a series of peaks and troughs in the voltage signal. Analyzing one total power channel, each peak is measured for width and height then compared to temporally close peaks on the other total power channel. When two peaks are temporally close, the difference in width and height are calculated. The same process is done using the derivative of each signal. If the differences in peak width, height, and location are under certain heuristic thresholds a *peak window* is defined around the data points. This process is referred to as *peak correlation* in the following discussion and for two signals tp_1 and tp_2 is denoted by $PC(tp_1, tp_2)$. Within this window the spectral correlation power is used to determine whether a detection is present. Figure 5.8 shows the peak window $PC(K_{a,1}, K_{a,2})$ formed around a detection at 118.05 s. The peak windows formed are as follows: $PC(K_{a,1}, K_{a,2})$, $PC(K_{a,1}, W)$, $PC(K_{a,2}, W)$, $PC(K_{a,1}, K_{a,1})$, $PC(K_{a,2},$

$K_{a,2}$), $PC(W, W)$, and $PC(K_{a,1}, K_{a,2}, W)$, where $K_{a,i}$ refers to the ith K_a-band total power channel and W refers to the W-band total power channel. Peak correlation pairs such as $PC(K_{a,1}, K_{a,1})$ are effectively the peak autocorrelation of the signal and serves to filter out any non-peaks in the data. Including the spectral correlation data, and the three raw total power signals (prior to data correlation) the heuristic formulation uses a total of eleven sensor signals (not including the laser range-finder or shaft angle encoder) to classify detections.
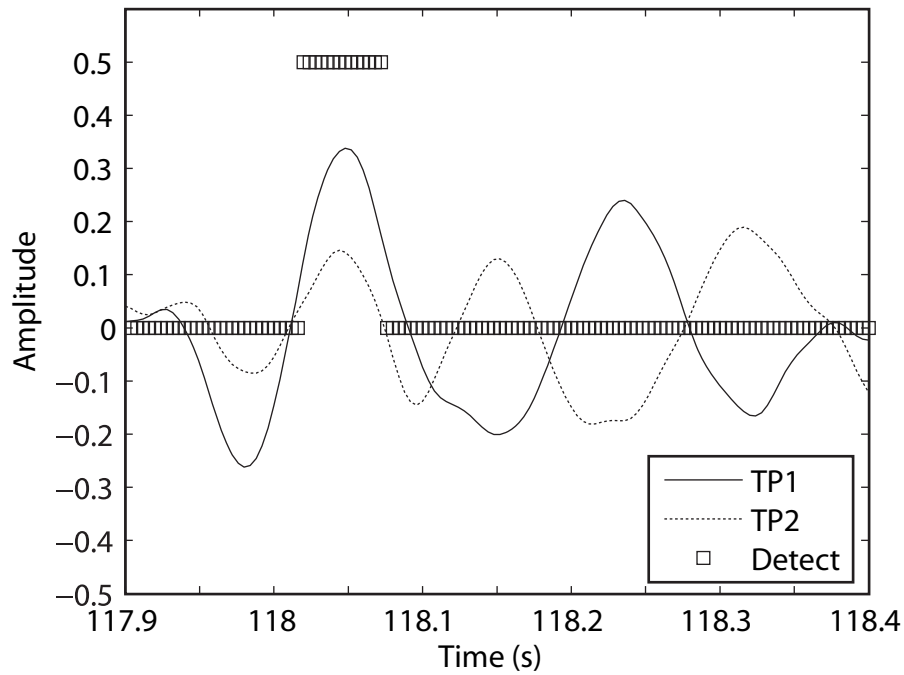
Figure 5.8. Peak correlation $PC(K_{a,1}, K_{a,2})$ resulting in a peak window centered at 118.05 sec.

The correlation signal is processed by short-time Fourier transform to convert the data into a quantity proportional to the scene brightness temperature. The experiment was run as is seen in Figure 5.9, with two people present in the data set on the left graph. Each rotation the maximum value of the STFT is taken at each data point and an array is created. Following this the arrays are plotted in versus the number of scans, producing a

75

scan map as seen in Figure 5.10, which shows the maximum spectral correlation data per angle. While one detection is noticeable, the other is not very noticeable. In addition, background objects cause strong signals on the right side of the graph. The peak window formed from the total power signals is then applied to the spectral correlation data by multiplying the peak window arrays per scan with each array of the spectral correlation signal. Applying the peak window has the effect of eliminating the false detections from the background objects seen on the right of Figure 5.10, as seen in Figure 5.11. The detections from the people are now very present while other responses are nearly eliminated.
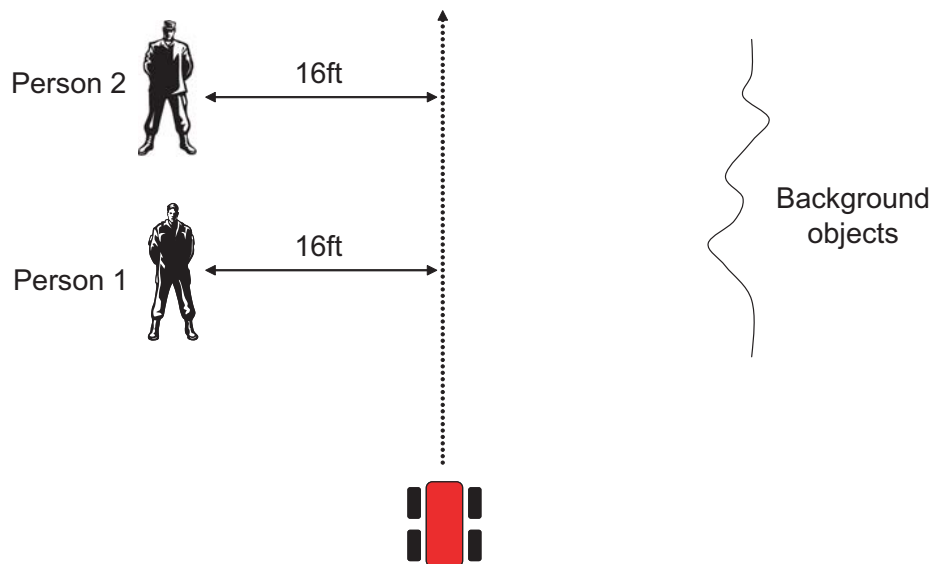
Figure 5.9. Experimental setup.
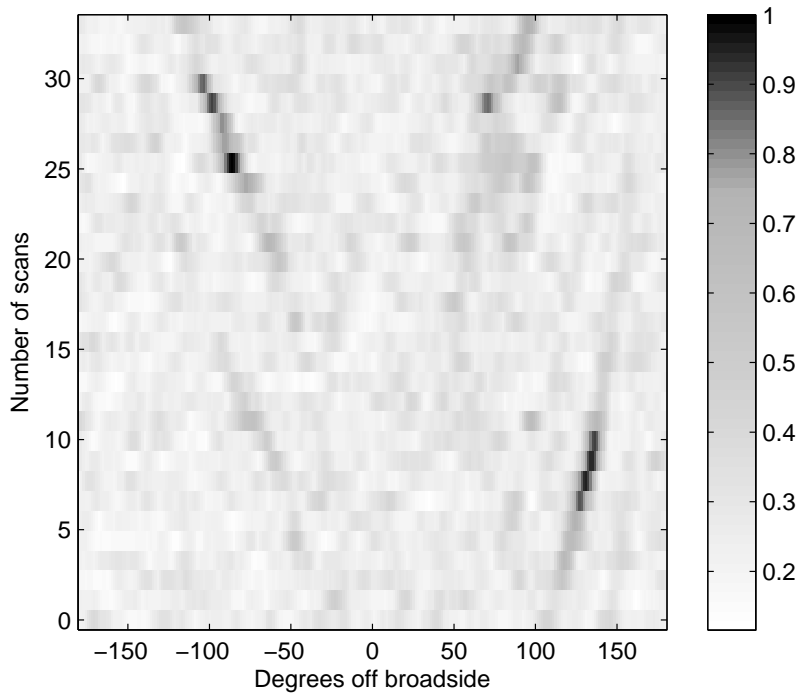
Figure 5.10. Scan map of spectral correlation data.
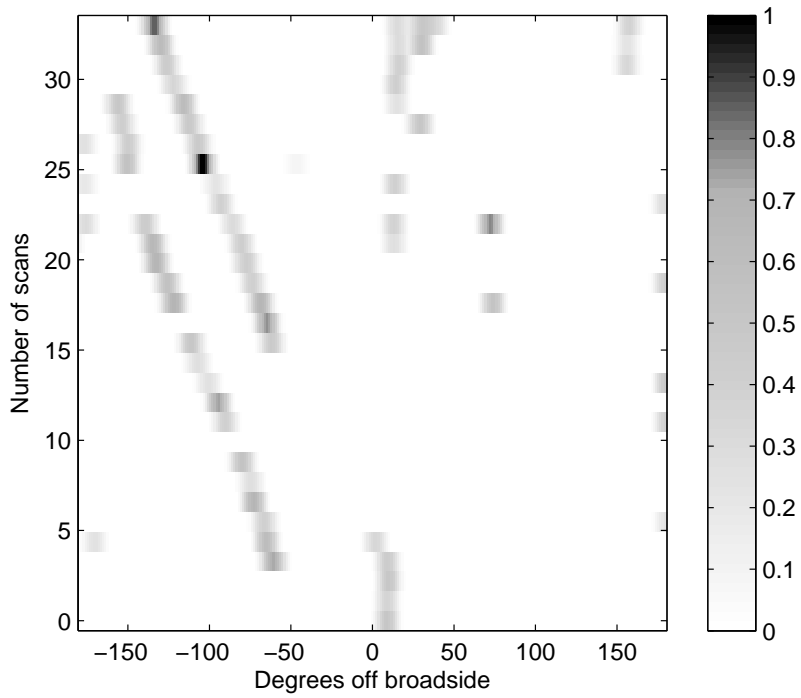
Figure 5.11. Scan map of spectral correlation data following the application of the peak window.

77

The detection map is formed by analyzing the output of a laser range finder and correlating the peak windows coinciding with the laser hits. Through each rotation vectors are formed of equal length containing total power, spectral correlation, laser range, and shaft angle data. The laser range vectors contains a series of points whose values are equal to the distance seen when the laser registers a detection on its CCD array. By incorporating the shaft angle encoder data an *x-y* grid of the area is formed. The vector data points coinciding with each laser hit are correlated with the vector points of the peak windowed arrays and each pixel on the *x-y* grid is summed with the value of each peak window at that pixel. Each rotation, pixels corresponding to laser range hits are summed with the value of the corresponding peak window. The result of applying this process to the map is shown in Figure 5.12; a human is standing at (15, 40) and it can be seen that there is a strong detection at this point.

This process works relatively well in most cases, however it is not without its drawbacks. The prominent detriment of the heuristic algorithms is processing overhead, running close to 400% slower than real-time, which clearly cannot be implemented in any kind of real-world security setting. Moreover, the heuristic approach lacks any fundamental statistical formulation in which a reasonable estimate of probabilities of detection and false alarm can be quantified. A formulation could be derived however it would be time consuming and would likely be specific only to this approach.
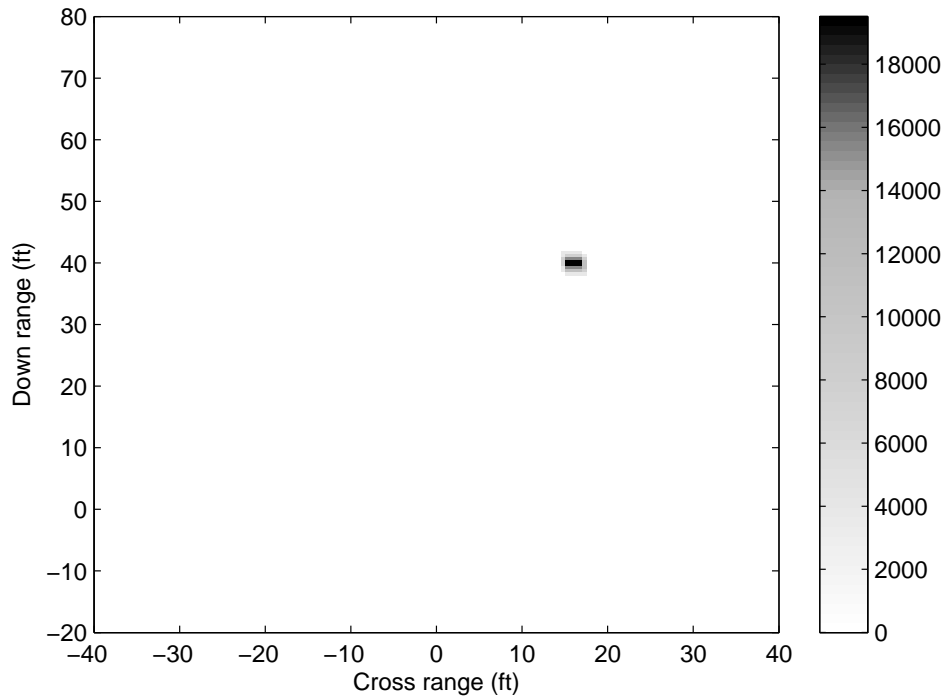
Figure 5.12. Heuristic detection map showing a detection at (15, 40).

5.3.2 Naïve Bayesian Classification

To improve the target classification results, a rudimentary Naïve Bayesian formulation was developed. This is a simple probabilistic classifier which depends on a number of inputs, or features, which are assumed to be independent. While it is typically not true that all the features are independent of each, other Naïve Bayesian classifiers typically produce better than expected results in real-world situations [39].

Given an array of features **x** the probability of a given data point being above the detection threshold (detection) is $p(D|\mathbf{x})$. Using Bayes' rule yields

$$p(D \mid \mathbf{x}) = \frac{p(\mathbf{x} \mid D)p(D)}{p(\mathbf{x})}, \tag{5.9}$$

79

and the probability of the point being below the threshold (no detection) is

$$p(N\,|\,\mathbf{x}) = \frac{p(\mathbf{x}\,|\,N)\,p(N)}{p(\mathbf{x})}. \tag{5.10}$$

Since $p(D\,|\,\mathbf{x}) + p(N\,|\,\mathbf{x}) = 1$,

$$p(D\,|\,\mathbf{x})\,p(D\,|\,\mathbf{x}) + p(D\,|\,\mathbf{x})\,p(N\,|\,\mathbf{x}) = p(D\,|\,\mathbf{x}), \tag{5.11}$$

$$p(D\,|\,\mathbf{x})\frac{p(\mathbf{x}\,|\,D)\,p(D)}{p(\mathbf{x})} + p(D\,|\,\mathbf{x})\frac{p(\mathbf{x}\,|\,N)\,p(N)}{p(\mathbf{x})} = \frac{p(\mathbf{x}\,|\,D)\,p(D)}{p(\mathbf{x})}, \tag{5.12}$$

$$p(D\,|\,\mathbf{x}) = \frac{p(\mathbf{x}\,|\,D)\,p(D)}{p(\mathbf{x}\,|\,D)\,p(D) + p(\mathbf{x}\,|\,N)\,p(N)}. \tag{5.13}$$

The features are the correlation signal given by (3.28) and the three total power signals given by (3.8), thus $\mathbf{x} = (cr, K_{a,1}, K_{a,2}, W)$. Under the feature independence assumption

$$p(\mathbf{x}\,|\,D) = p(x_1\,|\,D)\,p(x_2\,|\,D)\,p(x_3\,|\,D)\,p(x_4\,|\,D) = \prod_{i=1}^{4} p(x_i\,|\,D), \tag{5.14}$$

and thus it is determined that a detection has occurred if

$$p(D\,|\,\mathbf{x}) = \frac{p(D)\prod_{i=1}^{4} p(x_i\,|\,D)}{p(D)\prod_{i=1}^{4} p(x_i\,|\,D) + p(N)\prod_{i=1}^{4} p(x_i\,|\,N)} > 0.5. \tag{5.15}$$
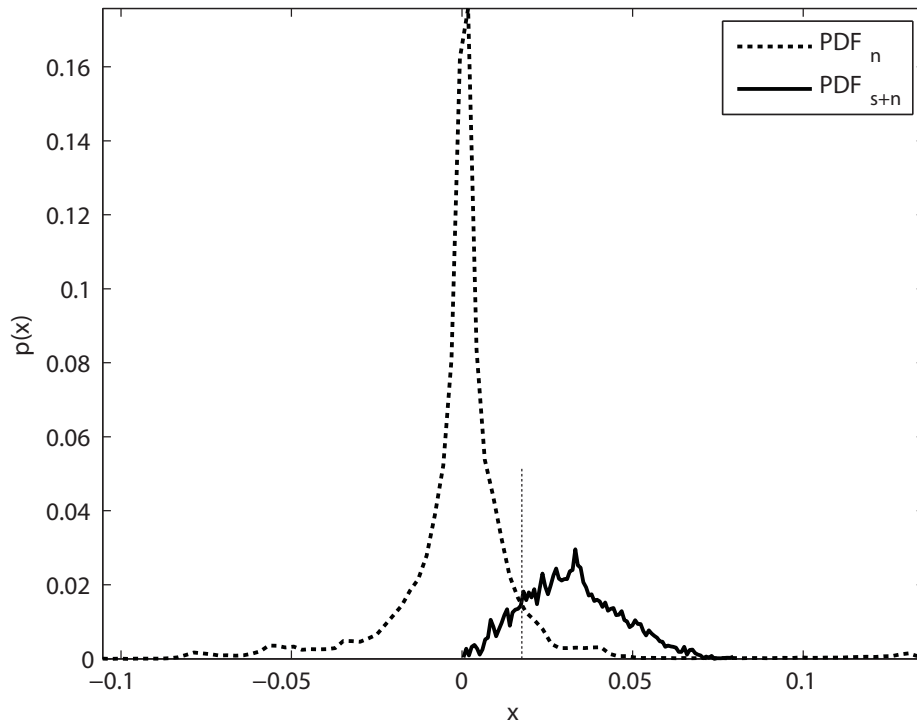
Figure 5.13. Probability densities for the total power 1 feature.
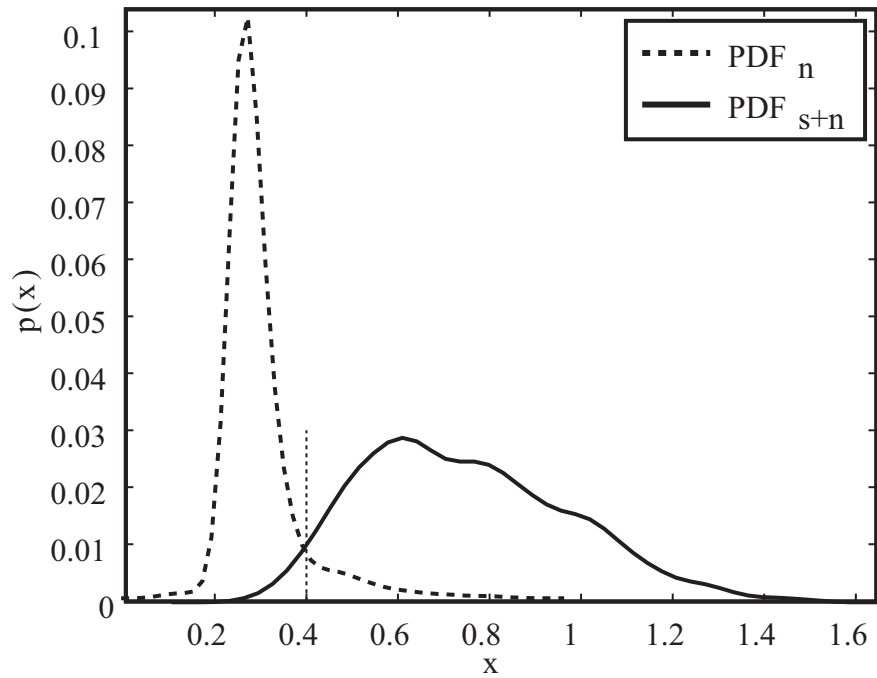
Figure 5.14. Probability densities for the correlation feature.

81

Table 5.2. Feature probabilities

Signal	Threshold
cr	40 mV
$K_{a,1}$	17.5 mV
$K_{a,2}$	17.5 mV
W	10 mV

Table 5.3. Feature probabilities

Signal	P_d	P_{fa}
cr	0.985	0.107
$K_{a,1}$	0.856	0.085
$K_{a,2}$	0.919	0.101
W	0.834	0.035

The prior probabilities $p(D)$ and $p(N) = 1 - p(D)$ cannot be accurately defined since they are highly dependent on the situation in which the system is being used. As such it is assumed that each outcome is equally likely to occur for the general case; that is, $p(D) = p(N) = 0.5$.

The feature probabilities were experimentally determined using only threshold detection as a factor; the probability densities from the noise and the signal plus the noise are seen in Figures 5.13 and 5.14 for the total power 1 and correlation signals, respectively. The voltage thresholds for each signal are shown in Table 5.2 and the resulting probabilities of detection and false alarm shown in Table 5.3.

Similar to the heuristic formulation, a vector is formed containing the probability of detection determined by (5.15) for each point in every rotation. Laser range data is correlated to these probabilities and an *x-y* map is formed. Each rotation, pixels corresponding to laser range hits have added to their values the probability determined by (5.15), as seen in Figure 5.15.

The detection map resulting from the rudimentary Naïve Bayesian classifier is clearly comparable to the heuristic formulation depicted in Figure 5.12. In addition, the processing time of this implementation of the Naïve Bayesian classifier runs on average at nearly 15% faster than the experimental time, which is an improvement over the heuristic formulation and can be applied to real-world situations. Another benefit of the Bayesian approach that has been seen in experimental outcomes is improved range; the heuristic approach was limited by a maximum range of about 25 *ft* whereas the current Bayesian formulation detects out to approximately 35 *ft*.
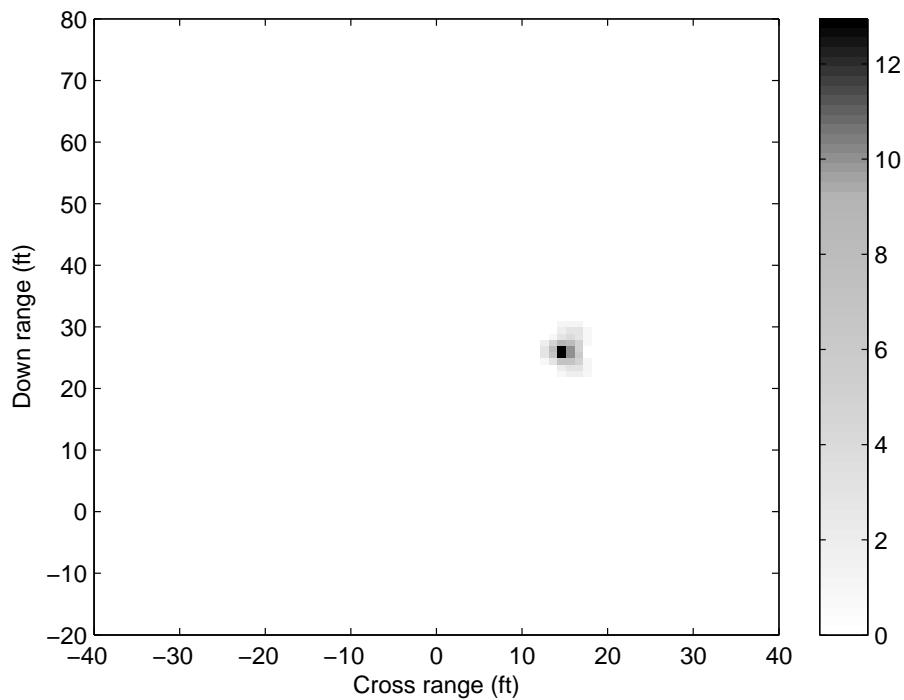
Figure 5.15. Detection map using rudimentary Naïve Bayesian classifier.

It should be noted that the Naïve Bayesian formulation described above uses only the three individual total power signals and the correlation signal as features whereas the heuristic approach used a total of eleven features as noted previously. Thus the Bayesian formulation achieves better results than the heuristic approach using close to 20% of the processing time and less than a third of the number of features.

An alternate Naïve Bayesian formulation uses the natural logarithm ratio of $p(\mathbf{x}|D)$ and $p(\mathbf{x}|N)$ which is called the log-likelihood ratio or *Bayes factor* to classify feature vector and is termed the *Bayes factor* formulation. Taking the ratio of (5.9) and (5.10) and using Bayes' rule yields

$$\frac{p(D|\mathbf{x})}{p(N|\mathbf{x})} = \frac{p(D)\prod_i p(x_i|D)}{p(N)\prod_i p(x_i|N)} = \frac{p(D)}{p(N)}\prod_i \frac{p(x_i|D)}{p(x_i|N)}. \tag{5.16}$$

Taking the logarithm of these ratios gives

$$\ln\frac{p(D|\mathbf{x})}{p(N|\mathbf{x})} = \ln\frac{p(D)}{p(N)} + \sum_i \ln\frac{p(x_i|D)}{p(x_i|N)}. \tag{5.17}$$

The data associated with the feature array is considered a detection if

$$\ln\frac{p(D|\mathbf{x})}{p(N|\mathbf{x})} > 0. \tag{5.18}$$
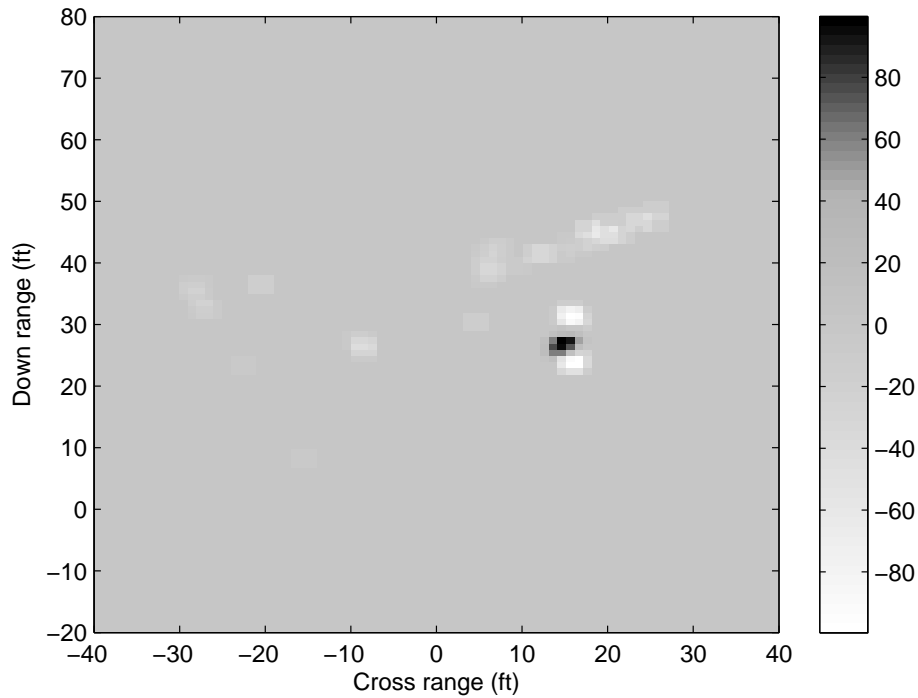
Figure 5.16. Detection map using log-likelihood Naïve Bayesian formulation.

The Bayes factor formulation includes the added benefit of classifying every data point where a laser range hit occurs, which has the effect of reducing the detection of non-humans. The detection map is initialized as a matrix of zeros and as the algorithm runs pixel values are increased or decreased based on the log-likelihood ratio. Thus laser hits that occur on low probability objects have a lower log-likelihood ratio than areas where no determination has been made. In general this has the effect of improving the signal-to-noise ratio of the final map. Figure 5.16 shows the data from Figure 5.15 run through the log-likelihood Naïve Bayesian classifier.

The Bayes factor formulation has an inherent drawback in its classification of non-humans with a low probability of detection. Namely, if a human is present at a large distance, the peaks may not be greater than the threshold. Thus if a person is correctly

detected at close ranges, as the platform passes and the person becomes farther away, the classifier may begin to add negative probabilities to the pixels where the person is located. A method of correcting this is to classify detections with a sliding time window of rotations. Thus the indication to alarm the user of the system would be time-dependent. However, in the current formulation such a method is not implemented and detections are determined on the basis of the entire experiment.

5.4 ENVIRONMENTAL DEPENDENCIES AND TEMPERATURE CALIBRATION

To develop a dependable statistical classifier I needed to determine what dependence the detection method had on different environmental backgrounds. If the statistical distributions of the true positive signals were significantly different in different environments the system would either have to include separate variables in the classifier for each environment, or the system would have to be calibrated to eliminate the statistical difference. This section shows that the signals can be calibrated in order to remove any environmental dependencies and thus eliminate the need for different algorithms in separate environments.

Experiments were conducted in three different environments, each containing a different amount of viewed scenes containing vegetation, man-made materials (concrete, treated wood, metal), and areas of mostly open range giving a mix of radiation from sky reflections, scattering, and thermal radiation. Each scene is show in Figure 5.17. Scene 1 is comprised of approximately 70% man-made, 20% open areas, and 10% vegetation (grass). Scene 2 is approximately 80% open area, 10% man-made, and 10% vegetation. Scene 3 is approximately 85% vegetation and 7% each man-made and open areas.

Scene 1

Scene 2

Scene 3

Figure 5.17. Scenes used for determination of environmental dependencies.

The experiments consisted of the radiometer rotating atop the stationary platform with one person being detected at varying distances. The true positive signal distributions were calculated and compared between the environments using Kolmogorov-Smirnov tests. The Kolmogorov – Smirnov test is a statistical measure of the difference between two distributions. For each data set of N values y_i the empirical distribution function is formed, defined by

$$S_N(x) = \frac{1}{N} \sum_{i=1}^{N} \begin{cases} 1 & \text{if } y_i \leq x, \\ 0 & \text{otherwise.} \end{cases}$$
(5.19)

The Kolmogorov – Smirnov (K-S) statistic is a measure of the maximum difference between the two distributions, given by [40]

$$D = \max_{-\infty < x < \infty} \left| S_{N_1}(x) - S_{N_2}(x) \right|.$$
(5.20)

The significance level of an observed value of D is given by [41]

$$\text{Probability}(D > \text{observed}) = Q_{KS}\left(\left[\sqrt{N_e} + 0.12 + 0.11/\sqrt{N_e}\right]D\right), \qquad (5.21)$$

where the function Q_{KS} is given by

$$Q_{KS}(\chi) = 2\sum_{j=1}^{\infty}(-1)^{j-1}e^{-2j^2\chi^2}, \qquad (5.22)$$

and

$$N_e = \frac{N_1 N_2}{N_1 + N_2}. \qquad (5.23)$$

It should be noted that (5.21) is an approximation, although it is reasonably accurate for values of $N_e \geq 4$. A typical value for $N_{1,2}$ for my system is 1000, resulting in $N_e = 500$, and thus the approximation is accurate.

The signals compared are the K_a-band total power and correlation signals and the W-band total power signal. In addition to the raw signals the absolute value of all three total power signals are also compared. The absolute value signals are analyzed to determine if they provide better probabilities of detection than the normal signals.

The K-S test was conducted with a significance level of $\alpha = 0.05$ or 5%. A K-S statistic measuring below α denotes a statistically significant difference in the distributions. The K-S matrices of the results from the raw data are shown in Figure 5.18. The matrices are thresholded by the significance level; a K-S result above α is set to 1 (black squares) and below α is set to 0 (white squares). It can be seen that the correlation

88

signal (CR) retains similar distributions between scenes, while all other signals show significant differences. Only TP1 shows some similarity between scenes 2 and 3, although not between 1 and 2 or 1 and 3. The reason the correlation signals produce similar distributions from scene to scene is that the correlation signal inherently filters out any DC voltage in the signal. However, the total power signals do not and thus a signal from one scene can have a higher offset than another scene, giving the distributions different means. Figure 5.19 shows the same data with the mean removed from each signal; no signals show significant differences in their distributions. Thus if the mean of the signal can be removed the environmental dependence can be eliminated from the processing algorithm.
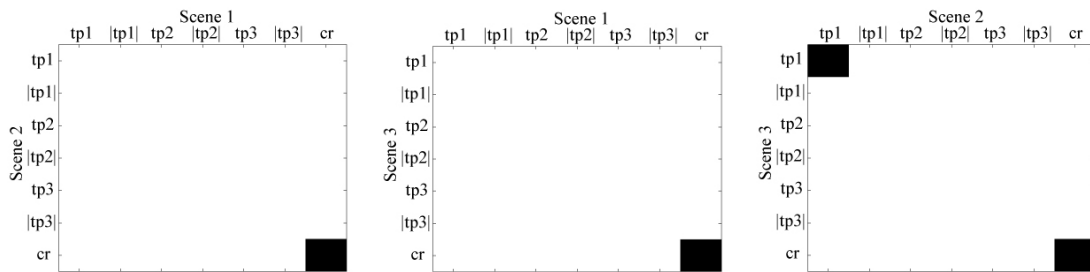
Figure 5.18. K-S matrices. The matrices are thresholded at α; a result above α is set to 1 (black), a result below is set to zero (white). The total power signals (tp1, |tp1|, etc…) show significant differences in their probability distributions from scene to scene while the correlation signal (cr) does not show a significant difference.
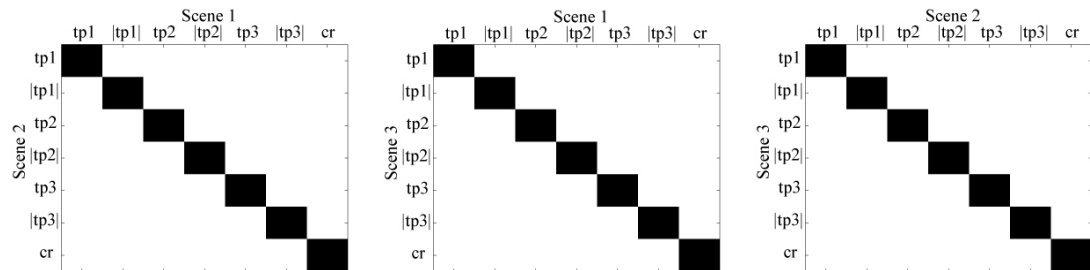
Figure 5.19. K-S matrices with the signal means removed. With the mean removed there is no significant difference in the signal distributions.

Removal of the signal mean on the total power signals can be accomplished by calibrating the receivers to absolute temperature. The probability densities of the response of a human will then have consistent mean from environment to environment.

Calibration of a total power receiver can be done in many ways. The simplest form of calibration is to view a source with known flux density and calibrate all resulting flux densities to this value [42]. However, the gain of the microwave low-noise amplifiers will drift over time, giving incorrect values of temperature or flux density [12, 15]. The calibration can then be repeated, but constant calibration with a known source is not always a viable option. A more reliable solution was introduced by Dicke [43] where a microwave switch is introduced behind the antenna which switches continually between the antenna and a calibrated noise source. This can reliably calibrate the temperature, but results in reduced radiometric sensitivity [12, 16, 43]. Another effective method of calibration involves characterizing the gain drift as a function of component temperature [27] however this method requires all the components of the receiver chain to be tied to a common heat sink.

Because of the difficulty involved in altering the radiometer hardware in order to introduce a microwave switch or temperature characterization, I implemented a calibration source to demonstrate the effect of calibrating the total power channels. The calibration was only tested on one total power channel in order to prove that the mean could be removed, and thus give K-S test results which show no significant differences.
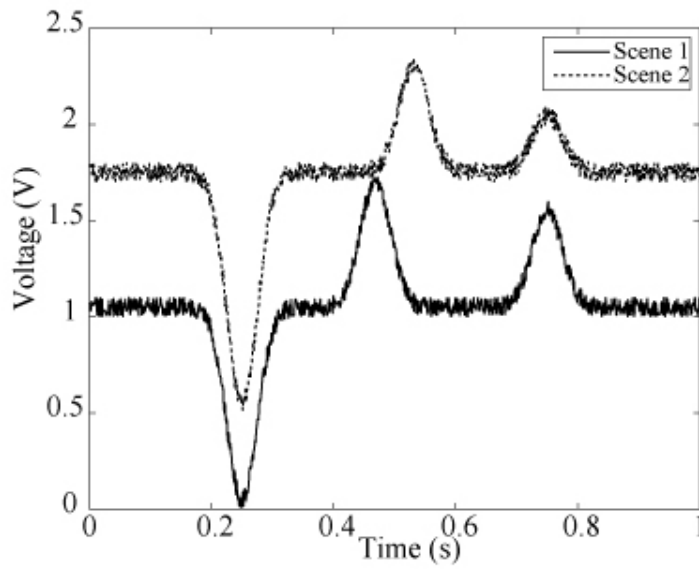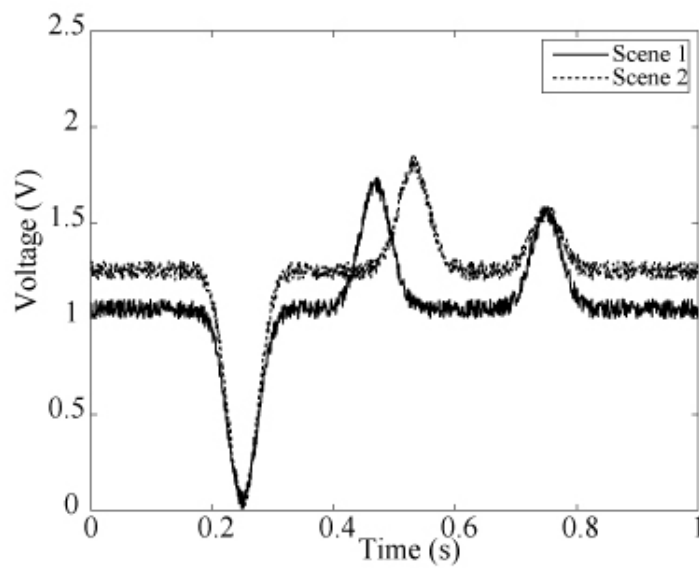
Figure 5.20. (a) Simulated total power signals from two difference scenes prior to calibration. The negative peak at t = 0.25 s is the calibration source, the small peak at t = 0.75 s is a simulated response to a human. The other peaks are simulated background structures. (b) Simulated total power signals after calibration.

The calibration source consisted of a sky reflector placed at the back of the platform. The reflector was a 94 cm × 11 cm strip of aluminum placed at 45° to direct

91

radiation from the sky towards the antennas. The width of the strip was chosen to be slightly greater than β of the K_a-band antennas so as to direct enough of the sky reflection to the antenna without occluding too much of the background scene. As the radiometer rotates the antennas view the calibration source once per rotation at -180°. Figure 5.20(a) shows two simulated total power signals with different offsets. The negative peak at $t = 0.25$ s is the calibration source, the small peak at $t = 0.75$ s is a simulated response to a human. The other peaks are different, simulated background structures, one in each scene. The observed brightness temperature of the sky at 27 GHz varies from 15 to 30 K depending on whether conditions are dry, moderate, or humid, but can be accurately specified based on the conditions [44], thus the sky reflection will produce a total power response with a much lower apparent brightness temperature than any other objects in a natural scene. This lowest point per rotation in the signal is then set to a specified value; the sky temperature if the conditions are known, or in this case, the low point is set to zero volts. The resulting voltage signals are shown in Figure 5.20(b). The simulated human response normalizes to a constant temperature between the scenes.

The probability density functions of the two full signals still have different statistical means (see Figure 5.21(a)) and thus the K-S test will results in a significant difference. However, the signals resulting from only the human responses are now normalized and their statistical means are similar (see Figure 5.21(b)). Thus the K-S tests will show no significant difference in the distributions, resulting in the K-S matrices seen in Figure 5.19.

(a)

(b)
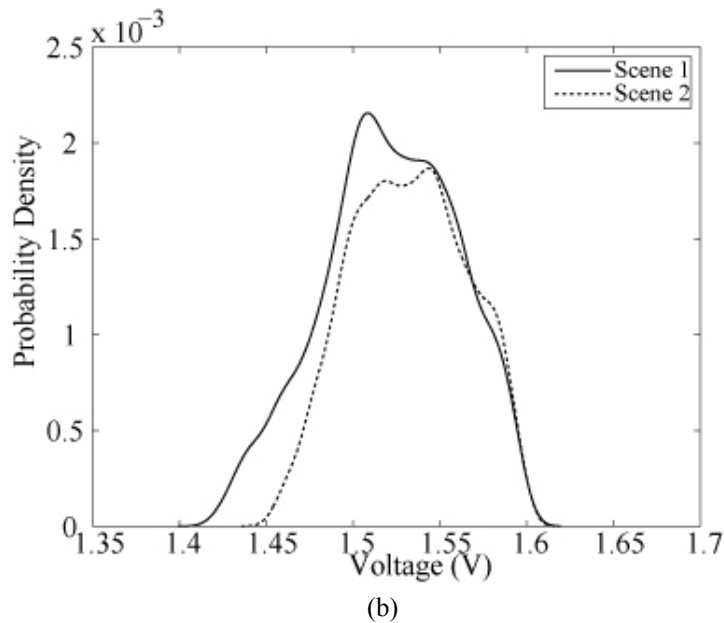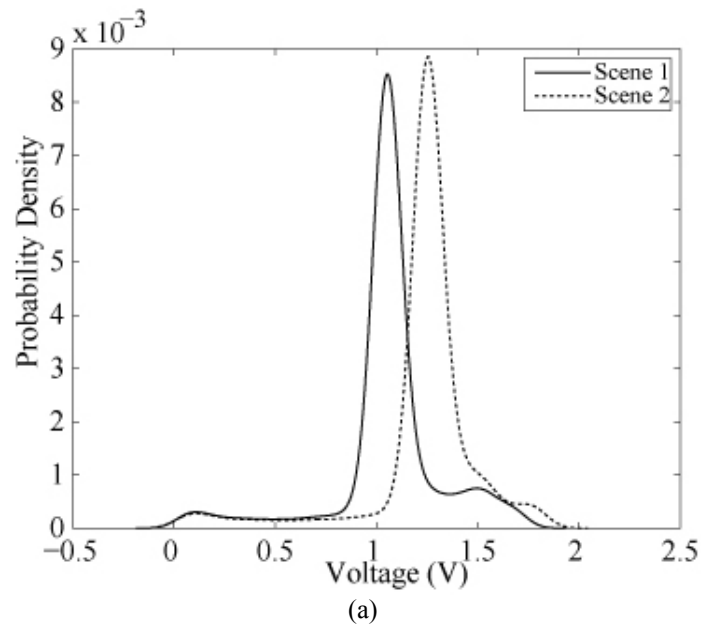
Figure 5.21. (a) PDF of the full signals in Figure 5.20(a). (b) PDF of only the human response.

To demonstrate this procedure experimentally, the total power signals were measure in scenes 1 and 2 with the calibration sky reflector in place. Scene 3 was not included because overhead vegetation from tree limbs occluded the sky. However, as the

point is to show that the signal means can be normalized by temperature calibration, demonstration between the two scenes was considered adequate. Following the calibration process the calculation of the statistical means of the human responses over the range of 1.8 to 12.2 m resulted in

$$\mu_1 = 0.869 \text{ V} \qquad\qquad (5.24)$$
$$\mu_2 = 0.870 \text{ V} \qquad\qquad (5.25)$$

or a difference of 0.004 or 0.5%. The probability density functions of the calibrated signals due to the humans are shown in Figure 5.22. Running a K-S test on the signals results in a value of $p = 0.358$, which is well above the significance level of 0.05, indicating that the distributions show no significant difference. Thus the calibration successfully removed the environmental bias.
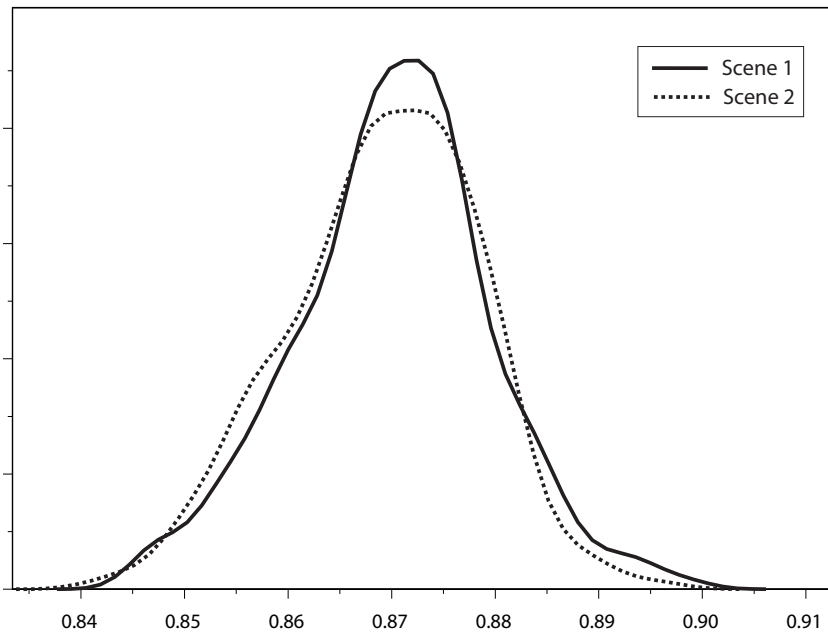
Figure 5.22. Measured PDFs of temperature calibrated signals due to human responses.

The method of temperature calibration presented here showed that the detection method may be used independent of the operating environment. However, the implementation of the temperature calibration is not very practical. The prominent drawback is the loss of coverage over a non-trivial portion of the viewed scene. Also, the frequency with which the signals are calibrated is not as accurate as it might need to be in other applications. Typical Dicke radiometer setups require the system to switch to the calibration temperature at a rate twice as fast as the integration time of the baseband amplifier [16]. While this is not impractical, it would require a high-speed waveguide switch at the antenna output and would result in lower radiometric sensitivity.

Chapter 6: Experimental Results and Performance Evaluation

The performance of the detection method using the Naïve Bayesian classifier is analyzed in this chapter. The experimental validation set is discussed and some intermediate results are shown. I follow by discussing the metrics used to evaluate the classifier and how they are affected by the balance of positive and negative instances in the data set.

6.1 EXPERIMENTAL SETUP

The evaluation data set consisted of sixteen different experiments in environment 1 of Figure 5.17. The results of the temperature calibration allowed me to conduct the evaluation sets in any location and environment 1 was chosen because of the diversity in the radiometric background. Each experiment consisted of approximately 30 rotations, resulting in ~500 rotations with which to evaluate the performance of the detection method. Each rotation produces ~1000 data points on each of the four sensors.

The experiments consisted of one person standing at varying distances from the path of the moving platform, from a closest approach of 4 ft to a closest approach of 18 ft. Note that the closest approach is not indicative of the maximum range of the sensor and is only the minimum distance that the person is from the platform. The platform moved at ~1 m·s^{-1} and the rotation rate of the platform was ~2π rad·s^{-1}. Two different locations within environment 1 were used, each providing a different direct backdrop to the person. Figure 6.1 shows an overhead diagram of the experimental setup.
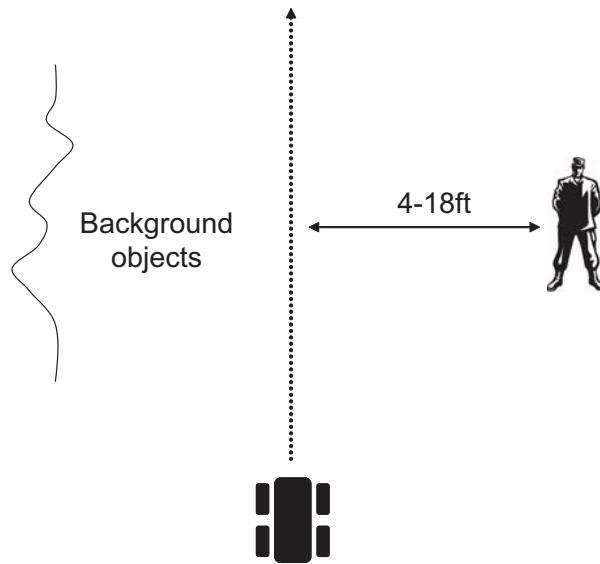
Figure 6.1. Experimental setup for the validation data tests.

6.2 INTERMEDIATE EXPERIMENTAL RESULTS

The raw data result of total power 1 is shown in Figure 6.2. The scan map is formed by plotting the sensor output per rotation as a function of rotation angle. The tracks on either side of the map represent objects as they pass the platform. The faint track seen at 80˚ and 12-15 rotations is the response from the person. In its raw unfiltered form the total power response from the person can be difficult to detect. The following figures show the total power scan map as it is filtered by range using the median filters. Figures 6.3 through 6.6 show the total power scan maps resulting from median filtering the total power signal for regions 1 through 4, respectively. The total power signals are analyzed per rotation in the detection and classification algorithms, but I present the results as maps representing the entire experiments in order to better elucidate the processes.
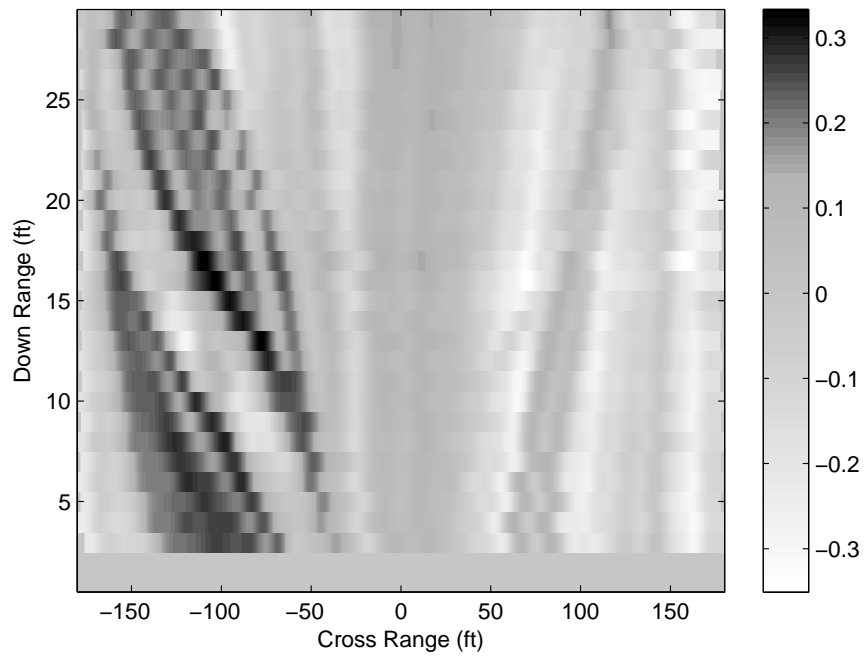
Figure 6.2. Total power 1 scan map of raw data.
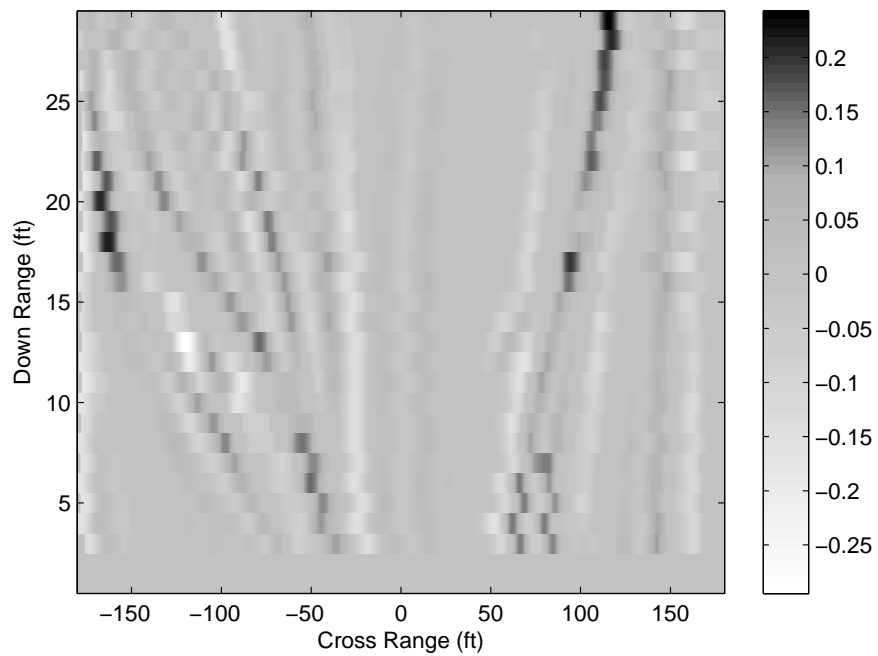
Figure 6.3. Total power 1 scan map after median filtering in range region 1.
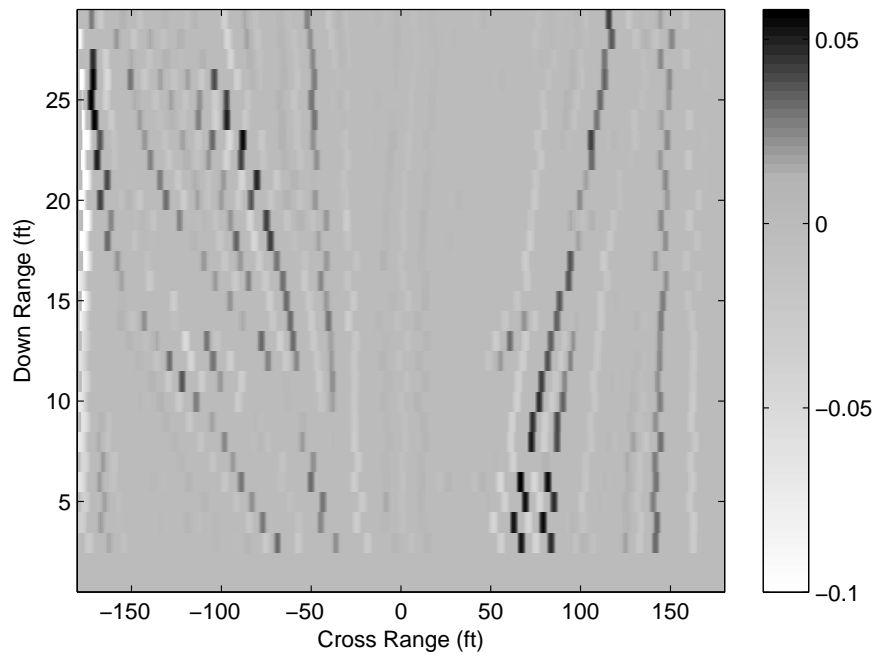
Figure 6.4 Total power 1 scan map after median filtering in range region 2.
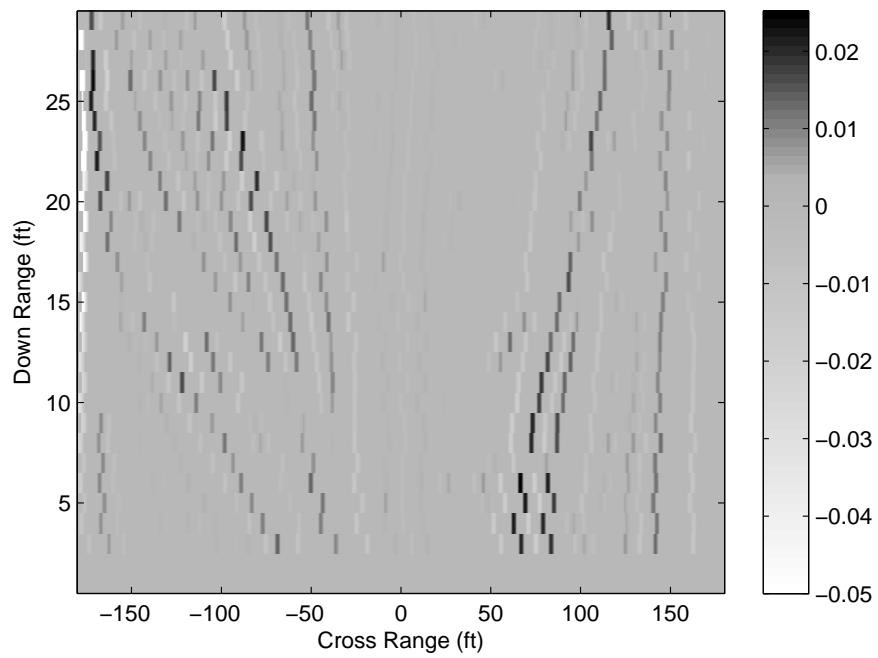
Figure 6.5 Total power 1 scan map after median filtering in range region 3
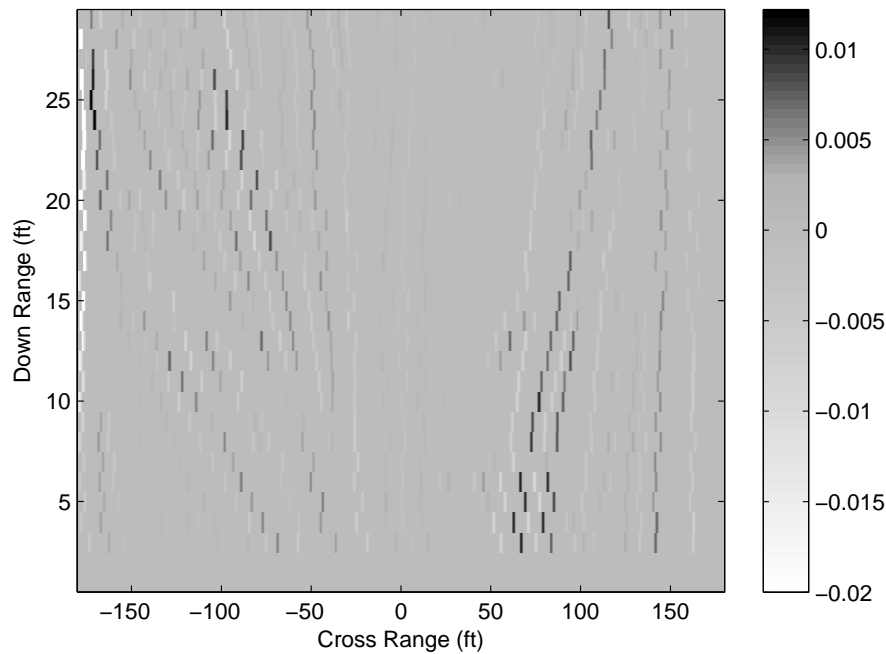
Figure 6.6Total power 1 scan map after median filtering in range region 4

All four signals are then processed in the Naïve Bayesian classifier and a probability of detection is calculated for each point. Figures 6.7 though 6.10 show the results of thresholding the individual total power 1 signal. The black areas denote where the signal level is greater than or equal to the detection threshold for the individual signal. It can be seen that the response from the person is consistently prominent through the median filtering process over the four regions. However, there are also a number of other tracks seen on either side of the graph. These tracks represent objects or regions which are moving slowly compared to the platform, as their angle changes slowly per rotation. This means that the objects or regions producing these responses are very distant from the sensors and will be filtered out in the creation of the *x-y* detection map. Because each sensor sees these distant objects at different angles (due to the angle of the antennas), the probability of detection from the combines sensors will help to remove these responses.

100
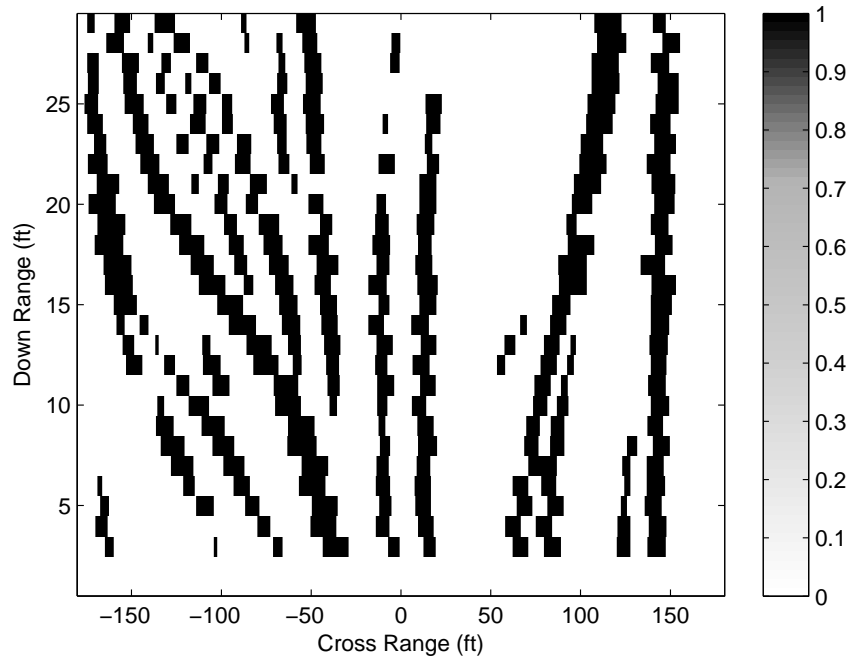
Figure 6.7. Thresholded total power 1 signal in region 1.
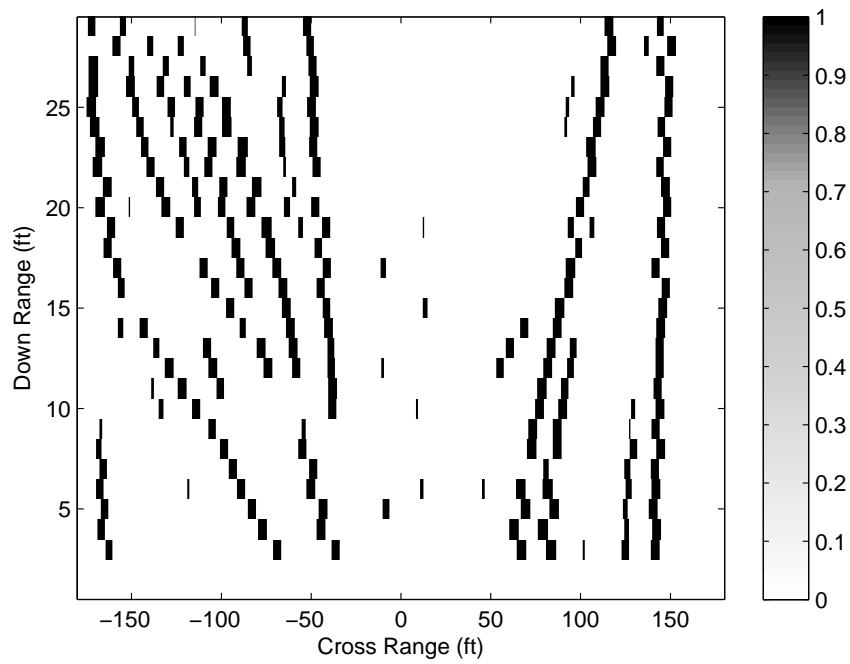
Figure 6.8. Thresholded total power 1 signal in region 2.

101
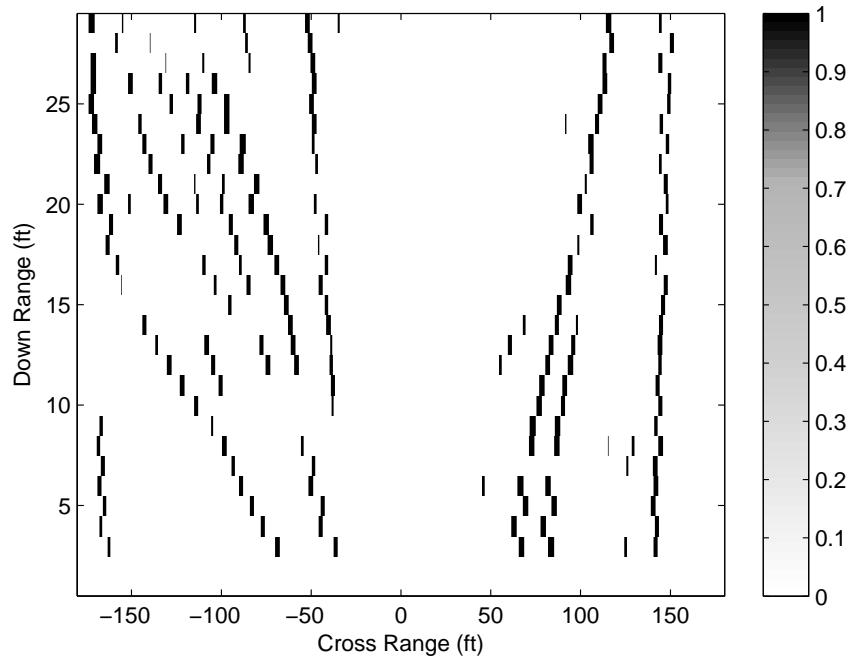
Figure 6.9. Thresholded total power 1 signal in region 3.
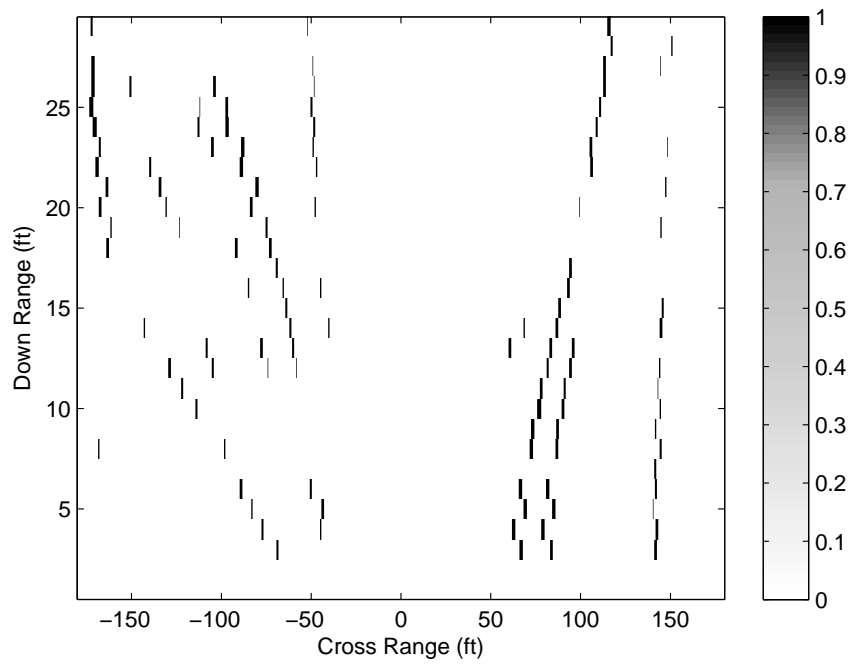
Figure 6.10. Thresholded total power 1 signal in region 4.
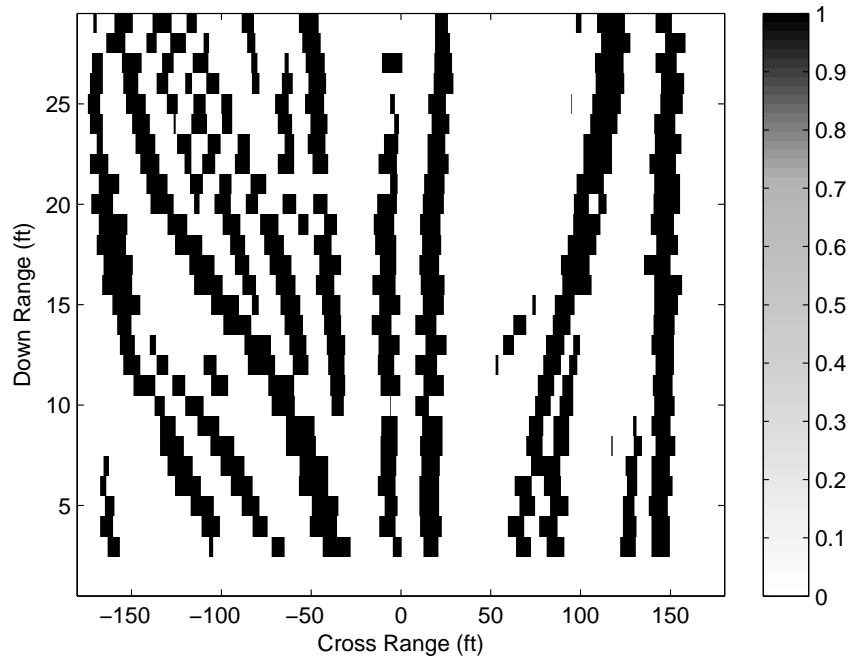
Figure 6.11. Thresholded total power 2 signal in region 1.
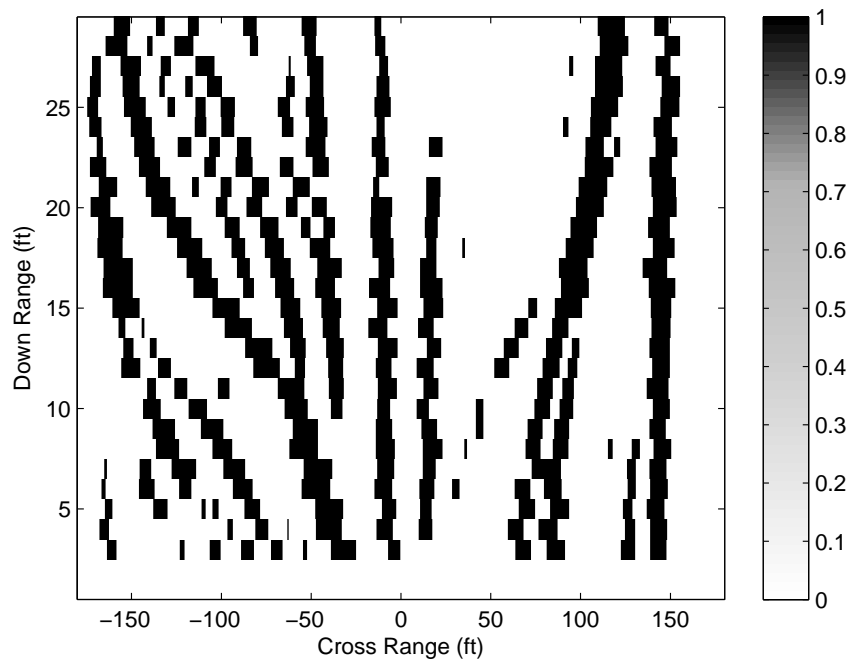
Figure 6.12. Thresholded total power 3 signal in region 1.

103
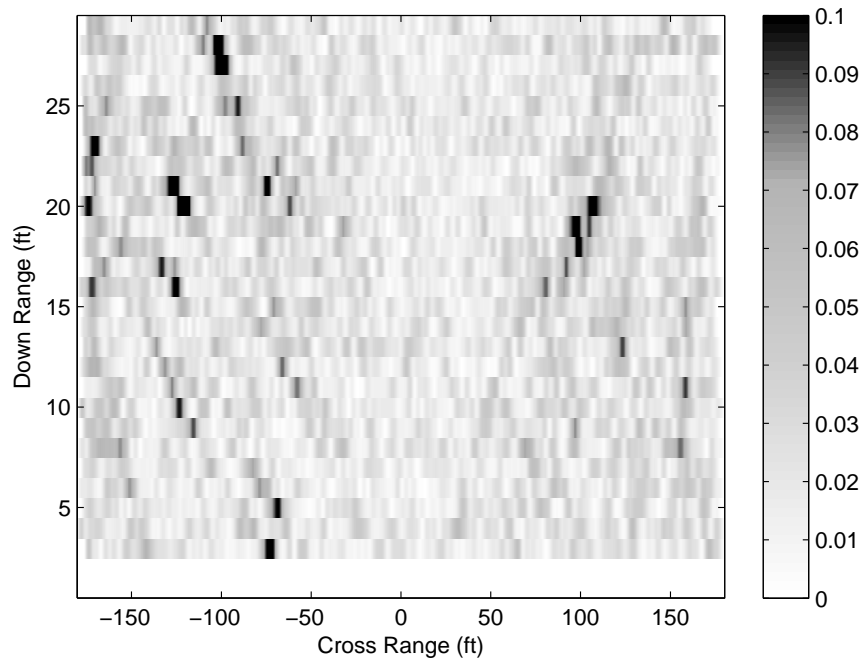
Figure 6.13. Raw spectral correlation signal.
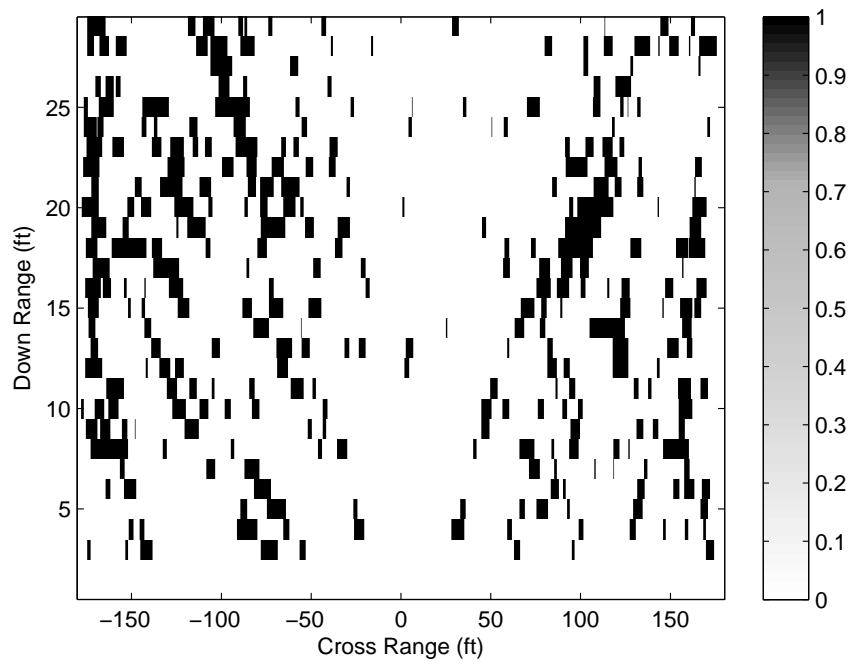
Figure 6.14. Thresholded spectral correlation signal in region 1.

The individual probability of detection scan maps for total power 2 and total power 3 are shown in Figures 6.11 and 6.12 for region 1. Figure 6. 13 shows the raw spectral correlation signal scan map. It can be seen that there is a prominent response from the person on the right side of the graph. Figure 6.14 shows the detection scan map resulting from thresholding the spectral correlation signal.

The full detection probability scan maps resulting from all four signals in the four different regions are shown in Figures 6.15 though 6.18. The response from the human is still present but diminishes as the range region increases. However, many of the distant false detections are also reduced. While some still remain, most will be removed during the range determination process, by either the passive or active ranging.
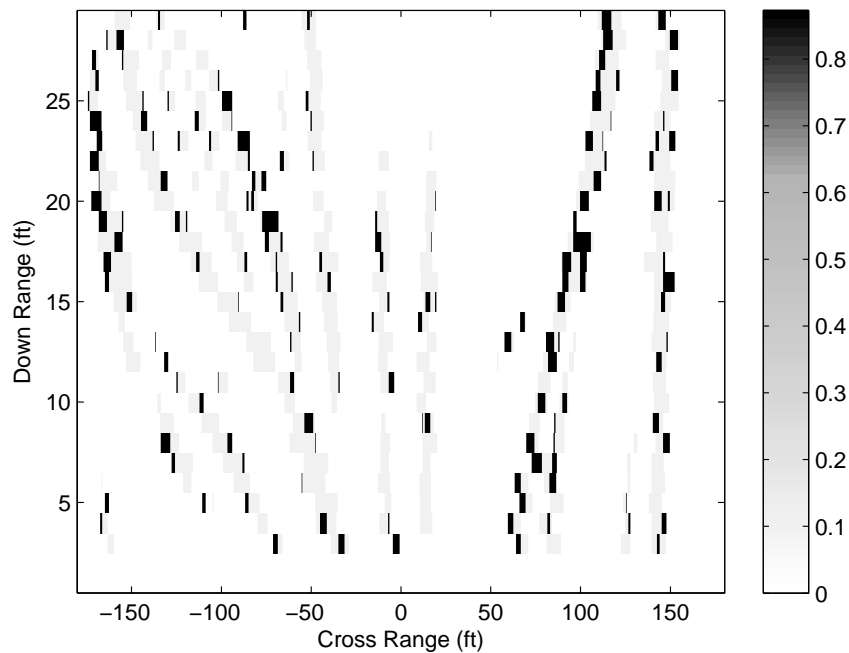
Figure 6.15. Detection probability in region 1.
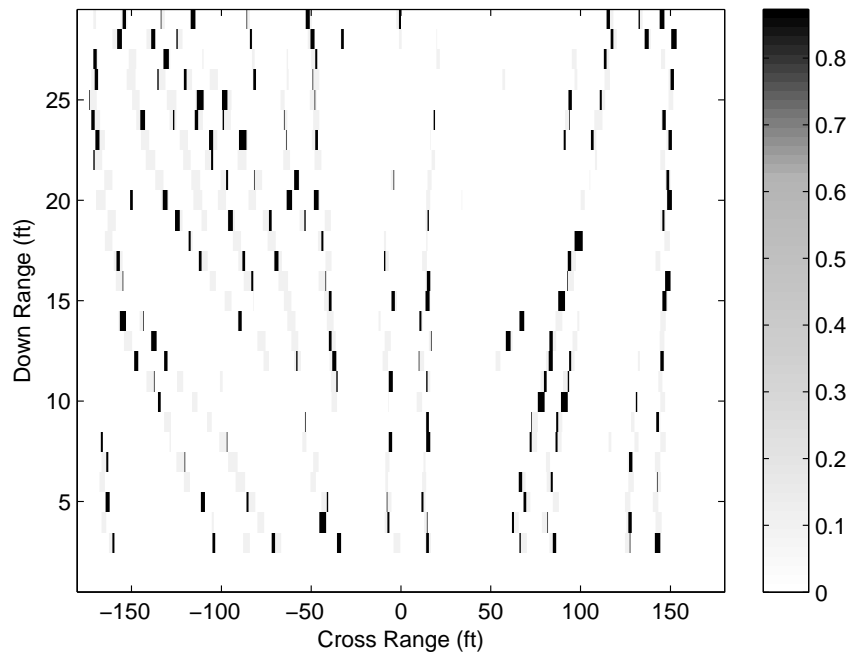
Figure 6.16. Detection probability in region 2.
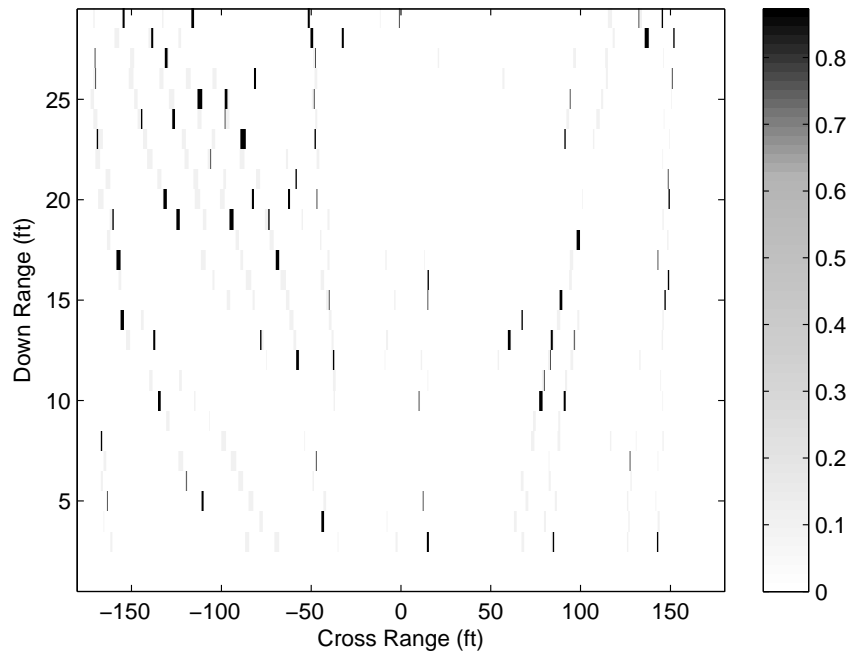
Figure 6.17. Detection probability in region 3.
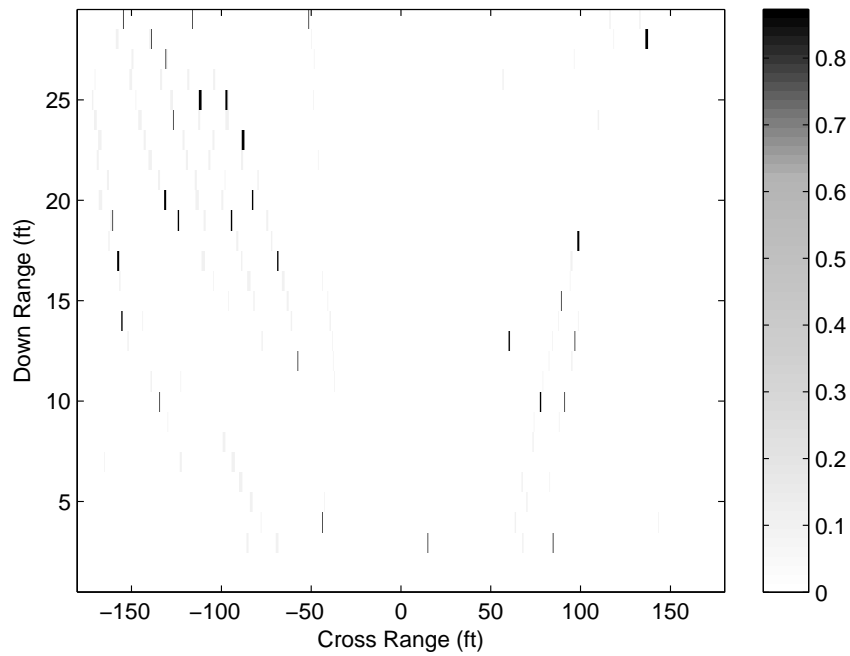
Figure 6.18. Thresholded spectral correlation signal in region 4.
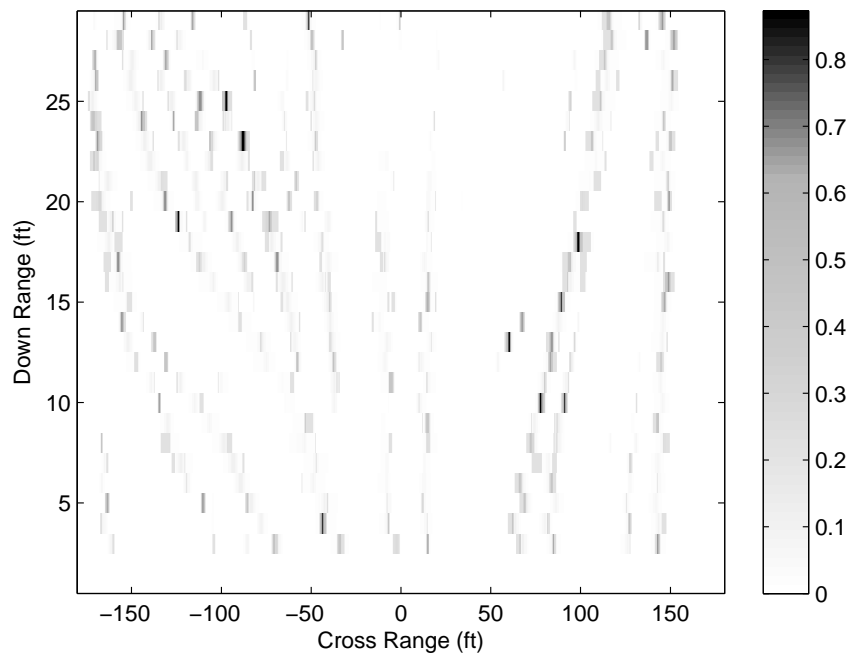
Figure 6.19. Combined detection probability for the entire experiment.

The final detection map is formed by correlating the passive or active range to the detection probability. The range and angle information allows the creation of the *x-y* map. The detection map resulting from correlating the detection probability scan map (Figure 6.19) with the active range is shown in Figure 6.20. The detection map using the passive range is shown in Figure 6.21. The passive range shows considerable error in the range estimation, although the range estimates tend to cluster in the areas where objects are present. The active range can be viewed as a more accurate measure of present objects, although not all objects reflect the laser light enough to register a detection, and can be used as a measure of the accuracy of the passive range. The detection map from the combined active and passive range is shown in Figure 6.22. The final detection map is formed by thresholding the probability of detection at the chosen cutoff level and is shown in Figure 6.23 for a cutoff level of 0.5. Thus detection with a confidence level greater than or equal to 0.5 is classified as a detection.
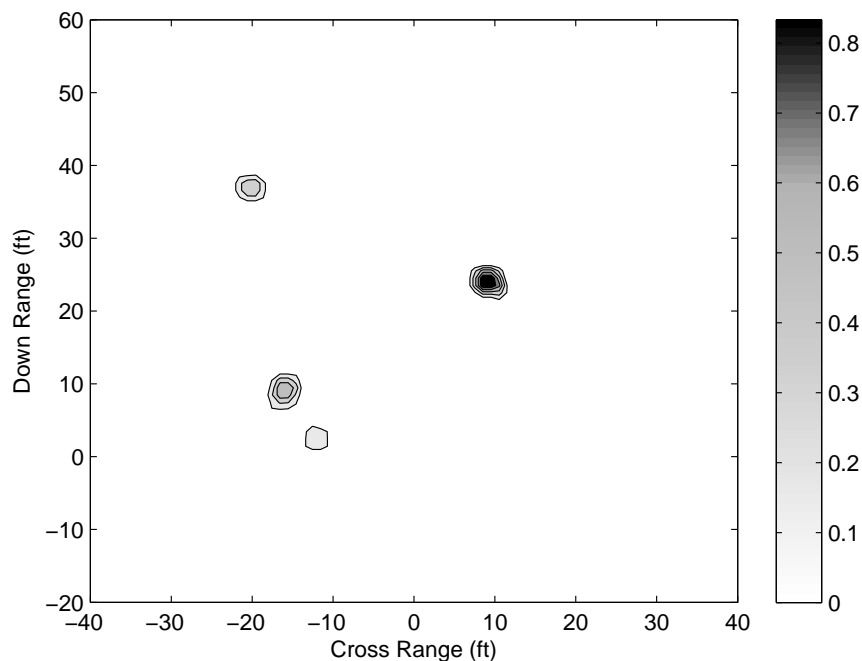
Figure 6.20. Detection map from active range.
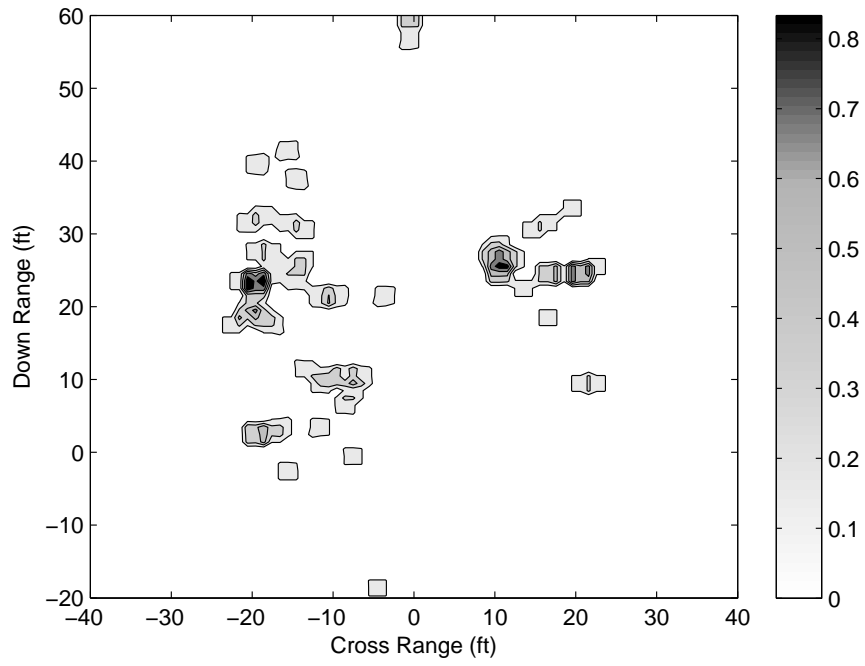
Figure 6.21. Detection map from passive range.
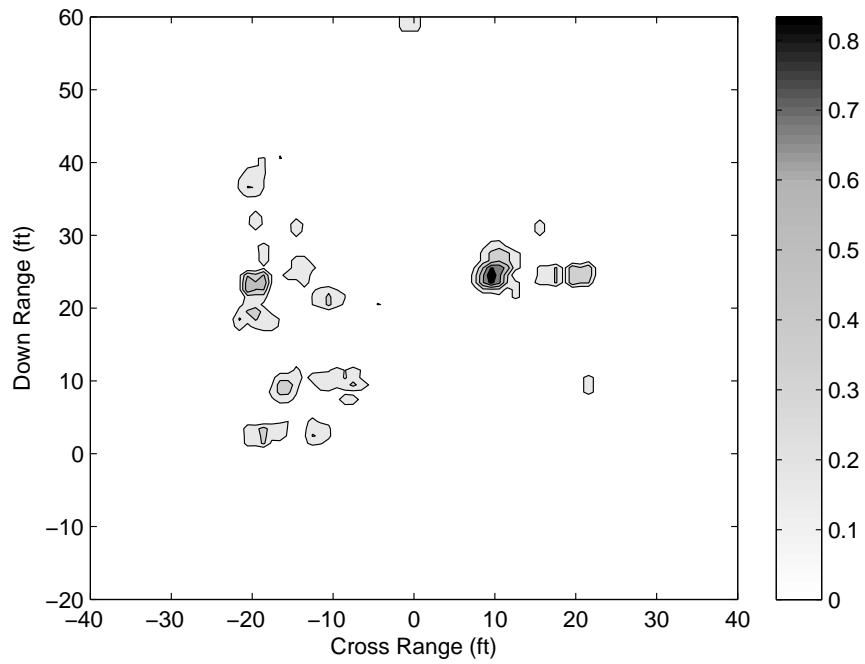
Figure 6.22. Detection map from combined active and passive range.
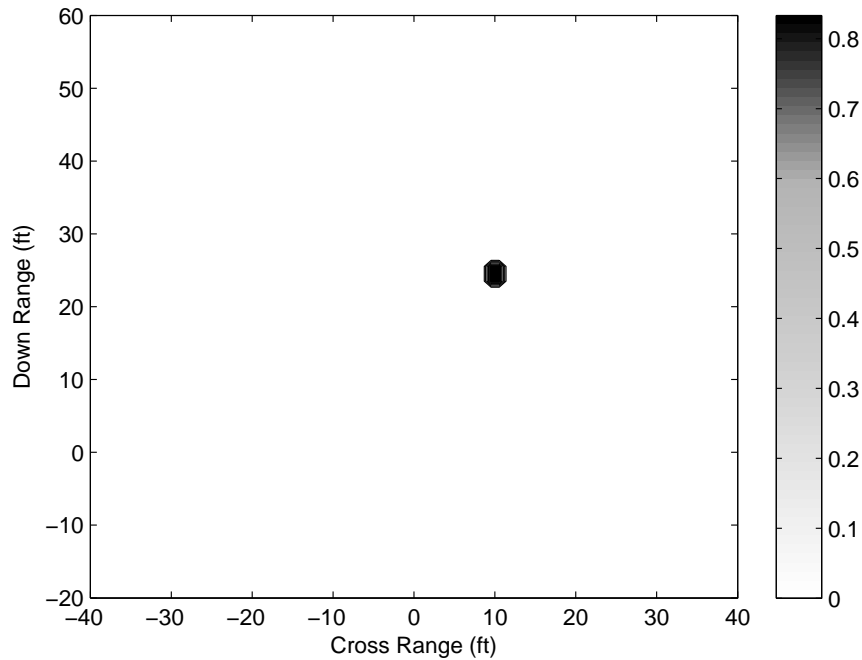
Figure 6.23. Final detection map with thresholded detection confidence.

6.3 CLASSIFIER PERFORMANCE METRICS

To focus on the capabilities of the passive sensor alone, the performance was analyzed by using the resulting passive detection maps. Final results are also shown using the total detection map, which uses both the passive and active ranging, for completeness.

6.3.1 Confusion Matrix and Typical Performance Metrics

When defining measures of the performance of a classifier, researchers often use the *confusion matrix*, shown in Table 6.1. The *positive* case is typically the case of interest in the classification; here the positive case is the classification of a human. The *negative* case is the classification of non-humans. The confusion matrix shows the number of *true positives* (TP), which are correctly predicted positive instances; *false*

negatives (FN), which are positive instances incorrectly classified as negative; *false positives* (FP), which are negative instances incorrectly classified as positive; and *true negatives* (TN), which are correctly classified negative instances.

To evaluate the performance of the Naïve Bayesian classifier I employ a number of widely used metrics. A commonly used metric which is derived from the confusion matrix is the *accuracy*, given by

$$AC = \frac{TP + TN}{TP + TN + FP + FN}.$$

(6.1)

The accuracy provides a good measure of the classifier providing that the data sets are appropriately balanced; that is, the number of positive instances must be on the order of the number of negative instances.

The *true positive rate* (TPR) is a measure of how well the classifier identifies the positive case and is alternatively called the *sensitivity* or *recall rate*. It is defined by

$$TPR = \frac{TP}{TP + FN}.$$

(6.2)

A TPR of 1 indicates that the classifier correctly classifies all positive instances. Note that this metric does not indicate how well the classifier identifies other cases.

Table 6.1. Confusion Matrix

		Predicted	
		Positive	Negative
Actual	Positive	TP	FN
	Negative	FP	TN

The *true negative rate* (TNR) is defined as

$$TNR = \frac{TN}{TN + FP},$$ (6.3)

and is alternatively referred as the *specificity*. The TNR indicates how well the classifier correctly identifies negative instances. Other similar metrics are the *false positive rate* and the *false negative rate*, given by

$$FPR = \frac{FP}{TN + FP},$$ (6.4)

$$FNR = \frac{FN}{TP + FN}.$$ (6.5)

The FPR is important is measuring how well the classifier rejects nuisance alarms and is important in applications such as security monitoring.

Table 6.2. Example Confusion Matrix

		Predicted	
		Positive	Negative
Actual	Positive	115	250
	Negative	250	10550

6.3.2 Imbalanced Data Sets

When one of the classes in a binary classification problem constitutes a small minority of the entire data set the classification problem is called *imbalanced*. There are many practical situations where such a classification arises, including the detection of rare diseases and information retrieval. In such a case the accuracy no longer provides a

good representation of how well the classifier works. For instance, take the confusion matrix of Table 6.2. This confusion matrix has a *percent minority* of

$$\%M = \frac{TP + FN}{TP + TN + FP + FN}$$

$$= \frac{115 + 250}{115 + 10550 + 250 + 250} \qquad (6.6)$$

$$= 3.26\%.$$

A data set is typically considered imbalanced if the percent minority is below 10%. The accuracy of the classifier represented by the confusion matrix is

$$AC = \frac{115 + 10550}{115 + 10550 + 250 + 250} = 0.9552. \qquad (6.7)$$

This indicates that the classifier is correct 95% of the time, however it can bee seen that of the 365 total positive cases (TP + FN) the classifier correctly classified only 115 instances, or 32% of the time. Thus for imbalanced data sets the accuracy measure is typically not useful.

In some cases the imbalanced stat problem is approached by altering the number of instances in the training data set. Techniques used are oversampling the minority case, undersampling the majority case, or both [45]. Oversampling the minority case involves techniques such as replication of the minority instances or creation of synthetic minority instances. Introducing additional positive cases into the training set by methods such as replication does not change the amount of information provided, but changes the weight applied to the minority data instances. Likewise, undersampling of the majority cases

113

involves removal of majority instances and has the effect of decreasing the weight applied to the majority case. In either method, the goal is to approach normalization of the number of instances of both the minority and majority cases.

6.3.3 Performance Measures for Imbalanced Data Sets

The percent minority of the data set for the detection method presented in this dissertation was 5.73%. The minority case is the positive case, which is the detection of a human while the majority case is the negative case which is the detection of anything other than a human. Because a human comprises only a small fraction of the detected data points in the detection map, the number of positive cases is very small.

Instead of altering the training set by undersampling the majority case or oversampling the minority case, I used a metric that is typically used to evaluate binary classifiers under an imbalanced data set, the F_α-measure [45, 46], defined by

$$F_\alpha = \frac{(1+\alpha)P \times TPR}{\alpha P \times TPR}.$$ (6.8)

where P is the *precision*, or *positive predictive value*, which is a measure of the predicted positives which are true positives and is defined by

$$P = \frac{TP}{TP+FP}.$$ (6.9)

The F_α-*measure* is the harmonic mean of the precision and the recall (true positive rate) and is has been used in the information retrieval area. The F_1-*measure* equally weights the precision and recall by setting $\alpha=1$, resulting in

$$F_1 = \frac{2P \times TPR}{P + TPR}.\qquad\qquad\qquad (6.10)$$

Other commonly used values are $\alpha=2$, which weights the recall twice as much as the precision, and $\alpha=0.5$, which weights the precision twice as much as the recall. I will use the F_1 metric in this dissertation.

6.3.4 Receiver Operating Characteristic

In practice it is necessary to evaluate the TPR and FPR for a sensor that will be deployed in an environment such as a security setting. For a binary classifier a graphical representation of the tradeoff between TPR (sensitivity) and the FPR (1–specificity) can be created which is called the *receiver operating characteristic* or *ROC* curve. Initially created to evaluate the performance of radars, the ROC curve is now used in numerous applications where binary classification is used; often the ROC curve is used to evaluate the performance of medical tests for diseases.

In the final data set a cutoff value is set where any value above the cutoff is classified in the positive class and anything below is classified in the negative class. By varying the cutoff the ROC curve is calculated. At a cutoff of 0, the classifier will classify every instance in the positive class, resulting in a TPR=1, since all positive instances are correctly classified; but this also classifies all negative instances in the positive class, resulting in FPR=1. At the other end of the curve, the cutoff is set to is maximum value (normalized to 1), resulting in FPR=0, but also TPR=0 since all instances are classified as negative. ROC curves are often plotted against a *random guess classifier* which has an

equal probability of classifying an instance as positive or negative. Anything performing equal to or worse than the random guess is typically considered useless as a classifier.

A commonly used metric to evaluate a classifier based on its ROC curve is calculating the area under the curve (AUC). A perfect classifier will have AUC=1, while if the classifier is no better than a random guess it will have AUC=0.5.

6.4 PERFORMANCE EVALUATION

The probability detection maps from the validation data set were analyzed by altering the threshold cutoff for determining the classification of instances. With prior knowledge of the position of the person in the experiment the positive instances were differentiated from the negative instances. The probability maps are normalized, and thus the cutoff value was varied from 0 to 1 in increments of 0.1. Tables 6.3-6.7 show the confusion matrix for the detection maps for cutoff values ranging from 0.3-0.7.

Table 6.3. Confusion Matrix: Cutoff = 0.3

		Predicted	
		Positive	Negative
Actual	Positive	132	11
	Negative	278	2076

Table 6.4. Confusion Matrix: Cutoff = 0.4

		Predicted	
		Positive	Negative
Actual	Positive	125	18
	Negative	186	2168

Table 6.5. Confusion Matrix: Cutoff = 0.5

		Predicted	
		Positive	Negative
Actual	Positive	116	27
	Negative	80	2274

116

Table 6.6. Confusion Matrix: Cutoff = 0.6

		Predicted	
		Positive	Negative
Actual	Positive	89	54
	Negative	51	2303

Table 6.7. Confusion Matrix: Cutoff = 0.7

		Predicted	
		Positive	Negative
Actual	Positive	75	68
	Negative	32	2322

The confusion matrices are used to compute the precision and the true positive rate and in turn compute F_1. I use F_1 to measure the performance of the classifier while TPR and FPR are used to measure the practical performance of the system. Figure 6.24 shows F_1 plotted against the cutoff number. The performance peaks at a cutoff rate of 0.5 and thus I use this as the operating point for the classifier. The peak value is $F_{1,0.5} = 0.6844$.

The receiver operating curve is shown in Figure 6.25 for all 11 cutoff values using only the passive ranging to develop the detection map. The Naïve Bayesian classifier of this dissertation reasonable performance compared to a random guess; the area under the ROC curve was calculated as

$$AUC_{passive} = 0.9392. \tag{6.11}$$

However, at 90% detection probability the false positive rate is nearly 20%. This is not good enough for a system to be deployed directly to an application environment. However, the results are promising considering the novel aspects of the detection method.

117

In the concluding chapter of this dissertation I discuss possible improvements that may increase the effectiveness of this detection method.

Figure 6.26 shows the ROC curve from the detection maps when including the active ranging component. It can be seen that at a detection probability of 90% the false positive rate is improved two-fold to about 10%. The area under the curve is

$$AUC = 0.9753. \tag{6.12}$$
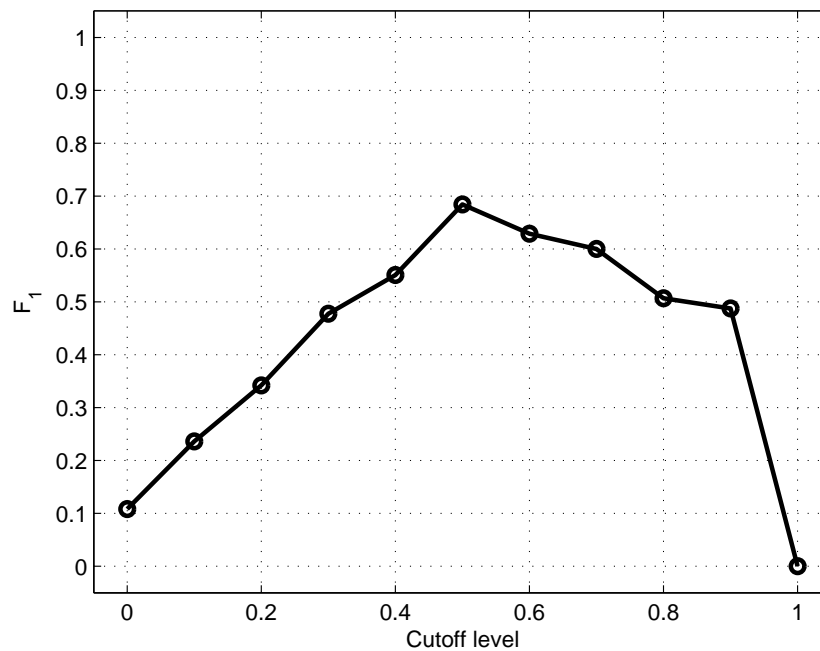
Figure 6.24. F_1 plotted against the cutoff level.
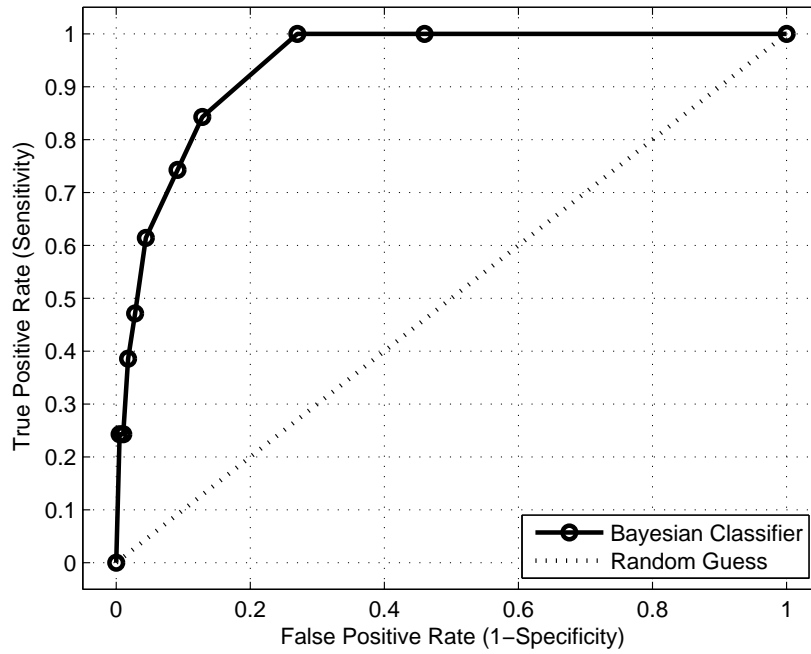
Figure 6.25. Receiver operating characteristic for the passive ranging method.
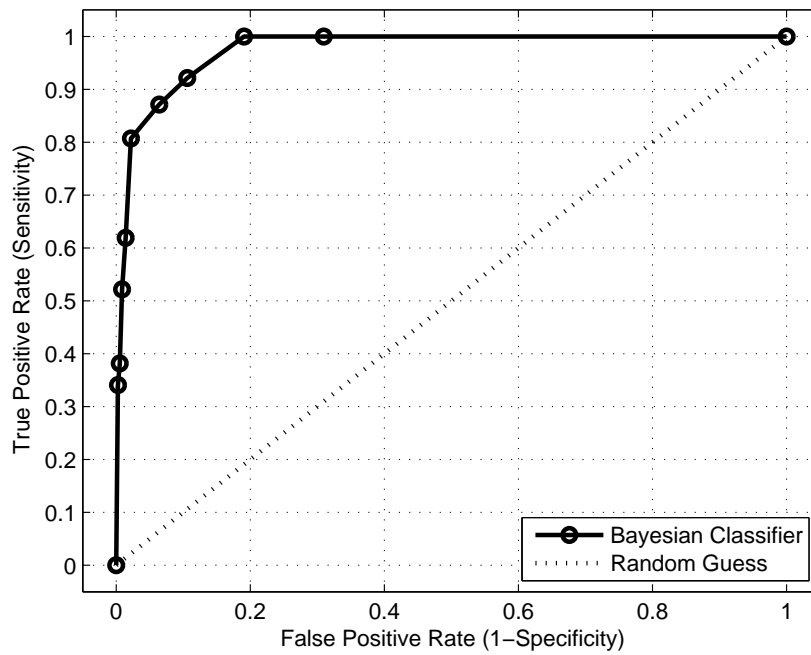
Figure 6.26. Receiver operating characteristic including the active ranging.

119

The F_1 value at the 0.5 cutoff is reasonable, at about 0.7. F_1 is the harmonic mean of the recall and the precision and it is the precision which brings the value down. The recall is approximately 0.8. The F_1 value indicates that the classifier could be more robust in eliminating false positives, which would bring the precision value up. However, with $F_1 \approx 0.7$ the classifier cannot be considered useless by any means, and indeed due to the novel nature of the detection method being employed the metric indicates that the method shows promise.

The AUC values of the ROC curves indicate that the detection method actually performs very well compared to a random-guess classifier. For site security monitoring purposes, however, the false alarm rates of 10-20% are too high. Again, the number of false positives needs to be reduced to improve the performance. To achieve this, the passive estimation needs to be improved. This could be done be developing a linear estimator and using the active range to calibrate estimator.

6.5 OTHER PERFORMANCE METRICS

I use F_1 and the ROC curve as the main performance measures of the detection method presented in this dissertation. However, I also investigated a number of other performance metrics, many of which are useful for evaluating classifiers under imbalanced data sets. I present these metrics and their results for a more complete view of the classifier, although I maintain the previous metrics as the main performance evaluators.

The FNR can be used to calculate the *power* of the classifier which is the probability that the test will not make a Type II error. The power is given by

$$p = 1 - FNR. \tag{6.13}$$

One typical metric measures the geometric mean between TPR and TNR. I refer to this as *g-mean*$_1$ and it is defined by

$$g - mean_1 = \sqrt{TPR \times TNR}. \tag{6.14}$$

This metric has been used to measure other imbalanced data sets, such as the detection of oil slicks on the ocean surface from satellite radar images in [47], where the percent minority was 4.4%. The *g-mean*$_1$ metric is independent of the distribution of the cases, and thus maintains its effectiveness in cases where the training set distribution differs from the validation set.

A similar metric used is called *g-mean*$_2$ and calculates the geometric mean between TPR and P and is defined by

$$g - mean_2 = \sqrt{TPR \times P}. \tag{6.15}$$

Both *g-mean*$_1$ and *g-mean*$_2$ achieve the goal of producing a single quantity which is typically used in the comparison of multiple classifiers. Because this dissertation does not compare classifiers I present the results from multiple metrics to measure the effectiveness of the Naïve Bayesian classifier in the context of human presence detection.

Finally, I used the *weighted accuracy*, defined by [45]

$$W = \beta TPR + (1 - \beta) TNR. \tag{6.16}$$

121

This metric is typically used to measure classifiers under imbalanced data sets when it is important have high accuracy in predicting the minority case and have only decent accuracy in the prediction of the majority case. The weight β can be adjusted to increase (or decrease) the weight on TPR, which places more (less) emphasis on predicting the minority class. For this dissertation I weight TPR and TNR equally by setting β=0.5.

The confusion matrices are used to calculate the metrics described in the previous sections. The metrics are analyzed for the five cutoff values shown in the above tables with the results shown in Table 6.8. Aside from the TPR and FPR, which improve with decreasing cutoff independent of the classifier, and TNR and FNR, which improve with increasing cutoff independent of the classifier, the best values for each metric are presented in bold. The accuracy AC has better performance as the cutoff increases due to the imbalanced data set: TN increases with increasing cutoff and is a majority case, thus as the cutoff rises, TN increases, pushing AC closer to 1. As mentioned earlier, this is not a particularly useful metric for imbalanced data sets and the results here demonstrate why.

The precision also benefits from increasing cutoff. However, P only takes into account TP and FP, and as can be seen in the confusion matrices, FN increases with each increasing cutoff as well. The power p decreases with increasing cutoff, indicating that the classifier becomes more likely to make a Type II error. As the cutoff rises, $g\text{-}mean_1$ decreases, indicating worsening performance. This is the same for W as well.

The metrics $g\text{-}mean_2$ and F_1 both show a peak in performance at the 0.5 cutoff level. Because these two metrics are the geometric and harmonic means, respectively, of the precision and the recall, these metrics provide more insight into the performance of a classifier under an imbalanced data set.

Table 6.8. Other Performance Metrics

Metric		Cutoff Value				
		0.3	0.4	0.5	0.6	0.7
Metric	TPR (6.2)	0.9231	0.8741	0.8112	0.6224	0.5245
	TNR (6.3)	0.8819	0.9210	0.9660	0.9783	0.9864
	FPR (6.4)	0.1181	0.0790	0.0340	0.0217	0.0136
	FNR (6.5)	0.0769	0.1259	0.1888	0.3776	0.4755
	AC (6.1)	0.8843	0.9183	0.9572	0.9580	**0.9600**
	P (6.9)	0.3220	0.4019	0.5918	0.6357	**0.7010**
	p (6.13)	**0.9231**	0.8741	0.8112	0.6224	0.5245
	g-mean$_1$ (6.14)	**0.9023**	0.8973	0.8852	0.7803	0.7193
	g-mean$_2$ (6.15)	0.5452	0.5927	**0.6929**	0.6290	0.6063
	F$_1$ (6.10)	0.4774	0.5507	**0.6844**	0.6290	0.6000
	W (6.16)	**0.9025**	0.8976	0.8886	0.8003	0.7554

Looking closer at Table 6.8, it can be seen that while *g-mean*$_1$ and W demonstrate better performance at lower cutoffs, the values of both metrics at cutoff of 0.3 and 0.5 are very close. *g-mean*$_1$ at 0.5 is only 1.7% lower than at 0.3 and W at 0.5 is only 1.4% lower. Also, at 0.6, both metrics show a decrease of nearly 10%, indicating a precipitous drop-off beyond 0.5. While the power *p* at 0.5 is 11.2% lower than at 0.3, its value decreases 18.9% at 0.6, another dramatic decrease. Thus, while the metrics *p*, *g-mean*$_1$, and W show better performance at lower cutoffs, the performance at 0.5 is very close to their best values. Because *g-mean*$_2$, and *F*$_1$ show the best performance at 0.5, and because

p, *g-mean*$_1$, and W have dramatic drop-offs in performance beyond 0.5, it is reasonable to set the cutoff to 0.5.

Chapter 7: Conclusions

7.1 CONTRIBUTIONS AND FINDINGS

The novel use of the correlation radiometer for close-range detection presented in this dissertation represents a significant contribution to the field and can be applied to many other areas where the detection of close-range self-luminous objects is required. Specifically, the detection method using millimeter-wave radiometers was tailored to the detection of stationary humans in daytime, outdoor environments, which is a problem in intruder detection and security monitoring that previously had no consistent solution. Both the total power and correlation radiometers have a low data rate, which is significant for object detection. Some methods focus on object detection in images which requires a much larger amount of data. Because radiometer sensor outputs are simple voltage signals the processing unit can have more overhead free for computing complex detection and classification algorithms.

In applying the theory of correlation interferometry to the close-range required for human presence detection, a number of modifications were made which may be applied for similar situations of close-range detection. The sensitivity in the millimeter-wave region in outdoor environments was derived, showing that the theory developed for radio astronomy and remote sensing was feasible in such an environment. The derivation of the dwell time for the correlation radiometer with angled antennas provides a necessary framework for determining the radiometric resolution of a system with angled antennas. The phase of the incoming radiation was analyzed in the context of the far-field approximation when the antennas are angled and it was shown that if, the antenna beams

125

are narrow enough, the phase of the incoming radiation does not deviate significantly from the plane-wave approximation.

Because the radiometer sensors are passive, no range information is readily available. To begin solving this problem I presented a method of range determination using the two total power receivers whose antennas were separated by a certain baseline. The method proved to be useful, however somewhat inaccurate. Thus it provides a framework for developing a method which can estimate the range more accurately.

The use of total power and correlation radiometers for the detection of human presence has never been attempted in this context, thus there were no models of the sensor responses as they viewed a human. I analyzed some aspects of the responses, using the distributions to develop a statistical classifier to discriminate between humans and non-humans. The naïve Bayesian classifier developed is a simple probabilistic classifier which was computationally inexpensive and allows for additional features due to its simple implementation. The classifier performed well in the F_1 metric showing reasonable classification capabilities. To achieve a reasonable TPR rate of 90% the FPR was 20% using only the passive sensor for range estimation, or 10% using the active ranging laser. Both measures indicate a sensor which is not viable for immediate deployment in practical situations such as site security monitoring where nuisance alarms would be too high. However, the scientific viability of the detection method is sound and improvement of the range estimation and classifier performance would help reduce the FPR.

7.2 FUTURE WORK

The most notable drawback of the detection method is its limited range. Increasing the range is a difficult problem because of the passive nature of the sensors,

however, a number of options are possible. If the antenna beamwidth were decreased the sensors would be able to resolve a human out to resolve a human out to longer distances, as the background temperature would not be averaged with that of the human when the person is unresolved. If the frequency were increased the radiation from the human would be stronger, as the blackbody curve increase with frequency until the infrared region. The drawback of increasing the frequency comes in the transmission of the radiation through the human's clothes and through the air. As the frequency increases more radiation is attenuated through the lossy clothing material, and particles in the air introduce more attenuation as the wavelength becomes closer to that of particles in the air such as water droplets, dust, and smoke.

The human model used to derive the intrinsic radiation in the millimeter-wave region was overly simplistic and provided only an approximation of the radiation produced. This approximate model gave enough information to develop the practical aspects of the sensor hardware however a more complete model of the human could provide further insight into improvements in the sensor. A more complete model could make use of limb darkening in the calculation of the radiation. Limb darkening is the decreasing radiance from the center of an object to its edges. For instance, the radiance seen from the center of the human torso is that calculated in Chapter 2; the radiance seen from the person's side (as viewed from the front) would be less since the skin is optically thin and there is no tissue seen under the skin when viewing the edges. While making use of this and would likely reduce the approximate radiation generated, and I justify its absence by pointing out that the main focus of Chapter 2 was to derive an approximate value of the maximum radiation seen from a human.

The passive range estimate proved to be marginally accurate at best because of the preponderance of false objects detected. Improvement of this could be made by using

a linear regression with the active ranging as the regressor to train the passive ranging. If the passive range estimation were improved to the point where the active ranging was no longer needed the detection method could rely solely on the passive sensors, and would likely improve the FPR. Doing so would put the system closer to being a deployable system in settings where nuisance alarms need to be minimized.

The receiver hardware itself could be improved or modified in numerous ways. At the front end, different antennas would be beneficial for improving the coverage of the beams: multiple antennas or multiple beam antennas could be used to improve the range coverage and beamforming could be used to create beams which are tall and narrow, increasing the coverage of the beams in elevation while keeping the azimuth beams narrow enough to resolve a human out to reasonable distances.

A multiple frequency front-end could be developed to detect human radiation at significantly different frequencies. Because of the difference in emissivities of various objects the resulting received radiation will look different at separate frequencies. Because human emissivity increases rather linearly over the millimeter-wave region [1] the response from a human will look similar in different frequency bands while that of other objects may change from band to band. Being able to discriminate between objects at different band would help in removing nuisance alarms and improve the performance of the classifier. With the availability of fast A/D converters the IF signals could be directly sampled and the correlations performed in software. This would allow for improved sensitivity in the correlation channel by not requiring the relatively high cutoff of the baseband LPF as the LPF frequency could be set in software, based on the fringe frequency of the correlation signal.

Appendix A: Sensitivity of the Correlation Radiometer

This appendix analyzes the theoretical sensitivity of a simple two-element interferometer. The analysis assumes a real correlator, although the same results apply to the two outputs of a complex correlator. There are a number of different derivations of the sensitivity of a two-element interferometer [12-14, 30, 48]. In this derivation I follow the analysis of Wrobel and Walker [30] which makes use of the RMS variations of the sampled data.

The voltages from the two antennas i, j are composed of a signal component $s_{i,j}$ and a noise component $n_{i,j}$. For a single element (total power) the receiver power output is the expectation value, denoted by $\langle \cdot \rangle$, of the sum of the signal and noise squared:

$$\langle P_i \rangle = \left\langle \left(s_i + n_i \right)^2 \right\rangle = \left\langle 2 s_i n_i + s_i^2 + n_i^2 \right\rangle. \tag{A.1}$$

Because the signal and noise components are uncorrelated the expectation value of the $s_i n_i$ component tends to zero yielding

$$\langle P_i \rangle = \left\langle s_i \right\rangle^2 + \left\langle n_i \right\rangle^2. \tag{A.2}$$

The power in each component in (A.2) is given by $GkT\Delta f$ as described in Section 3.1. The signal power results from the antenna temperature and the noise power results from the system noise temperature, resulting in

$$\begin{aligned} \langle P_i \rangle &= GkT_{A,i}\Delta f + GkT_{rec,i}\Delta f = Gk\left(T_{A,i} + T_{rec,i} \right)\Delta f \\ &= GkT_{sys,i}\Delta f. \end{aligned} \tag{A.3}$$

For a correlation receiver the output power is the expectation value of the signal and noise from two antenna elements:

$$\left\langle P_{ij} \right\rangle = \left\langle \left(s_i + n_i \right) \left(s_j + n_j \right) \right\rangle = \left\langle s_i s_j + s_i n_j + s_j n_i + n_i n_j \right\rangle. \tag{A.4}$$

Because the expectation value of the noise components is zero, resulting in

$$\left\langle P_{ij} \right\rangle = \left\langle s_i s_j \right\rangle. \tag{A.5}$$

It is convenient at this point to define

$$K = \frac{A_{ant}}{2k} \tag{A.6}$$

where A_{ant} is the antenna collecting area. Since the antenna temperature can be written in terms of the detected flux density S by $T_A = A_{ant}S$, the receiver power (A.3) can be written

$$\left\langle P_i \right\rangle = Gk \left(K_i S_T + T_{sys,i} \right) \Delta f, \tag{A.7}$$

where S_T is the total flux received. Then (A.5) can be written

$$\left\langle P_{ij} \right\rangle = \sqrt{G_i G_j K_i K_j} \, k S_C \Delta f, \tag{A.8}$$

where $\sqrt{G_i G_j}$ is the expectation value of the gains of the two receivers and S_C is the correlated flux density, which is not greater than the total flux density S_T.

The RMS fluctuation, or variance, of P_{ij} is found by

$$\sigma^2(x) = \langle x^2 \rangle - \mu_x^2, \tag{A.9}$$

where in this case

$$\langle x^2 \rangle = \langle P_{ij}^2 \rangle = \left\langle \left[(s_i + n_i)(s_j + n_j) \right]^2 \right\rangle,$$
$$\mu_x = \langle P_{ij} \rangle = \sqrt{G_i G_j K_i K_j} \, k S_C \Delta f. \tag{A.10}$$

The RMS fluctuation of the power is then

$$\sigma^2(P_{ij}) = \left\langle \left[(s_i + n_i)(s_j + n_j) \right]^2 \right\rangle - G_i G_j K_i K_j k^2 S_C^2 \Delta f^2. \tag{A.11}$$

To analyze the first term, use the relation

$$\langle z_1 z_2 \cdots z_{2n+1} \rangle = 0$$
$$\langle z_1 z_2 \cdots z_{2n} \rangle = \sum_{\text{all pairs}} \langle z_i z_j \rangle \langle z_k z_l \rangle. \tag{A.12}$$

This results in

$$\sigma^2(P_{ij}) = \left[2 \langle (s_i + n_i)(s_j + n_j) \rangle^2 + \langle (s_i + n_i) \rangle^2 \langle (s_j + n_j) \rangle^2 \right] - G_i G_j K_i K_j k^2 S_C^2 \Delta f^2$$
$$= 2 G_i G_j K_i K_j k^2 S_C^2 \Delta f^2$$
$$+ G_i G_j k^2 \left(K_i S_T + T_{sys,i} \right) \left(K_j S_T + T_{sys,j} \right) \Delta f^2$$
$$- 2 G_i G_j K_i K_j k^2 S_C^2 \Delta f^2. \tag{A.13}$$

Collecting terms the RMS fluctuation is

131

$$\sigma^2\left(P_{ij}\right) = G_i G_j k^2 \Delta f^2 \left(K_i K_j S_C^2 + K_i K_j S_T^2 + K_i T_{sys,j} S_T + K_j T_{sys,i} S_T + T_{sys,i} T_{sys,j}\right) \quad \text{(A.14)}$$

The RMS fluctuation in (A.14) is in terms of the squared power $\langle P_{ij}\rangle^2$. Because the sensitivity is defined in terms of the minimum detectable flux density, the general expression between power and flux is used:

$$\langle P_{ij}\rangle = \sqrt{G_i G_j K_i K_j}\, kS\Delta f. \quad \text{(A.15)}$$

The RMS flux is then given by the square root of (A.14) divided by $\sqrt{G_i G_j K_i K_j}\, k\Delta f$:

$$S_{ij} = \sqrt{S_C^2 + S_T^2 + S_T\left(\frac{T_{sys,i}}{K_i} + \frac{T_{sys,j}}{K_j}\right) + \frac{T_{sys,i} T_{sys,j}}{K_i K_j}}. \quad \text{(A.16)}$$

For a square band-pass the number of independent samples recorded is $2\Delta f\tau$, where τ is the integration time of the correlator. The sensitivity is given by dividing (A.16) by the square root of the number of independent samples:

$$\Delta S_{ij} = \frac{1}{\sqrt{2\Delta f\tau}} \sqrt{S_C^2 + S_T^2 + S_T\left(\frac{T_{sys,i}}{K_i} + \frac{T_{sys,j}}{K_j}\right) + \frac{T_{sys,i} T_{sys,j}}{K_i K_j}}. \quad \text{(A.17)}$$

Using the (A.6) and definition of the system equivalent flux density (SEFD) given by (4.8), (A.17) can be written in the form given by (4.7):

$$\Delta S_{ij} = \sqrt{\frac{S_T^2 + S_C^2 + S_T\left(SEFD_i + SEFD_j\right) + SEFD_i SEFD_j}{2\Delta f\tau}}. \quad \text{(A.18)}$$

Appendix B: Spectral Estimation[†]

An observation of signals with P complex sinusoids in noise can be given by

$$x(n) = \sum_{p=1}^{P} \alpha_p e^{j2\pi n f_p} + w(n) \tag{B.1}$$

where $\sum_{p=1}^{P} \alpha_p e^{j2\pi n f_p}$ are the complex sinusoids with amplitudes α and $w(n)$ is the noise.

The noise power is

$$\left\langle \left| w(n) \right|^2 \right\rangle = \sigma_n^2, \tag{B.2}$$

where $\langle x \rangle$ denotes the expectation value of x. A time-window of the observed signal of length M is then

$$\mathbf{x}(n) = \begin{bmatrix} x(n) & x(n+1) & \cdots & x(n+M-1) \end{bmatrix}^{\mathrm{T}}$$

$$= \begin{bmatrix} \sum_{p=1}^{P} \alpha_p e^{j2\pi n f_p} + w(n) \\ \sum_{p=1}^{P} \alpha_p e^{j2\pi(n+1)f_p} + w(n+1) \\ \vdots \\ \sum_{p=1}^{P} \alpha_p e^{j2\pi(n+M-1)f_p} + w(n+M-1) \end{bmatrix} \tag{B.3}$$

$$= \sum_{p=1}^{P} \alpha_p \mathbf{v}(f_p) e^{j2\pi n f_p} + \mathbf{w}(n). \tag{B.4}$$

[†] This section follows [31] D. G. Monolakis, V. K. Ingle, and S. M. Kogon, *Statistical and Adaptive Signal Processing: Spectral Estimation, Signal Modeling, Adaptive Filtering and Array Processing*: Artech House, 2005.

where the Vandermonde vector

$$\mathbf{v}(f_p) = \begin{bmatrix} 1 & e^{j2\pi f_p} & \cdots & e^{j2\pi(M-1)f_p} \end{bmatrix} \tag{B.5}$$

is a discrete Fourier transform vector at frequency f_p.

The autocorrelation matrix of the observed signal is

$$\begin{aligned} \mathbf{R}_x &= \mathrm{E}\left\{\mathbf{x}(n)\mathbf{x}^{\mathrm{H}}(n)\right\} \\ &= \mathbf{R}_s + \mathbf{R}_w \\ &= \sum_{p=1}^{P} |\alpha_p|^2 \, \mathbf{v}(f_p)\mathbf{v}^{\mathrm{H}}(f_p) + \sigma_w^2 \mathbf{I}, \end{aligned} \tag{B.6}$$

where $\mathbf{R}_s$ is the autocorrelation matrix of the signal subspace, $\mathbf{R}_w$ is the autocorrelation matrix of the noise subspace, and $\mathbf{I}$ is the identity matrix. (B.6) can also be written

$$\mathbf{R}_x = \mathbf{V}\mathbf{A}\mathbf{V}^{\mathrm{H}} + \sigma_w^2 \mathbf{I}, \tag{B.7}$$

where $\mathbf{V}$ is the Vandermonde matrix

$$\mathbf{V} = \begin{bmatrix} \mathbf{v}(f_1) & \mathbf{v}(f_2) & \cdots & \mathbf{v}(f_P) \end{bmatrix} \tag{B.8}$$

and

$$\mathbf{A} = \begin{bmatrix} |\alpha_1^2| & 0 & \cdots & 0 \\ 0 & |\alpha_2^2| & & \vdots \\ \vdots & & \ddots & \\ 0 & \cdots & & |\alpha_p^2| \end{bmatrix}. \tag{B.9}$$

134

The eigendecomposition of the correlation matrix is

$$\mathbf{R}_x = \sum_{m=1}^{M} \lambda_m \mathbf{q}_m \mathbf{q}_m^{\mathrm{H}}. \tag{B.10}$$

where $\mathbf{q}_m$ is the eigenvector corresponding to the eigenvalue λ_m.

Because there are P complex sinusoids present in the signal,

$$\mathrm{rank}\left(\mathbf{VAV}^{\mathrm{H}}\right) = P. \tag{B.11}$$

If the eigenvalues of $\mathbf{VAV}^{\mathrm{H}}$ are $\left\{\tilde{\lambda}_m\right\}_{m=1}^{P}$, the eigenvalues of $\mathbf{R}_x$ are

$$\lambda_m = \tilde{\lambda}_m + \sigma_w^2 \quad \text{for } m = 1, \ldots, P. \tag{B.12}$$

Because $\mathbf{Ax} = \lambda\mathbf{x}$ it follows that $(\mathbf{A} + \sigma\mathbf{I})\mathbf{x} = (\lambda + \alpha)$ and thus the eigenvalues of $\mathbf{R}_x$ can be written

$$\lambda_m = \begin{cases} \tilde{\lambda}_m + \sigma_w^2, & m \leq P, \\ \sigma_w^2, & m > P. \end{cases} \tag{B.13}$$

Thus there is a clean, discrete separation between the subspace containing the noise and the subspace containing the signal and the noise. The correlation matrix can now be written

$$\mathbf{R}_x = \sum_{m=1}^{P} \left(\tilde{\lambda}_m + \sigma_w^2\right) \mathbf{q}_m \mathbf{q}_m^{\mathrm{H}} + \sum_{m=P+1}^{M} \sigma_w^2 \mathbf{q}_m \mathbf{q}_m^{\mathrm{H}}. \tag{B.14}$$

135

Thus the *M*-dimensional subspace containing the observations (B.3) can be split into a signal subspace and a noise subspace. Furthermore, since $\mathbf{R}_x$ is Hermitian symmetric, the signal and noise subspaces are orthogonal.

B.1 PISARENKO HARMONIC DECOMPOSITION (PHD)

Because the signal and noise subspaces are orthogonal, the frequencies of the complex sinusoids contained in the observations can be found by determining where the vector product of the signal and noise subspaces goes to zero.

If the observation time-window is limited to one more than the number of complex sinusoids

$$M = P + 1, \tag{B.15}$$

there is then only one noise eigenvector $\mathbf{q}_M$ corresponding to the eigenvalue λ_M. Since the signal and noise subspace are orthogonal, all of the *P* complex exponentials are orthogonal to the eigenvector $\mathbf{q}_M$:

$$\mathbf{v}^{\mathrm{H}}\left(f_p\right)\mathbf{q}_M = \sum_{k=1}^{M}\mathbf{q}_M e^{j2\pi(k-1)f_p} = 0. \tag{B.16}$$

The *pseudospectrum* is then calculated as

$$\mathbf{R}_{phd}\left(e^{j2\pi f}\right) = \frac{1}{\left|\mathbf{v}^{\mathrm{H}}\left(f\right)\mathbf{q}_M\right|^2}. \tag{B.17}$$

The peaks in the pseudospectrum indicate the frequencies of the complex sinusoids.

136

B.1.1 Sample Correlation Matrix

The accuracy of the Pisarenko method is dependent on the accuracy with which $\mathbf{q}_M$ is calculated. However, $\mathbf{q}_M$ (and thus λ_M) will only be precisely calculated from the true correlation matrix (B.6). In practice, the true correlation matrix is unattainable due to its dependence on the entire observed signal and must be estimated from the available data. As a result, the eigenvector $\mathbf{q}_M$ in the Pisarenko method has an error associated with it that is only minimized by increasing the number of data points used to estimate the correlation matrix. The estimated correlation matrix, or *sample correlation matrix*, is estimated by first calculating the data matrix

$$\mathbf{X} = \begin{bmatrix} \mathbf{x}^T(0) \\ \mathbf{x}^T(1) \\ \vdots \\ \mathbf{x}^T(n) \\ \vdots \\ \mathbf{x}^T(N-2) \\ \mathbf{x}^T(N-1) \end{bmatrix} = \begin{bmatrix} x(0) & x(1) & \cdots & x(M-1) \\ x(1) & x(2) & \cdots & x(M-2) \\ \vdots & \vdots & \ddots & \vdots \\ x(n) & x(n+1) & \cdots & x(n+M-1) \\ \vdots & \vdots & \ddots & \vdots \\ x(N-2) & x(N-1) & \cdots & x(N+M-3) \\ x(N-1) & x(N) & \cdots & x(N+M-2) \end{bmatrix}, \qquad \text{(B.18)}$$

where N is specified to determine the matrix size. The sample correlation matrix is then

$$\hat{\mathbf{R}}_x = N^{-1}\mathbf{X}^H\mathbf{X}. \qquad \text{(B.19)}$$

B.2 MULTIPLE SIGNAL CLASSIFICATION (MUSIC)

The MUSIC algorithm allows the time-window to increase beyond one greater than the number of complex sinusoids and thus allowing a greater number of noise

eigenvectors to be used. This allows for averaging over the noise subspace, increasing the accuracy of the pseudospectrum.

The vector product of the observed signal and the eigenvectors is then

$$\mathbf{v}^{\mathrm{H}}\left(f_p\right)\mathbf{q}_m = \sum_{k=1}^{M} \mathbf{q}_m\left(k\right)e^{j2\pi(k-1)f_p} = 0 \quad \text{for } P < m \le M \tag{B.20}$$

for all P frequencies f_p of the complex sinusoids. The pseudospectrum for each eigenvector is

$$\mathbf{R}_m\left(e^{j2\pi f}\right) = \frac{1}{\left|\mathbf{v}^{\mathrm{H}}\left(f\right)\mathbf{q}_m\right|^2} \tag{B.21}$$

and the MUSIC pseudospectrum is

$$\mathbf{R}_{music}\left(e^{j2\pi f}\right) = \frac{1}{\sum\limits_{m=P+1}^{M}\left|\mathbf{v}^{\mathrm{H}}\left(f\right)\mathbf{q}_m\right|^2}. \tag{B.22}$$

B.3 ESTIMATION OF SIGNAL PARAMETERS USING ROTATIONAL INVARIANCE TECHNIQUES (ESPRIT)

Whereas the PHD and MUSIC algorithms made use of the sample correlation matrix $\hat{\mathbf{R}}_x$, the ESPRIT algorithm uses the data matrix $\mathbf{X}$. The observed signal given by (B.4) can be written as

$$\mathbf{x}\left(n\right) = \sum_{p=1}^{P}\alpha_p\mathbf{v}\left(f_p\right)e^{j2\pi nf_p} + \mathbf{w}\left(n\right) = \mathbf{V}\mathbf{\Phi}^n\mathbf{\alpha} + \mathbf{w}\left(n\right), \tag{B.23}$$

where $\mathbf{V}$ is given by (B.8), $\boldsymbol{\alpha}$ is a vector of the amplitudes, and

$$\boldsymbol{\Phi} = \begin{bmatrix} e^{j2\pi f_1} & 0 & \cdots & 0 \\ 0 & e^{j2\pi f_2} & \cdots & 0 \\ \vdots & \vdots & \ddots & \vdots \\ 0 & \cdots & 0 & e^{j2\pi f_P} \end{bmatrix} \tag{B.24}$$

is the diagonal matrix composed of the phase shifts between time samples. This rotation matrix is composed of the frequencies of the complex exponentials, and thus in determining this matrix the frequencies can be found.

The signal subspace

$$\mathbf{s}(n) = \mathbf{V}\boldsymbol{\Phi}^n \boldsymbol{\alpha} \tag{B.25}$$

is partitioned into two $(M-1)$-dimensional subspaces $\mathbf{s}_{M-1}$ by

$$\mathbf{s}(n) = \begin{bmatrix} \mathbf{s}_{M-1}(n) \\ s(n+M-1) \end{bmatrix} = \begin{bmatrix} s(n) \\ \mathbf{s}_{M-1}(n+1) \end{bmatrix}. \tag{B.26}$$

Equivalent to (B.25) the subwindows can be written

$$\mathbf{s}_{M-1}(n) = \mathbf{V}_{M-1}\boldsymbol{\Phi}^n \boldsymbol{\alpha} \quad \text{and} \quad \mathbf{s}_{M-1}(n+1) = \mathbf{V}_{M-1}\boldsymbol{\Phi}^{n+1}\boldsymbol{\alpha}. \tag{B.27}$$

Defining

$$\mathbf{V}_1 = \mathbf{V}_{M-1}\boldsymbol{\Phi}^n \quad \text{and} \quad \mathbf{V}_2 = \mathbf{V}_{M-1}\boldsymbol{\Phi}^{n+1} \tag{B.28}$$

gives the relation

139

$$V_2 = V_1 \Phi. \tag{B.29}$$

Until this point the derivation has made use of the actual signal space $s(n)$. To estimate the frequencies the data matrix X and (B.29) are used to access Φ. First a singular value decomposition (SVD) is performed on the data matrix yielding

$$X = L\Sigma U^H, \tag{B.30}$$

where L is the $N \times N$ matrix of left singular values, Σ is the $N \times M$ matrix of descending singular values on the diagonal, and U is the $M \times M$ matrix of right singular values. The columns of U are the eigenvectors of $\hat{R}_x$ and the squared magnitude of the singular values are the eigenvalues scaled by N through (B.19). Thus the matrix U can be divided into the signal and noise subspaces by

$$U = \begin{bmatrix} U_s | U_n \end{bmatrix}. \tag{B.31}$$

U_s contains only the singular values with the P largest values, and thus spans the same subspace as V, and thus there exists a transform

$$V = U_s T. \tag{B.32}$$

The subspace U_s is partitioned into two $(M - 1)$-dimensional subspaces in the same way that V was in (B.28) and thus, by (B.29), a rotation Ψ must exist such that

$$U_2 = U_1 \Psi. \tag{B.33}$$

Through (B.32) the partitioned subspaces have the relations

$$\mathbf{V}_1 = \mathbf{U}_1 \mathbf{T}, \tag{B.34}$$
$$\mathbf{V}_2 = \mathbf{U}_2 \mathbf{T}. \tag{B.35}$$

Thus the partitioned subspaces of the actual signals $\mathbf{V}$ and the estimated signals $\mathbf{U}$ can be related by

$$\mathbf{V}_2 = \mathbf{U}_2 \mathbf{T} = \mathbf{U}_1 \mathbf{\Psi} \mathbf{T}. \tag{B.36}$$

$\mathbf{V}_2$ can also be solved for through (B.29) and (B.35) yielding

$$\mathbf{V}_2 = \mathbf{V}_2 \mathbf{\Phi} = \mathbf{U}_1 \mathbf{T} \mathbf{\Phi}. \tag{B.37}$$

Equating (B.36) and (B.37) gives

$$\mathbf{\Psi} = \mathbf{T} \mathbf{\Phi} \mathbf{T}^{-1}. \tag{B.38}$$

Thus the diagonal elements of $\mathbf{\Phi}$ are the eigenvectors of $\mathbf{\Psi}$. Since the diagonal elements of $\mathbf{\Phi}$ are of the form $exp(j2\pi f_p)$, the frequency estimates are found by taking the phase of the eigenvectors of $\mathbf{\Psi}$. The rotation matrix $\mathbf{\Psi}$ is calculated through (B.33) by

$$\mathbf{\Psi} = \left(\mathbf{U}_1^H \mathbf{U}_1 \right)^{-1} \mathbf{U}_1^H \mathbf{U}_2. \tag{B.39}$$

References

[1]   C. D. Govan, "A Wide-band Frequency-Tunable Dicke Radiometer for Microwave Radiometric Measurements," M.S. Thesis, The University of Texas at Austin, 1994.

[2]   L. D. Harmon, "Tactile Sensing for Robots," in *Recent Advances in Robotics*. vol. 1: John Wiley and Sons, 1983.

[3]   H. R. Everett, *Sensors for Mobile Robots: Theory and Application*: A. K. Peters, Ltd, 1995.

[4]   H. E. M. Viggh and A. M. Flynn, "Infrared People Sensors for Mobiles Robots," *Proceedings of the SPIE,* vol. 1007, 1998.

[5]   J. E. Bjarnason, T. L. J. Chan, A. W. M. Lee, M. A. Celis, and E. R. Brown, "Millimeter-wave, Terahertz, and Mid-Infrared Transmission through Common Clothing," *Applied Physics Letters,* vol. 85, 2004.

[6]   T. D. Williams and N. M. Vaidya, "A Compact, Low-Cost, Passive MMW Security Scanner," *Proceedings of the SPIE,* vol. 5789, 2005.

[7]   D. J. Fixsen, E. S. Cheng, J. M. Gales, J. C. Mather, R. A. Shafer, and E. L. Wright, "The Cosmic Microwave Background Spectrum from the Full COBE FIRAS Data Set," *Astrophysical Journal,* vol. 473, 1996.

[8]   R. Doyle, B. Lyons, A. Lettington, T. McEnroe, J. Walshe, J. McNaboe, and P. Curtin, "Illumination Strategies to Achieve Effective Indoor Millimeter-wave Imaging for Personnel Screening," *Proceedings of the SPIE,* vol. 5789, 2005.

[9]   D. M. Sheen, D. L. McMakin, W. M. Lechelt, and J. W. Griffin, "Circularly Polarized Millimeter-Wave Imaging for Personnel Screening," *Proceedings of the SPIE,* vol. 5789, 2005.

[10]   C. A. Martin, W. Manning, V. G. Koliko, and M. Hall, "Flight Test of a Passive Millimeter-Wave Imaging System," *Proceedings of the SPIE,* vol. 5789, 2005.

[11]   D. A. Wikner, "Passive Millimeter-Wave Imagery of Helicopter Obstacle in Sand," *Proceedings of the SPIE,* vol. 6211, 2006.

[12]   J. D. Kraus, *Radio Astronomy*: McGraw-Hill, 1966.

[13]   W. N. Christiansen and J. A. Högbom, *Radiotelescopes*. London: Cambridge University Press, 1969.

[14]   A. R. Thompson, J. M. Moran, and G. W. Swenson, *Interferometry and Synthesis in Radio Astronomy*: John Wiley & Sons, 2001.

[15]   K. Rohlfs, *Tools of Radio Astronomy*. Berlin: Springer-Verlag, 1990.

[16]   F. T. Ulaby, R. K. Moore, and A. K. Fung, *Microwave Remote Sensing: Active and Passive Vol I* vol. 1: Addison-Wesley, 1981.

[17]   D. M. LeVine, "The Sensitivity of Synthetic Aperture Radiometers for Remote Sensing Applications from Space," *Radio Science,* vol. 25, p. 441, 1990.

[18]   D. M. LeVine, "Synthetic Aperture Radiometer Systems," *IEEE Transactions on Microwave Theory and Techniques,* vol. 47, p. 2228, 1999.

[19]   D. Mitchell, C. H. Wyndham, T. hodgson, and F. R. N. Nabarro, "Measurement of the Total Normal Emissivity of Skin Without the Need for Measuring Skin Temperature," *Physics in Medicine and Biology,* vol. 12, p. 359, 1967.

[20] F. P. Incropera and D. P. DeWitt, *Fundamentals of Heat and Mass Transfer*: John Wiley & Sons, 2002.

[21] G. B. Rybicki and A. P. Lightman, *Radiative Processes in Astrophysics*: Wiley-VCH, 2004.

[22] T. S. England, "Dielectric Properties of the Human Body in the 1-10cm Range," *Nature,* vol. 166, September 16, 1950.

[23] H. Alexander and D. L. miller, "Determining Skin Thickness with Pulsed Ultra Sound," *The Journal of Investigative Dermatology,* vol. 72, pp. 17-19, 1979.

[24] I. Yamaura, "Measurements if 1.8-2.7 GHz Microwave Attenuation in the Human Torso," *IEEE Transactions on Microwave Theory and Techniques,* vol. MTT-25, pp. 707-710, August 1977.

[25] F. A. Davis, *Tabler's Cyclopedic Medical Dictionary*: F. A. Davis Company, 1993.

[26] H. Ling: Personal Communication, 2004.

[27] D. A. Thompson, R. L. Rogers, and J. H. Davis, "Temperature Compensation of Total Power Radiometers," *IEEE Transactions on Microwave Theory and Techniques,* vol. 51, pp. 2073-2078, October 2003.

[28] Agilent, "Noise Figure Measurement Accuracy - The Y-Factor Method," Agilent Application Note 57-2 2004.

[29] Agilent, "Fundamentals of RF and Microwave Noise Figure Measurements," Agilent Application Note 57-1 2004.

[30] J. M. Wrobel and R. C. Walker, "Sensitivity," in *Synthesis Imaging in Radio Astronomy II*. vol. 180, G. B. Taylor, C. L. Carilli, and R. A. Perly, Eds.: ASP Conference Series, 1999, pp. 171-186.

[31]   D. G. Monolakis, V. K. Ingle, and S. M. Kogon, *Statistical and Adaptive Signal Processing: Spectral Estimation, Signal Modeling, Adaptive Filtering and Array Processing*: Artech House, 2005.

[32]   P. Stoica and R. Moses, *Introduction to Spectral Analysis*: Prentice Hall, 1997.

[33]   R. O. Schmidt, "Multiple Emitter Location and Signal Parameter Estimation," *IEEE Transactions on Antennas and Propagation,* vol. AP-34, pp. 276-280, March 1986.

[34]   B. Ottersten and T. Kailath, "Direction-of-Arrival Estimation for Wide-Band Signals Using the ESPRIT Algorithm," *IEEE Transactions on Acoustics, Speech, and Signal Processing,* vol. 38, pp. 317-327, February 1990.

[35]   D. S. Briggs, F. R. Schwab, and R. A. Sramek, "Imaging," in *Synthesis Imaging in Radio Astronomy II*. vol. 180, G. B. Taylor, C. L. Carilli, and R. A. Perly, Eds.: ASP Conference Series, 1999, pp. 127-149.

[36]   J. A. Nanzer, "A K_a-Band Correlation Radiometer for Human Presence Detection from a Moving Platform," M.S. Thesis, The University of Texas at Austin, 2005.

[37]   J. A. Nanzer and R. L. Rogers, "A K_a-band Correlation Radiometer for Human Presence Detection from a Moving Platform," in *IEEE MTT-S International Microwave Symposium*, Honolulu, Hawai'i, June 3-8, 2007, pp. 385-388.

[38]   L. R. Rabiner, M. R. Sambur, and C. E. Schmidt, "Applications of a Nonlinear Smoothing Algorithm to Speech Processing," *IEEE Transactions on Acoustics, Speech, and Signal Processing,* vol. 23, pp. 552-557, December 1975.

[39]   I. Rish, "An Empirical Study of the Naive Baye's Classifier," in *Proceedings of ICJAI-01 Workshop on Empirical Methods in AII*, Sicily, Italy, 2001, pp. 41-46.

[40]   W. H. Press, S. A. Teukolsky, W. T. Vetterling, and B. P. Flannery, *Numerical Recipes in C*: Cambridge University Press, 1992.

[41]   M. A. Stephens, "Use of the Kolmogorov-Smirnov, Cramer-Von Mises and Related Statistics Without Extensive Tables," *Journal of the Royal Statistical Society Series B,* vol. 32, pp. 115-122, 1970.

[42]   M. S. Hersman and G. A. Poe, "Sensitivity of the Total Power Radiometer with Periodic Absolute Calibration," *IEEE Transactions on Microwave Theory and Techniques,* vol. MTT-29, pp. 32-40, January 1981.

[43]   R. H. Dicke, "The Measurement of Thermal Radiation at Microwave Frequeuncies," *The Review of Scientific Instruments,* vol. 14, pp. 268-275, July 1946.

[44]   S. L. Cruz-Pol, C. S. Ruf, and S. J. Keihm, "Improved 20-32 GHz Atmospheric Absorption Model," *Radio Science,* vol. 33, pp. 1319-1333, June 1998.

[45]   C. Chen, A. Liaw, and L. Breiman, "Using Random Forest to Learn Imbalanced Data," University of California, Berkeley Department of Statistics Technical Report 666 July 2004.

[46]   D. D. Lewis and W. A. Gale, "A Sequential Algorithm for Training Text Classifiers," in *Proceedings of the Seventeenth Annual International ACM SIGIR Conference on Research and Development in Information Retrieval*, 1994, pp. 3-12.

[47]   M. Kubat, R. C. Holte, and S. Matwin, "Machine Learning for the Detection of Oil Spills in Satellite Radar Images," *Machine Learning,* vol. 30, pp. 195-215, February 1998.

[48]   P. C. Crane and P. J. Napier, "Sensitivity," in *Synthesis Imaging in Radio Astronomy*, R. A. Perley, F. R. Schwab, and A. H. Bridle, Eds. San Francisco, 1989, pp. 139-165.

Vita

Jeffrey Allan Nanzer received the B.S. degree in electrical engineering and the B.S. degree in computer engineering from Michigan State University, East Lansing, MI, in 2003 and the M.S.E. degree in electrical engineering from the University of Texas at Austin, Austin, TX, in 2005 and is currently working toward the Ph.D. degree in electrical engineering at the University of Texas at Austin.

From 2002 to 2003 he was a Research Assistant at Michigan State University where he developed testing procedures for genetic-algorithm-based self-structuring antennas. He currently works as a Graduate Research Assistant at the University of Texas at Austin Applied Research Laboratories in Austin, TX.

Publications:

1. **J.A. Nanzer** and R.L. Rogers, "Human Presence Detection using Millimeter-wave Radiometry," IEEE Transactions on Microwave Theory and Techniques, vol. 55, no. 12, pp. 2727-2733, 2007

2. **J.A. Nanzer** and R.L. Rogers, "A K_a-band Correlation Radiometer for Human Presence Detection From a Moving Platform," IEEE MTT-S International Microwave Symposium, June 3-8, 2007, pp.385-388

3. G. Kogut, G. Ahuja, E.B. Pacis, D. Carroll, J. Giles, R.L. Rogers, and **J.A. Nanzer**, "Sensor Fusion for Automatic Detection of Human Presence," Int. Joint Topic: 9th Emergency Preparedness and Response/11th Robotics and Remote Systems for Hazardous Environments, February 12-15, 2006.

4. B.T. Perry, **J.A. Nanzer**, E.J. Rothwell, L.C. Kempel, J.E. Ross, and L.L. Nagy, "A Comparison of Several Self-Structuring Antenna Templates," IEEE AP-S International Symposium and URSI Radio Science Meeting, June 23-26, 2003

Permanent address: 6005 San Paublo Ct, Austin TX 78749

This dissertation was typed by the author.